STRUCTURAL GEOLOGY AND HYDROGEOLOGIC CHARACTERIZATION OF FAULTS IN POORLY LITHIFIED SEDIMENTS

BY

GEOFFREY CALLIS RAWLING

Submitted in Partial Fulfillment
of the Requirements for the

Doctorate of Philosophy in Geology

New Mexico Institute of Mining and Technology
Department of Earth and Environmental Science

Socorro, New Mexico

May, 2002

ABSTRACT

In this study I integrate field and microstructural observations, field and laboratory permeability measurements, and analytical and numerical hydrologic models to understand the structural development, operative deformation mechanisms, and impact on subsurface fluid flow of normal faults in poorly lithified sediments. The study sites are faults cutting sediments of the Tertiary Santa Fe Group in the Albuquerque and Socorro Basins of the Rio Grande rift, central New Mexico, USA.

These fault zones do not contain macroscopic fractures; they are characterized by deformation bands where they cut sandy sediments. The fault cores are composed of foliated clay flanked by structurally and lithologically heterogeneous mixed zones, in turn flanked by damage zones. Structures present within these fault-zone architectural elements are different from those in brittle faults formed in lithified sedimentary and crystalline rocks which do contain fractures. Mixed zones are structurally and hydrologically heterogeneous, and are not present in brittle faults in crystalline and well-lithified sedimentary rocks. Sediment is initially incorporated into mixed zones by

processes typical of brittle faults (e.g., asperity and tipline bifurcation), and may be continually added throughout the movement history of the fault. Mixed zones exhibit macroscopically ductile structures formed by penetrative particulate flow. In sand-rich lithologies, these are overprinted by deformation bands, which represent a later, more localized style of deformation. These structures and overprinting relationships are consistent with the inferred consolidation history of the faults and their host sediments.

Microscopic observations reveal that the mode of grain fracture within the fault zones is controlled by relative grain strength. Transgranular fracturing of quartz is rarely observed. Rather, quartz typically deforms by flaking of grain edges, feldspar by transgranular fracture facilitated by cleavage, and lithic fragments by transgranular fracture or distributed microcracking. Particle size measurements indicate that progressive deformation produces particle size distributions that can be described by power-law models, characterized by low D values (1.7 – 2.1). This indicates that the particle size distributions have more proportionally more large particles than would be expected from cataclasis by constrained comminution ($D \sim 2.6$). I interpret the results in terms of cataclastic deformation by controlled particulate flow under low confining pressure, in which extensive transgranular fracturing is not necessary for strain accumulation. This style of cataclastic deformation is different from the transgranular fracturing observed in crystalline and lithified sedimentary rocks.

The structural differences between faults with deformation bands in poorly lithified sediments such as the Sand Hill fault and faults with fractures in crystalline and lithified sedimentary rocks are reflected in the permeability structures of the two fault-zone types. Equivalent permeability calculations indicate that the large-displacement

normal faults in poorly lithified sediments examined in this study have little potential to act as vertical fluid-flow conduits and have a much greater effect on horizontal fluid flow than faults with fractures.

Numerical flow models indicate that fluid flow in faults with fractures in lithified sedimentary rocks is concentrated in fracture-rich damage zones, which allow extensive vertical redistribution of flow. Faults with mixed zones in poorly lithified sediments are more effective barriers to horizontal flow. Flow is induced in low permeability layers adjacent to such faults, and there is less potential for vertical redistribution, or focussing, of flow within the fault zone. Increasing the internal fault zone complexity and varying the thickness of the host strata have only secondary effects on fault-related fluid flow patterns for both fault types. Three-part fault-zone models therefore appear adequate to provide simulations of fluid-flow patterns in basin-scale numerical flow models.

ACKNOWLEDGEMENTS

Many people and organizations contributed greatly to the successful completion of this dissertation. I first thank my advisor, Laurel Goodwin, for her guidance and motivation, which more than once saved me from throwing up my hands in terminal frustration. Likewise, my advisory committee of John Wilson, Peter Mozley, Harold Tobin, and Bill Haneberg offered helpful comments and insight and were all great people to work with. The late Allan Gutjahr cured me of my aversion to mathematics with his excellent teaching and enthusiasm, and also pulled the appropriate strings to get a field vehicle for free! I miss him greatly, as do all who knew him. Many thanks are due the National Science Foundation and The New Mexico Geological Society for funding the research. Dustin Smyth was a great field partner, and Jeff Arbuckle and Scott Mozley were cheerful and capable field assistants. Fellow faulty grad students John Sigda and Matt Herrin kindly provided data and many hours of discussion on the nature of deformed dirt. Andy Dunn taught me how to do get things done in the soils lab and did several experiments for me. Floyd Hewitt at the machine shop did an excellent job

making all sorts of widgets on short notice. Felix Barreras was a great help with computer assembly and debugging. I made many great friends along the way, including fellow geologists, mathematicians, jovial freaks, and various combinations thereof. So eternal Viking hails and a brimming flagon of mead for the following for their help, laughs, and companionship: Lane Andress, Sunny Baer, Chris Bartlett, Chris Harpel, David Kebler, Scott Lynch, Erwin Melis, Erik Munroe, Peter Rinkleff, and Jeff Winick. And of course the four-legged furry friends: Basa, Cholla, Meatloaf, Muhammad, and Suske! Finally, many thanks to my parents for all their love and support over the years.

TABLE OF CONTENTS

Page

CHAPTER 1. INTRODUCTION 1

1.1. Background 1

1.2. Objectives and Approach 2

1.3. Organization 3

CHAPTER 2. STRUCTURAL DEVELOPMENT AND IMPLICATIONS FOR FLUID FLOW OF MIXED ZONES WITHIN FAULTS IN POORLY LITHIFIED SEDIMENTS 5

2.1. Abstract 5

2.2. Introduction 6

2.3. Study Areas 10

2.4. Macroscopic Fault Zone Structures of the Santa Ana Fault 12

2.5. Macroscopic Fault Zone Structures of the Sand Hill Fault 17

2.5.1. Fault Zone Architecture 17

2.5.2. Planar Structures 17

2.5.3. Outcrop Maps 24
2.6. Microstructural Observations 30
2.6.1. Sample Description and Preparation 30
2.6.2. Grain Shape Preferred Orientations 31
2.6.3. Pore Geometry 34
2.7. Discussion 44
2.7.1. Incorporation of Sediment into the Fault Zone 44
2.7.2. Ductile Deformation and Particulate Flow 46
2.7.3. Deformation Bands 51
2.7.4. Fault-zone Structural Development 52
2.8. Implications 56
2.9. Conclusions 58
2.10. Appendix – Calculation of Two-point Correlation Functions 59
2.12. References Cited 60

CHAPTER 3. CATACLASIS AND PARTICULATE FLOW IN FAULTED, POORLY LITHIFIED SEDIMENTS 70

3.1. Abstract 70
3.2. Introduction 71
3.3. Geologic Setting and Study Areas 75
3.3.1. Sand Hill Fault Site 75
3.3.2 Fault Zone Structures 78
3.3.3. Bosque del Apache Site 81

3.4. Methods 83
3.4.1. Sample Collection 83
3.4.2. Particle Size Measurement 84
3.4.3. Microscopy 88
3.5. Results 89
3.5.1. BSE and SEM Microscopy 89
3.5.2. Particle Size Distributions 95
3.6. Discussion 100
3.6.1. Mechanisms of Cataclasis 100
3.6.2. Deformation Model 103
3.6.3. Implications 106
3.7. Conclusions 108
3.8. Acknowledgements 109
3.9. References Cited 110

CHAPTER 4. INTERNAL ARCHITECTURE, PERMEABILITY STRUCTURE, AND HYDROLOGIC SIGNIFICANCE OF CONTRASTING FAULT-ZONE TYPES 117

4.1. Abstract 117
4.2. Introduction 118
4.3. The Sand Hill Fault 119
4.4. Methods 123
4.5. Discussion 123

4.5.1. Permeability Data 123

4.5.2. Bulk Hydrologic Properties 125

4.6. Conclusions 128

4.7. Acknowledgements 129

4.8. References Cited 129

CHAPTER 5. NUMERICAL MODELLING OF FLUID FLOW PATTERNS ADJACENT TO CONTRASTING FAULT-ZONE TYPES 134

5.1. Abstract 134

5.1. Introduction 135

5.2. Descriptions of the Models 138

5.2.1. Net Flux Calculations 138

5.2.2. Models of Faulted Sedimentary Sequences 139

5.2.3. Model 1 - Juxtaposition 141

5.2.4. Model 2 – Simple Fault Zone 141

5.2.5. Model 3 – Subdivided Fault Zone 143

5.2.6. Model 4 – Varied Sedimentary Thickness 143

5.3. Model Computations 143

5.4. Results 146

5.4.1. Net Flux Calculations 146

5.4.2. Model 1 - Juxtaposition 146

5.4.2. Model 2 - Simple Fault Zone 146

5.4.3. Model 3 - Subdivided Fault Zone 151

5.4.4. Model 4 - Varied Sedimentary Thickness 156

5.5. Discussion and Implications 159

5.6. Conclusions 161

5.7. References Cited 162

CHAPTER 6. CONCLUSIONS 166

6.1. Overview 166

6.2. How do the Outcrop-scale Structures and Architectural Elements Develop? 166

6.3. What are the Primary Deformation Mechanisms? 167

6.4. What is the Permeability Structure of Large Displacement Normal Faults in Poorly Lithified Sediments? 168

6.5. What are the Implications of this Permeability Structure for Fault-proximal and Basin-scale Subsurface Fluid Flow? 169

6.6. How can the Geology and Permeability Structure of these Faults Best be Incorporated Into Subsurface Fluid Flow Models? 170

6.7. Suggestions for Future Work 170

APPENDIX 1. AN OVERVIEW OF CRITICAL STATE SOIL MECHANICS .. 173

A1.1. Introduction 173

A1.2. Basic Concepts of Critical State Soil Mechanics 174

A1.3. Interpreting Deformation Histories on the Critical State Diagram 179

A1.3.1. Consolidation of Sediments 179

A1.3.2. Tectonic Deformation of Sediments 181

A1.4. Summary 185

A1.5. References Cited 186

APPENDIX 2. SAND HILL FAULT PERMEABILITY MEASUREMENTS 188

REFERENCES CITED 194

LIST OF TABLES

Table **Page**

1. Sample descriptions and grain-shape preferred orientation statistics. 35

2. Deformation band shear zone particle size distribution data 98

3. Relative permeabilities of flow model components 140

4. Results of net flux calculations 147

LIST OF FIGURES

Figure **Page**

1. Study sites in Albuquerque Basin of Rio Grande rift. 11

2. Photograph and sketch from photograph of Santa Ana fault outcrop..... 13

3. Individual and clustered fault-parallel deformation bands offset by deformation bands in the R1 orientation..... 15

4. Shear zone of coalesced deformation bands separating footwall mixed zone from footwall damage zone 16

5. Schematic cross-section of Sand Hill fault zone showing architectural elements and representative orientations and senses of movement of populations of deformation bands 19

6. Cross-section of upper portion of Shooting Gallery outcrop..... 20

7. Lower hemisphere equal area net of poles to planar structures at upper Shooting Gallery outcrop. 20

8. Cross section of lower portion of Shooting Gallery outcrop. 21

9. Cross section of west half of Waterfall outcrop..... 22

10. Foliations in footwall mixed zone of upper Shooting Gallery outcrop 25

11. Compositional layers with S-, C-, and C'-surfaces indicated 26

12. Compositional banding and foliation in the Waterfall outcrop 29

13. Rose diagrams of orientations of grain long axes in two perpendicular sections of undeformed sand 32

14. Rose diagrams of orientations of grain long axes in mutually perpendicular sections of deformed sands 33

15. Example of calculation of two-point correlation functions for a section within the plane of the fault 39

16. Two-point correlation function difference plots for images from two perpendicular sections of undeformed sand 41

17. Two-point correlation function difference plots for images from mutually perpendicular sections of deformed sand 43

18. Study site along Sand Hill fault zone in Albuquerque basin of Rio Grande rift. 76

19. Ternary diagram showing the relative proportions of quartz, feldspar + granitic/gneissic fragments and lithic fragments 77

20. Shear zone of coalesced deformation bands forming contact between footwall damage zone and footwall mixed zone within Sand Hill fault zone 79

21. Map of excavated outcrop in footwall of Sand Hill fault zone 80

22. Compositional data from the Bosque del Apache site 82

23. Crushed quartz sand PSDs by weight determined by seiving and image analysis methods 87

24. Back-scattered electron images from DBSZ at Sand Hill fault site 91

25. Secondary electron images 94

26. Sand Hill fault PSD data 96

27. Bosque del Apache PSD data 99

28. Grain bridge model for deformation within fault in poorly lithified sediment 104

29. Study sites along Sand Hill fault zone in Albuquerque basin of Rio Grande rift 120

30. Shear zone of coalesced deformation bands forming contact between footwall damage zone and footwall mixed zone within Sand Hill fault zone. 122

31. Permeability data for FWFs in crystalline rocks and DBF 124

32. Hydrologic models and results of equivalent permeability calculations 126

33. Model 1 (juxtaposition-only) domain 142

34. Model 2 (simple fault) domain 142

35. Model 3 (subdivided fault) domain 144

36. Model 4 (varied sedimentary thickness) domain 144

37. Results for model 1 148

38. Results for model 2, poorly lithified sediment case 150

39. Results for model 2, lithified sedimentary rock case 152

40. Results for model 3, poorly lithified sediment case 153

41. Results for model 3, lithified sedimentary rock case 155

42. Results for model 4, poorly lithified sediment case 157

43. Results for model 4, lithified sedimentary rock case 158

A1.1. A perspective view of the critical state diagram 175

A1.2. Three mutually perpendicular slices through the critical state diagram 177

This dissertation is accepted on behalf of the
Faculty of the Institute by the following committee:

Advisor

1/14/2002
Date

I release this document to the New Mexico Institute of Mining and Technology.

Student's Signature

1/14/2002
Date

CHAPTER 1. INTRODUCTION

1.1. Background

It is widely recognized that faults in the shallow crust exert primary controls on subsurface fluid flow regimes. Much work has focussed on characterizing the internal structure and hydrologic properties of brittle fault zones to better understand and quantify these controls. Studies of brittle fault zones in crystalline and lithified, low-porosity sedimentary rocks have identified a characteristic internal architecture that has been summarized in conceptual geologic and hydrologic models (see introductory sections to Chapters 2 and 4).

Many heavily developed aquifers in urban areas in the southwestern United States are in poorly lithified Tertiary sediments that are pervasively cut by normal faults. Many important oil fields, such as the US Gulf Coast, are in heavily faulted, poorly lithified sediments. Previous field studies in the Albuquerque and Socorro basins of the Rio Grande rift by New Mexico Tech researchers have shown that the basic structures of these faults, and their distribution into a characteristic arrangement of fault zone

architectural elements, are considerably different from those described in existing conceptual models (see introductory sections to Chapters 2 and 4).

1.2. Objectives and Approach

Given the aforementioned observations, several interrelated questions arise of both fundamental and applied geologic and hydrologic interest pertaining to faults in poorly lithified sediments: How do the outcrop-scale structures and architectural elements develop? What are the primary deformation mechanisms? What is the resulting permeability structure of the fault zone? What are the implications of this permeability structure for fault-proximal and basin-scale subsurface fluid flow? How can the geology and permeability structure of these faults best be incorporated into subsurface fluid flow models? The objective of this work is to address these questions. My approach is to first develop an understanding of how microscale deformation mechanisms and sequential development of fault zone structures result in the characteristic fault zone internal architecture and its corresponding permeability structure. I then assess the impact of the faults on subsurface fluid flow with models that incorporate the essential geologic and hydrologic data.

The field study areas are the Sand Hill and Santa Ana faults, Albuquerque Basin, New Mexico, and a series of small faults within the Bosque del Apache National Wildlife Refuge, Socorro Basin, New Mexico. These faults cut poorly lithified sediments of the Tertiary Santa Fe Group and have large (100's of m), moderate (10's of m), and small (<10 m) vertical displacements, respectively. The sediments are weak enough to be excavated by hand, but strong enough to form vertical cliffs. They encompass a wide

range of structural complexity, host sediment types, and bed thicknesses, and therefore are an excellent field laboratory with which to address the objectives of this study. The methods used included detailed (cm- to m-scale) and sketch mapping of natural and excavated outcrops, microstructural study and grain-size measurement with image processing and analysis techniques, field and laboratory permeability measurement, and integration of structural and permeability data into analytical and numerical flow models.

1.3. Organization

The body of this dissertation is organized into four chapters, each of which is written as a separate journal article. This introduction and a conclusion chapter define the goals of the work and summarize the main findings and their implications. A brief overview of each of the four main chapters follows.

Chapter Two: Co-author Laurel B. Goodwin; submitted to the Geological Society of America Bulletin. This chapter documents the structures and internal architecture of the Sand Hill and Santa Ana normal faults, with emphasis on the mixed zones, which are characteristic of the faults in poorly lithified sediments studied. It includes outcrop observations and quantitative microstructural measurements. I synthesize these data with inferences about the consolidation history of the fault into a model for the development of mixed zones in normal faults.

Chapter Three: Co-author Laurel B. Goodwin; in review at The Journal of Structural Geology. I use grain-size measurements, back-scattered electron imaging of thin sections, and surface textural observations of individual grains to document the occurrence of cataclasis in faults in poorly lithified sediments, its mineralogical dependence, and how its nature systematically varies with intensity and/or localization of deformation within the fault zones. The results are interpreted as an example of controlled particulate flow.

Chapter Four: Co-authors Laurel B. Goodwin and John L. Wilson; published in Geology (Rawling et al., 2001). In this chapter I contrast the basic structures and internal architecture of faults in crystalline and lithified sedimentary rocks and normal faults in poorly lithified sediments. The regional hydrologic significance of both is assessed with equivalent permeability calculations based on groundwater flow models of idealized normal faults of both types.

Chapter Five: I assess the differences in high-angle normal fault-proximal fluid flow patterns related to faults in crystalline and lithified sedimentary rocks and faults in poorly lithified sediments. Two-dimensional finite-element models of horizontal flow regimes within faulted, fining-upward, sedimentary sequences are used to investigate the relative effects on flow patterns of different fault-zone permeability structures, levels of internal structural complexity, juxtaposition of strata, and stratal thickness variations.

CHAPTER 2. STRUCTURAL DEVELOPMENT AND IMPLICATIONS FOR FLUID FLOW OF MIXED ZONES WITHIN FAULTS IN POORLY LITHIFIED SEDIMENTS*

2.1. Abstract

We integrate field and microstructural observations of faults in poorly lithified sediments of the Albuquerque Basin, New Mexico, USA to understand the development of a structurally and hydrologically heterogeneous fault-zone architectural element, the mixed zone. Mixed zones are not present in brittle faults in crystalline and well-lithified sedimentary rocks. However, we infer that sediment was initially incorporated into mixed zones by processes typical of brittle faults, and may be continually added throughout the movement history of the fault. Mixed zones exhibit macroscopically ductile structures formed by penetrative particulate flow. These are overprinted by deformation bands, which represent a later, more localized style of deformation. These structures and overprinting relationships are consistent with the inferred consolidation

* Geoffrey C. Rawling and Laurel B. Goodwin, submitted to Geological Society of America Bulletin

history of the faults and host sediments. Recognition of mixed zones is important not only for interpreting the deformational history of faults - - they may also affect groundwater flow and act as hydrocarbon traps.

2.2. Introduction

With the recognition of the impact of faults on subsurface flow regimes (Smith et al., 1990; Bredehoeft et al., 1992; Knipe, 1993; Haneberg 1995), much work has focussed on characterizing the internal structure and hydrologic properties of brittle fault zones (Underhill and Woodcock, 1987; Forster and Evans, 1991; Antonellini and Aydin, 1994; Antonellini and Aydin, 1995; Caine et al., 1996; Evans et al., 1997; Caine and Forster, 1999; Sigda et al., 1999; Chapter 4). Field studies of brittle fault zones in crystalline and lithified, low-porosity sedimentary rocks have resulted in the identification of a characteristic internal architecture defined by the spatial arrangement of architectural elements that has been summarized in a conceptual fault zone model (Chester and Logan, 1986; Chester et al., 1993; Caine et al., 1996). The basic structural unit of faults in these rocks is the fracture, whereas in high-porosity sandy sedimentary rocks it is the deformation band (a narrow, tabular zone of displacement, compaction, and/or cataclasis; cf. Aydin, 1978; Antonellini et al., 1994; Goodwin et al., 1999). In both cases, the fault zone as a whole is comprised of three architectural elements: (1) The core zone is the locus of most of the deformation, and is composed of gouge or cataclasite. It is flanked by (2) damage zones with abundant fractures or deformation bands. (3) The fault zone proper is embedded in protolith with no fault-related deformation structures.

Faults in sandy, poorly lithified sediments are analogous to brittle faults in high-porosity sedimentary rocks in that they have deformation bands as a basic structural unit. However, studies of faults in poorly lithified sediments within basins of the Rio Grande rift, New Mexico, USA have identified differences in fault-zone internal architecture when compared to the model described above (Mozley and Goodwin, 1995; Heynekamp et al., 1999; Sigda et al., 1999; Chapter 4). The fault core is a foliated clay layer as thick as 10 centimeters. Gaps in the clay core are rare, even where the host sediments are dominantly sand (Heynekamp et al., 1999). Where displacement is greater than local average bed thickness, a new architectural element – the mixed zone – develops between the core and damage zones. It is characterized by compositional variability and highly heterogeneous deformation, from intact but rotated and attenuated bedding to intermixing of such disparate sediment types as clay and gravel by particulate flow and cataclasis during slip (Chapter 3). Mixed zones are similar to fault cores in that they are composed of highly deformed material; however we find that they are lithologically, structurally and hydrologically distinct from both the core and damage zones (Heynekamp et al., 1999; Chapter 4). The boundary between the mixed and damage zones is defined by displacement greater than local average bed thickness (Heynekamp et al., 1999). Relict sedimentary structures, such as cross beds, are locally preserved in the mixed zone but are absent from the core. Similar structures and overall fault-zone geometry have been observed in small-displacement faults in poorly lithified sediments in German coal mines (Weber et al., 1978) and in Tertiary growth faults along the Texas Gulf Coast (Berg and Avery, 1995). Similar deformation structures, intermixing of disparate sediment types,

and development of compositional and structural foliations have been described in tills and glacially deformed sediments (e.g., Benn and Evans, 1996).

In Chapter 4, we investigate the hydrologic properties of the Sand Hill fault, which cuts poorly lithified Tertiary sediments in the Albuquerque basin of the Rio Grande rift in central New Mexico. A central conclusion of Chapter 4 is that the mixed zone has highly heterogeneous hydrologic properties, with permeability that may vary over six orders of magnitude. Mixed-zone heterogeneity necessarily challenges our ability to accurately simulate the hydrologic properties of the fault zone as a whole. To the degree that the variability of hydrologic properties is controlled by structural and compositional heterogeneity, an understanding of the geologic controls on permeability in mixed zones will enhance our ability to accurately assess the impact of fault zones on fluid flow.

Many important structural questions remain to be answered about the nature of mixed zones in faults in poorly lithified sediments, and the structural evolution from single deformation bands to a differentiated and mappable architectural element with complex internal structure is as yet unstudied. In addition to being fundamental to our understanding of how fault zones in poorly lithified sediments evolve, answering these structural questions is necessary prior to attempting more detailed hydrologic studies. For example, how do mixed zones form? What are the important deformation mechanisms at the micro- and macro-scale? Are these deformation mechanisms similar to those that have been proposed for brittle faults in lithified rocks? Is there a consistent sequence in the development of individual structures within the mixed zones? What is the influence, if any, of tectonic burial and/or exhumation on this sequence of development?

The purpose of this paper is to provide detailed descriptions of the macroscale (outcrop) and microscale internal structures of mixed zones and identify the deformation mechanisms operative during faulting and mixed zone development in poorly lithified sediments. Our investigation has focussed on several outcrops along two normal faults within the Albuquerque Basin of the Rio Grande rift, central New Mexico. The study outcrops span a wide range of host fluvial sediments and bedding thickness, fault zone thickness and internal complexity, and vertical displacement.

Our observations suggest that deformation of sediments is initially accomplished by incorporation of masses of material into the fault zone by splitting of the propagating fault tip (tip-line bifurcation) and shearing off of the corners of tilted beds (asperity bifurcation). Progressive deformation within the fault zone is accomplished by disaggregation and pervasive particulate flow, accompanied to varying degrees by cataclasis in sandy sediments. This results in macroscopically ductile structures, in the sense of distributed deformation without extensive localization (cf. Rutter, 1986). In sandy sediments, these structures are eventually overprinted by deformation bands, both isolated and in networks. This localized style of deformation is accompanied by more extensive cataclasis. Cataclastic shear zones of coalesced deformation bands form either as localized high strain zones during mixed zone development or after mixed zone development as deformation becomes more localized. The structures and overprinting relationships we observe are consistent with the inferred consolidation history of the host sediments and with predictions from critical state soil mechanics theory, which indicate that deformation should localize with increasing consolidation. These results have implications for the interpretation of fault-zone deformational history; e.g., structures

formed before complete lithification may be preserved and/or overprinted by later deformation. Comparison with other studies suggests that homogenization of different sediments types in mixed zones allow them to strongly affect the ability of faults to act as traps in hydrocarbon reservoirs.

2.3. Study Areas

Two faults were investigated for this study. Both cut poorly lithified sediments of the Tertiary Santa Fe Group which, except where cemented by calcite, are friable and easily disaggregated. The sediments are weak enough to be excavated by hand, but strong enough to form vertical cliffs. The first is the fault with a clay core studied by Sigda et al. (1999). This fault is located near the center of the Albuquerque Basin. It appears to be a southern extension of, or splay from, the Santa Ana fault (Sigda et al., 1999; S. Connell, written commun., 2001), which is a major intrabasinal, down-to-the-east, normal fault that is well exposed at the northern margin of the basin (Pazzaglia et al., 1999). It is exposed in the wall of an arroyo in the city of Rio Rancho, NW of Albuquerque (Figure 1). This fault is believed to record approximately 10 m of vertical displacement and cuts sediments of the upper Santa Fe Group (Sigda et al., 1999). It illustrates a level of complexity above single deformation-band faults, with nascent but readily identifiable damage, mixed, and core zones.

The second fault studied is the Sand Hill fault. It is one of the major normal faults bounding the Rio Grande rift, and marks the western margin of the Albuquerque Basin (Hawley et al., 1995; Figure 1). It is a growth fault juxtaposing synrift sediments of the Pliocene-Pleistocene upper Santa Fe Group against middle Miocene to Oligocene

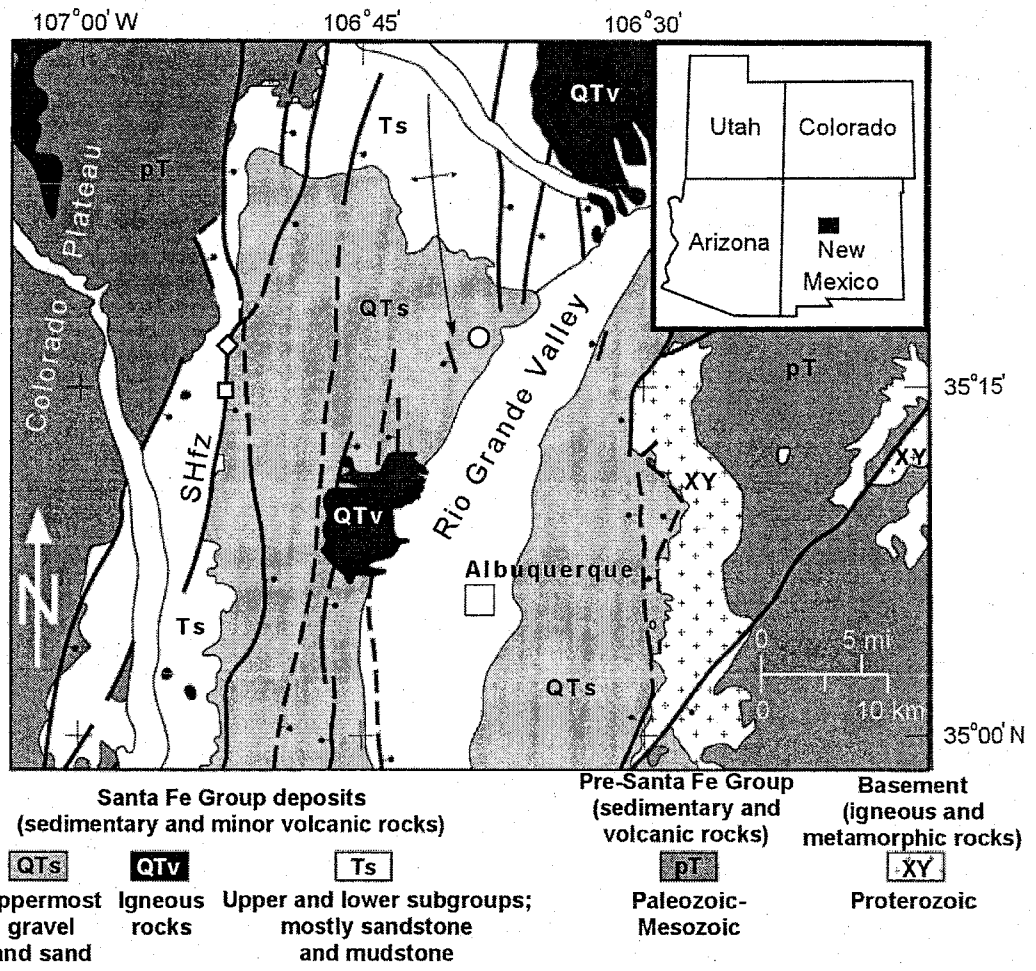

Figure 1. Study sites in Albuquerque Basin of Rio Grande rift. Inset shows regional location. Sand Hill fault zone (SHfz) sites are Shooting gallery (square) and Waterfall (diamond). Santa Ana fault site is circle. Faults are generalized; not all faults are shown. Modified from Hawley et al. (1995) and Hawley (1996) by S. Connell.

sediments of the lower and middle Santa Fe Group, with displacement increasing from ~10 to ~600 m down dip (Connell et al., 1999; Tedford and Barghoorn, 1999). Stratigraphic constraints (S. Connell, written communication, 2001) and vitrinite reflectance data (W. Shea, personal communication, 1998) suggest that current exposures of the Sand Hill fault were never buried more than 1 km. The two study outcrops are portions of those mapped at 1:100 scale by Heynekamp et al. (1999). The northern outcrop (the Waterfall) is of a portion of the fault where the fault zone as a whole is extremely wide (~20m). The southern outcrop (Shooting Gallery) has vertical exposure >100 m and the fault zone thickness varies from ~1m at the top of the outcrop to ~10 m in the middle of the outcrop. Vertical displacement (throw) at the structural levels currently exposed along the Sand Hill fault is approximately 200 m (Tedford and Barghoorn, 1999). This large-displacement fault exhibits great structural complexity and extensive development of damage, mixed, and core zones.

2.4. Macroscopic Fault Zone Structures of the Santa Ana Fault

Figure 2 is a photo and outcrop map of the Santa Ana fault. The fault zone varies from less than a half meter wide at the base of the outcrop to slightly more than a meter at the top. Other than a subsidiary fault in the hanging wall, structures in the damage zone are sparse, with only a few isolated deformation bands present. Near the top of the outcrop there is slight curvature of clay-rich beds in the hanging wall and of finely laminated clay-rich sand beds in the footwall immediately adjacent to the fault. The subsidiary fault is a ~ 2 cm wide zone of coalesced deformation bands in the thick sandy

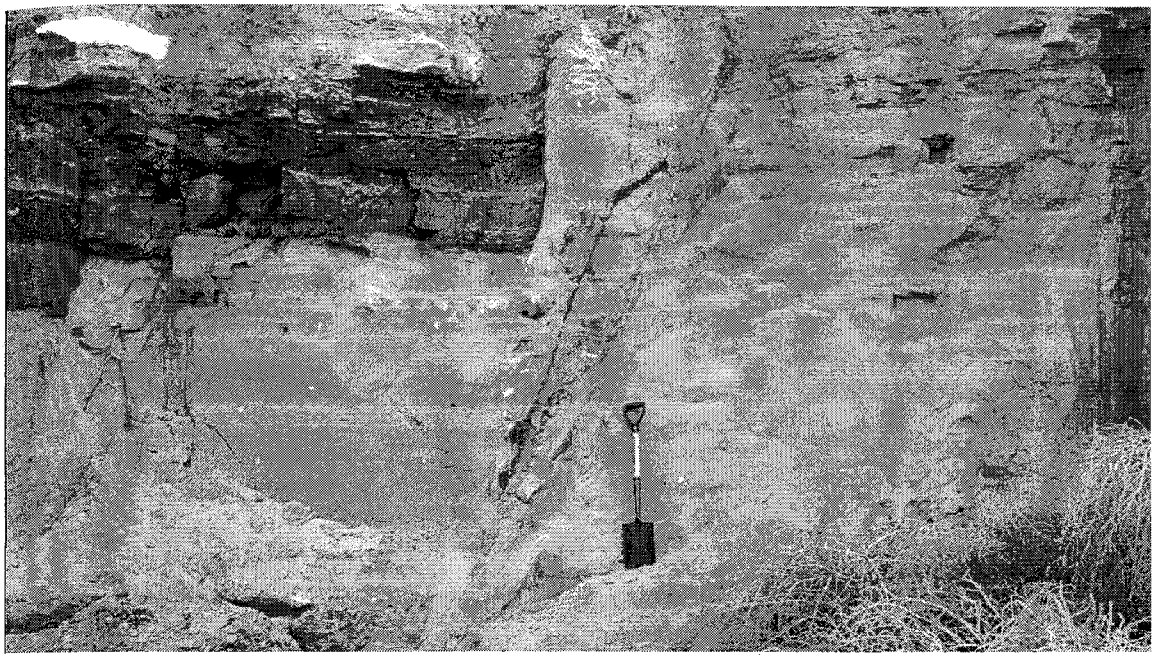

a

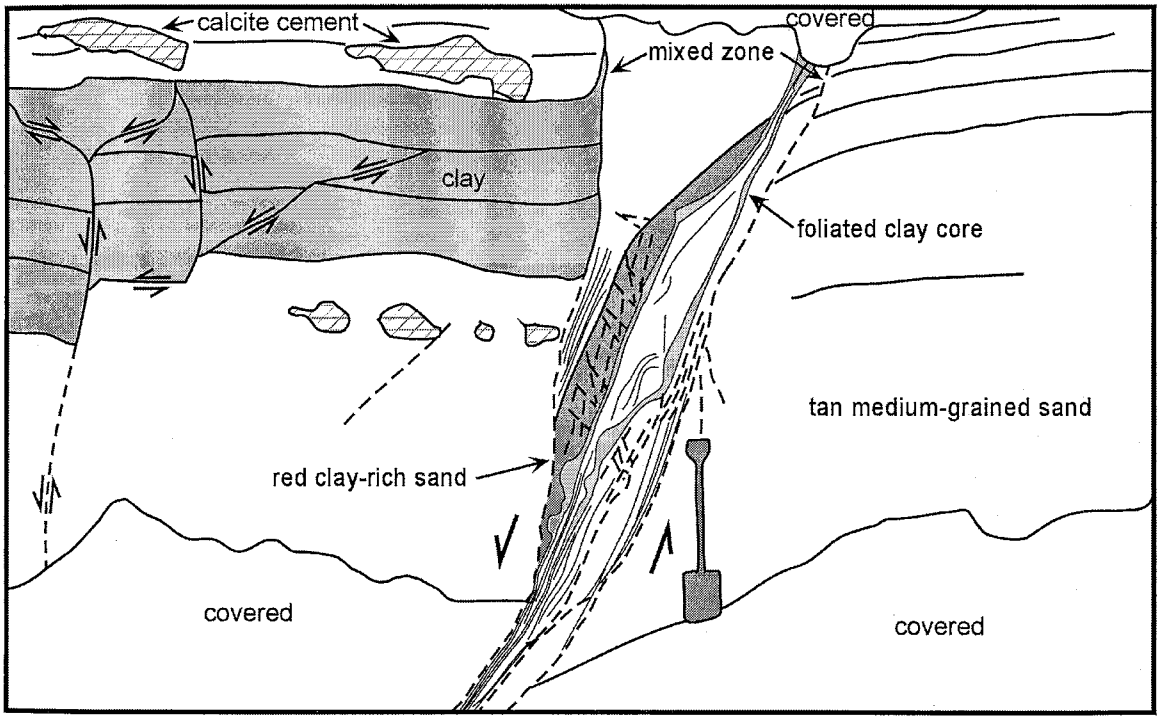

b

Figure 2. a) Photograph and **b)** sketch from photograph of Santa Ana fault outcrop. Thick lines are bedding, thin lines are foliations, dashed lines are deformation bands. View is to the south. Shovel is 1 m high. See text for discussion.

bed at the base of the outcrop that bifurcates into discrete, slickensided slip surfaces in the thick clay-rich layers at the top of the outcrop. These slip surfaces are similar to those in the Sand Hill fault zone. Vertical displacement on the subsidiary fault is ~ 0.5 m.

Most of the variation in the thickness of the main fault is due to variation in mixed zone thickness. The mixed zones are composed of two sediment types: a tan, medium-grained sand and a reddish, clay-rich sand. The tan medium-grained sand is similar in color and outcrop surface texture to the undeformed sand on either side of the fault. However, the mixed zones are intensely internally deformed, with a fault-parallel foliation defined by compositional and textural layering and clusters or shear zones of coalesced deformation bands (hereafter referred to as deformation band shear zones, or DBSZ) overprinted with individual deformation bands in a Riedel (R_1) orientation (cf. Logan et al., 1992; Figure 3). This is a pattern observed at all of the outcrops in this study: deformation bands, either singly or on clusters, may crosscut each other, but they always overprint a macroscopically ductile foliation defined by compositional layering. These features are better developed in the tan medium-grained sand of the footwall than in the red clay-rich sand of the hanging wall. The mixed zone contacts and contacts with the clay core are commonly slightly stepped, due to offset along the R_1 deformation bands (Figure 3). The boundaries between the footwall and hanging wall mixed zones and their respective damage zones are shear zones of coalesced deformation bands (Figure 4).

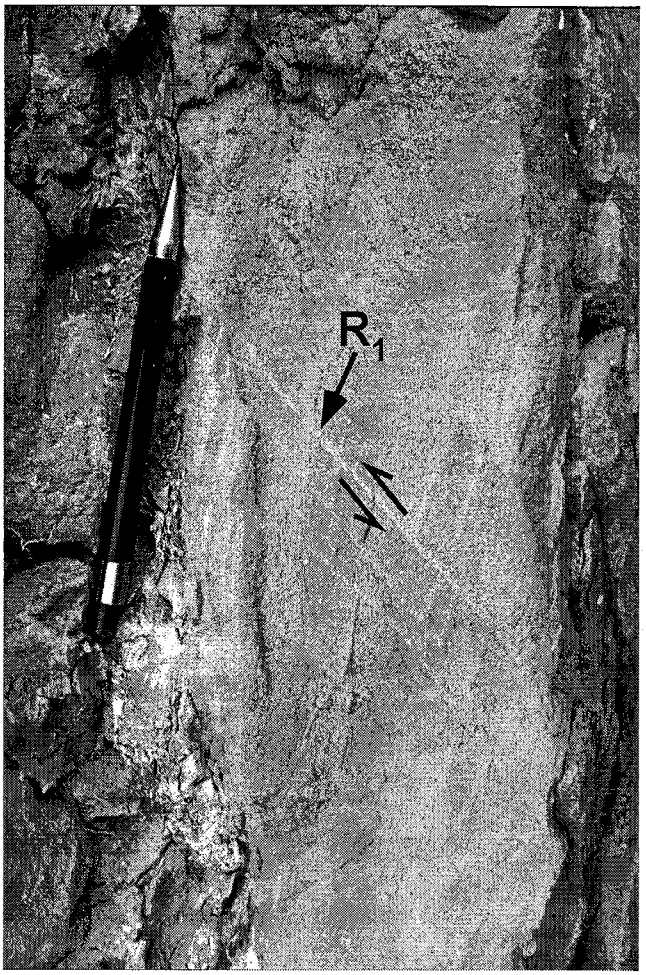

Figure 3. Individual and clustered fault-parallel deformation bands offset by deformation bands in the R_1 orientation (see Figure 5f). Pencil is 10 cm long. Relative movement is left (southeast) side down.

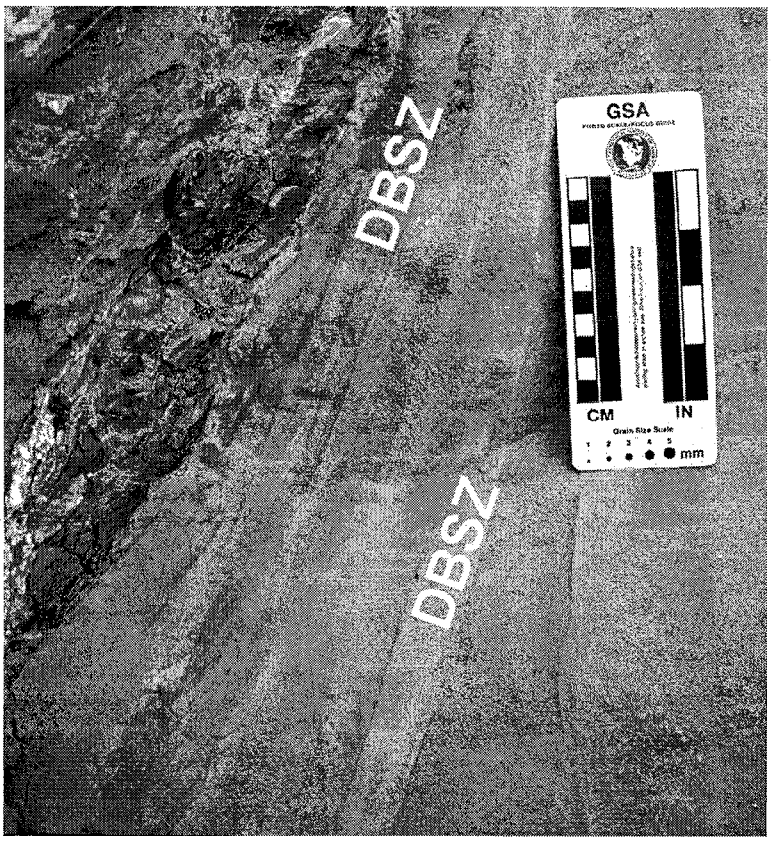

Figure 4. Shear zone of coalesced deformation bands (DBSZ) separating footwall mixed zone from footwall damage zone. Red foliated clay is visible to left of DBSZs. Relative movement is left (southeast) side down.

2.5. Macroscopic Fault Zone Structures of the Sand Hill Fault

2.5.1. Fault Zone Architecture

Heynekamp et al. (1999) described the fault-zone architecture and controls on fault-zone width of faults in poorly lithified sediments based on observations of the Sand Hill fault. The general fault-zone architecture is summarized here and in the schematic cross-section in Figure 5. Where the fault cuts thick, clay-rich (>20% clay) beds or thin, interlayered sandy (≤ 20% clay) and clay-rich beds, the fault zone is narrow and structurally simple (Figures 6 and 7). Where the fault cuts beds that are ≥ 80% sand and/or gravel, the fault zone is wide and structurally complex (Figures 8 and 9). Heynekamp et al. (1999) observed that where the adjacent sediments are coarse grained, the hanging wall mixed zone is typically extensively cemented with sparry calcite.

2.5.2. Planar Structures

We measured the orientations of macroscopic structural features and the main fault (identified as the core zone in most outcrops) at numerous locations along an approximately 9 km strike-parallel traverse of the Sand Hill fault. Figure 5 shows compiled orientation data from multiple outcrops for deformation bands and slip surfaces (minor faults) within the footwall damage and mixed zones, and clay foliation within the core of the Sand Hill fault zone. The aforementioned slip surfaces occur in clay and very clay-rich sand. In fresh, moist excavations and in rewetted samples in the laboratory, the slip surfaces appear as striated planes. They are planes of weakness, as samples often break apart along these surfaces when handled. After desiccation and contraction of the host material, they appear similar to shear fractures. However, under saturated conditions

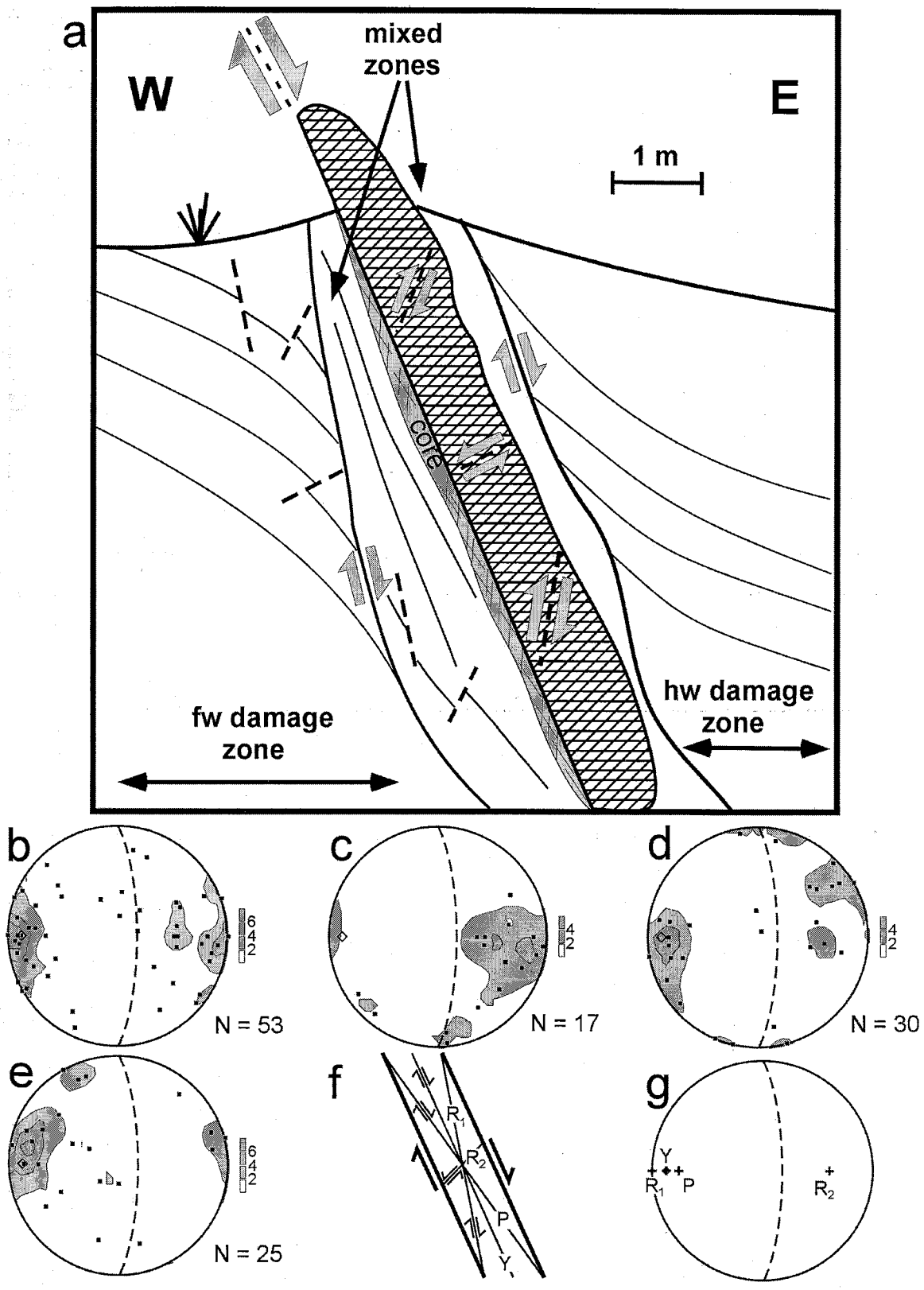
a
W
E
mixed
zones
1 m
core
fw damage
zone
hw damage
zone
b
N = 53
c
N = 17
d
N = 30
e
N = 25
f
R1
R2
P
Y
g
Y
R1
P
R2

Figure 5. (following page) **a)** Schematic cross-section of Sand Hill fault zone showing architectural elements and representative orientations and senses of movement of populations of deformation bands (dashed lines). Thin lines are traces of bedding within damage zones and compositional layers within mixed zones. Cross-hatched region represents cemented zone in coarse-grained sediments. Based on observations from this study and Heynekamp et al. (1999). Lower hemisphere equal area plots of poles to: **b)** normal slip deformation bands; **c)** reverse slip deformation bands; **d)** unknown slip deformation bands; and **e)** foliation in clay core. Data compiled from four outcrops of Sand Hill fault. Fault strike at each outcrop rotated to 000° and plotted with average dip of 76° E (dashed great circle; open diamond is pole to fault). Structural data for each outcrop rotated with local fault trend. Contours are in multiples of uniform distribution by the method of Starkey (1977). White area therefore represents less than two times uniform distribution. **f)** Orientations of and **g)** poles to brittle shear zone structures, after Logan et al. (1992).

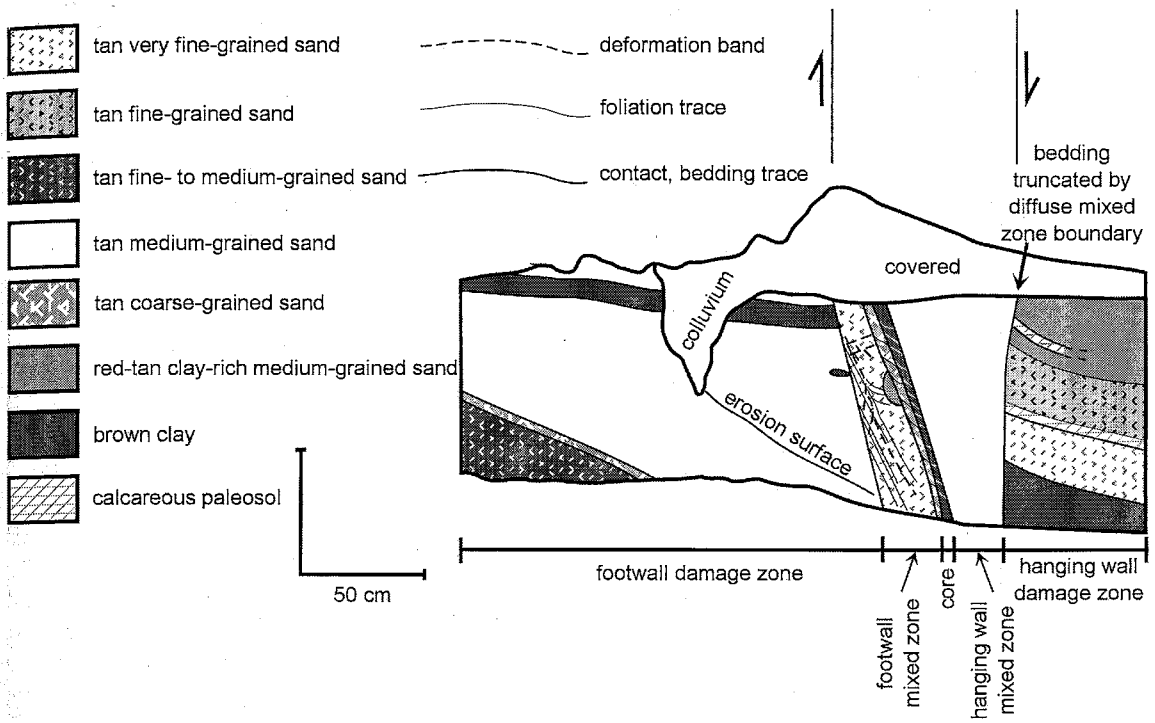

Figure 6. Cross-section of upper portion of Shooting Gallery outcrop.

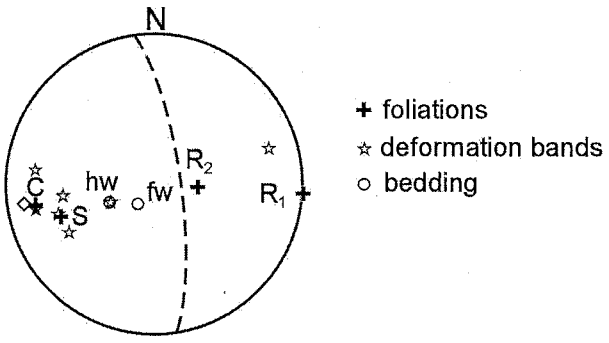

Figure 7. Lower hemisphere equal area net of poles to planar structures at upper Shooting Gallery outcrop. Great circle is contact between clay core and footwall mixed zone.

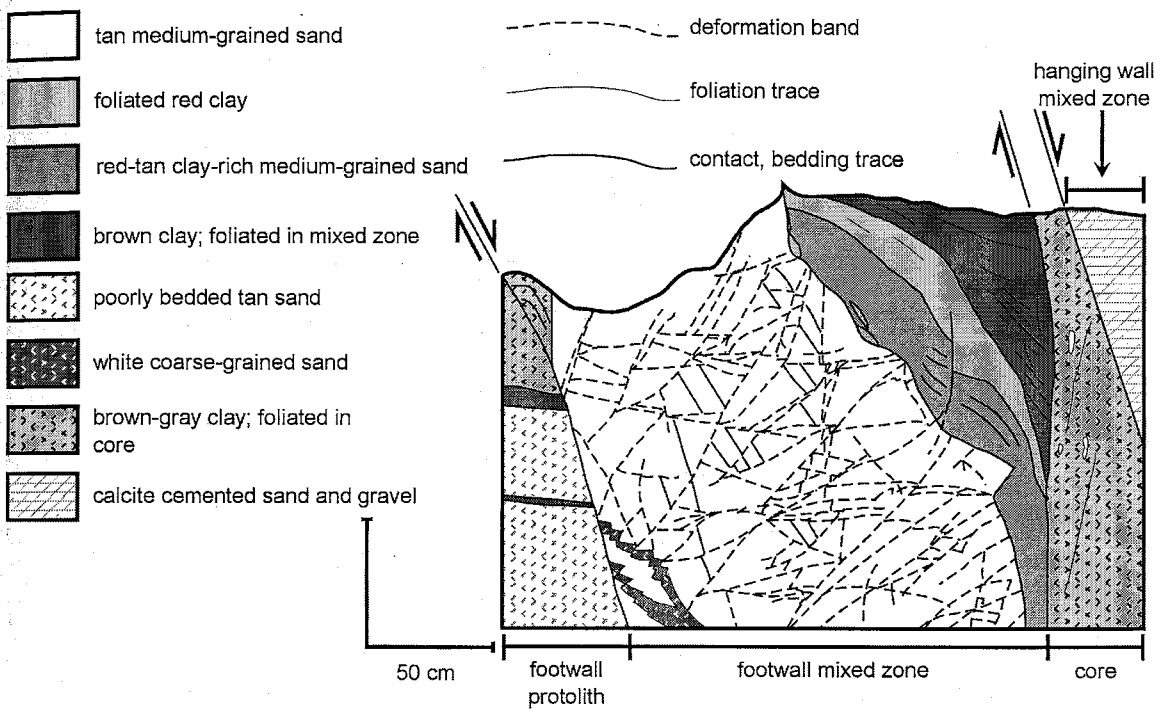

Figure 8. Cross section of lower portion of Shooting Gallery outcrop.

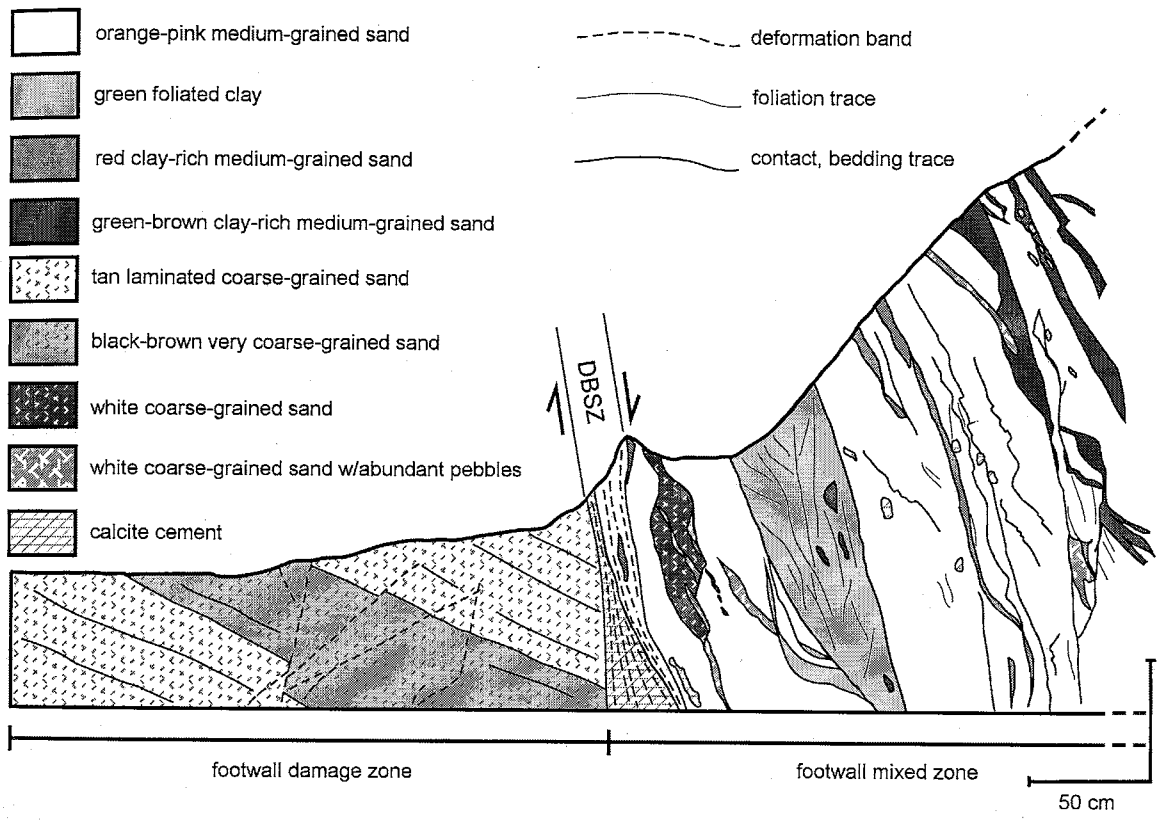

Figure 9. Cross section of west half of Waterfall outcrop. The large lenticular pod of clay pinches out abruptly both up and down dip. Fault core is east (right) of mapped portion of outcrop. DBSZ is deformation band shear zone.

they are unlikely to have any aperture. Due to poor exposure, we have few observations of the hanging wall of the Sand Hill fault, except where the hanging wall mixed zone is well cemented. Except for the lower outcrop at the Shooting Gallery (Figure 8), the majority of the deformation bands measured were within the damage zone and the slip surfaces were largely within the mixed zone. The foliation within the clay core is closely spaced, non-planar, and anastomosing, and isolates lozenge-shaped pods of clay. Because they are not planar, measurement of the orientation of clay foliation surfaces is difficult. We have attempted to measure the mean orientation of surfaces representative of those exposed in outcrop, recognizing that this approach does not capture the full range in orientation. However, in general, the core foliation is dominantly fault parallel and steeply dipping (Figure 5e).

Deformation bands within the damage zone are usually either isolated or form open networks (Figure 8). Complex arrays of deformation bands are more common within the mixed zone (Figure 8). Most deformation bands are subparallel to the local trace of the fault. Normal-slip deformation bands form dominantly steeply east- and west-dipping populations (Figure 5b). Reverse-slip deformation bands form a moderately to steeply west-dipping population (Figure 5c). Deformation bands of unknown slip sense are both steeply east-northeast- and west-southwest-dipping (Figure 5d). Relative to the steeply east-dipping, down-to-the-east Sand Hill fault, the east-dipping population of normal-slip deformation bands correspond in orientation and slip sense to R_1 or Y shears. The west-dipping normal-slip deformation bands correspond in orientation and slip sense to R_2 shears (compare Figure 5b with Figures 5f and g). The reverse slip deformation bands (Figure 5c) do not correspond to any of the ideal fault zone foliations of Logan et

al. (1992). They appear to accommodate down dip extension of the footwall sediment (cf. Figure 5a).

2.5.3. Outcrop Maps

Upper Shooting Gallery – Narrow Fault. In the upper portion of the Shooting Gallery outcrop the fault juxtaposes thickly bedded (>20 m) sediments with >50% clay in the hanging wall against thinner bedded (≤6 m) sediments with < 50% clay in the footwall (figure 7 of Heynekamp et al., 1999). Figure 6 is a cross section of the fault mapped at a scale of 1:10. The fault zone in this location is less than 1 m wide, with the only evidence of a damage zone being slight bed rotation and bedding-parallel slip surfaces between sand and clay layers in the hanging wall.

The hanging wall mixed zone consists of largely structureless sand which forms a gradational contact with the damage zone, whereas the contact with the core is sharp (Figure 6). The footwall mixed zone forms a sharp boundary with apparently undeformed, but slightly tilted, footwall beds. Immediately adjacent to this boundary are steeply dipping S- and C-foliations defined by compositional bands of sand, visible as variations in color, grain size, and surface texture on the excavated, brushed surface (Figures 6 and 7, 10 and 11). These are locally offset by C'-surfaces (Figures 6 and 11). Small areas of relict bedding are present as sigmoidal pods of sand (Figure 10).

The clay core has a well developed, penetrative foliation. It is composed of elongate lenses of clay oriented at ~20° to the main fault. Some are sigmoidal in shape, with ends that rotate into parallelism with the main fault orientation. Others are truncated by discrete, more steeply dipping, fault-parallel slip surfaces. The overall geometry is

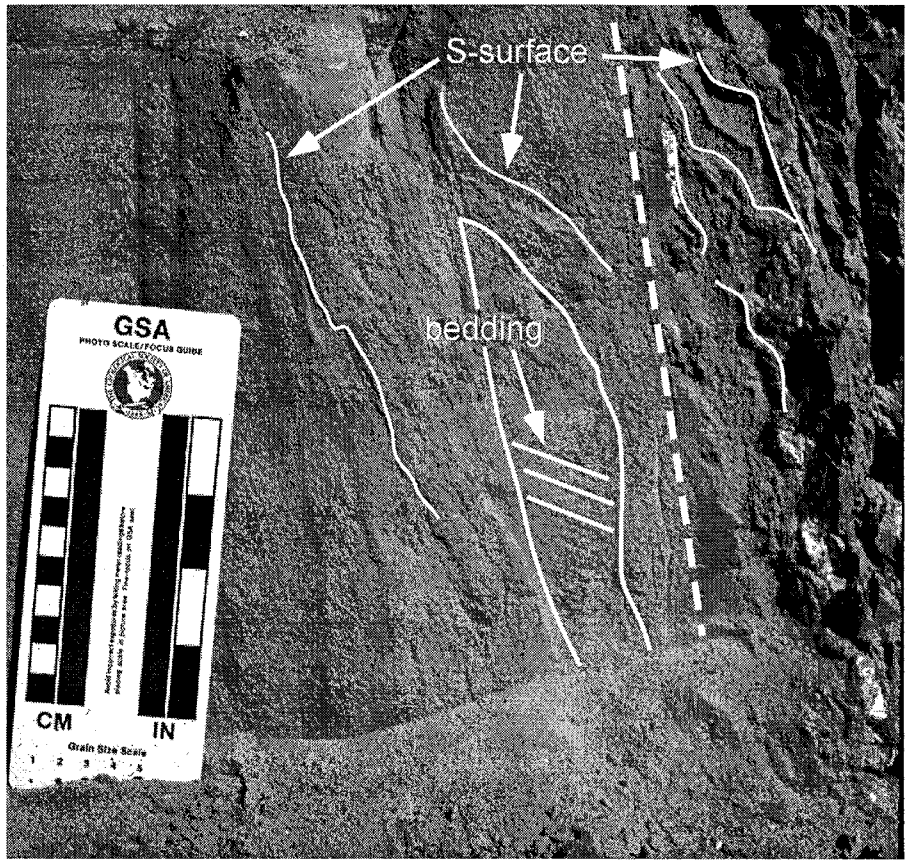

Figure 10. Foliations in footwall mixed zone of upper Shooting Gallery outcrop (Figure 6). Dashed line marks contact between clay and sand core and largely sand footwall mixed zone. Compositional foliations in sand and clay shown by curved white lines. Three straight lines indicate relict bedding within sigmoidal pod of coarse sand. Image viewed to north, with east (right) side down.

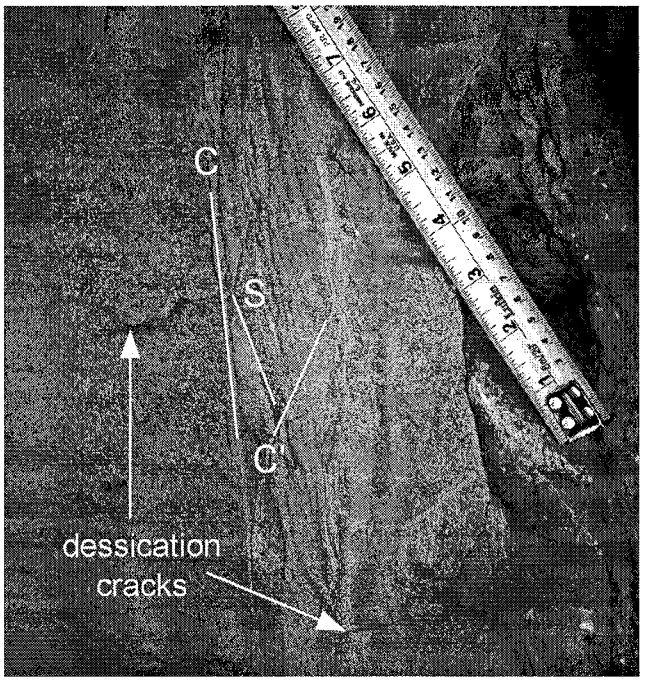

Figure 11. Compositional layers with S-, C-, and C'-surfaces indicated. Cracks are due to desiccation of relatively clay-rich areas after excavation. Image viewed to north, with east (right) side down.

similar to S-C fabrics from deeper crustal rocks (Figure 10; cf. Lister and Snoke, 1984), and is particularly obvious where sand and clay are both present (Figure 10).

Lower Shooting Gallery – Intermediate Width Fault. In the lower portion of the Shooting Gallery, the fault juxtaposes thickly bedded (several tens of meters) sediments with ≤ 20% clay in the hanging wall against thinner bedded (2-6 m) sediments with either ≤ 20% clay or > 50% clay (figure 7 of Heynekamp et al., 1999). The fault zone in this location is approximately 10 m wide. Figure 8 is a cross section of most of the fault zone mapped at a scale of 1:10.

The hanging-wall mixed zone consists of coarse sand and gravel cemented by calcite. Rotated and attenuated gravel beds are prominent, and are commonly cut by R_1 and R_2 shears oriented as shown in Figure 5a. The contact with the clay core is sharp. The clay core has little included sand and is strongly foliated. The clay-rich layers in the footwall mixed zone exhibit macroscopically ductile deformation, tilted beds, and variable thickness but an overall progressive thinning of beds with increased dip. Bedding- and fault-parallel foliations are less well developed than those in the core. The tan medium-grained sand has an intricate network of deformation bands. Three orientations of deformation bands can be identified: a subvertical set, and two orientations that may represent a conjugate pair, with one member of the pair very shallowly east-dipping, and the other dipping west ~45°. Bedding is only locally evident, and is tilted significantly toward the main fault. Where sand is juxtaposed against sand, the contact of the footwall mixed zone with the protolith is a thin zone of deformation bands; where clay is juxtaposed against clay, it is a discrete slip surface.

Waterfall – Wide Fault. At the Waterfall site, the fault juxtaposes at least 10 m of sediment with ≤ 5% clay in the hanging wall against sediment with < 20% clay in the footwall (figure 10 of Heynekamp et al., 1999). The fault zone is ≥ 20 m wide. Figure 9 is a partial cross section of the footwall at this site mapped at a scale of 1:10. Just east of the map is the clay core and extensively cemented hanging-wall mixed zone.

The hanging-wall mixed zone is composed of coarse sand and gravel cemented by calcite. It is much more resistant to erosion than the adjacent unlithified sediment and stands up as a prominent wall overhanging the footwall. The footwall mixed zone has grain sizes ranging from gravel to clay, and has been penetratively deformed, as shown by approximately fault-parallel compositional banding and extensive grain-scale mixing. Localized shear zones contain compositional segregations of sand and clay, typically with a sigmoidal shape that records the down-to-the-east fault kinematics. Relict sedimentary structures such as rotated bedding are present (Figure 12). Foliation is well developed in sand and clay and the foliation in sand is locally overprinted by deformation bands. Down dip lineations defined by the long axes of sand grains are common on sand foliation surfaces. The contact with the footwall damage zone is a shear zone of coalesced deformation bands (DBSZ) partly cemented with calcite (Figure 9). DBSZs (Figures 3 and 4) are distinguishable from other high strain zones in the mixed zone (Figure 12) by their more indurated nature and raised relief on excavated, brushed outcrops.

Figure 12 also illustrates another type of structural complexity within the mixed zone. The coarse-grained tan sand with scattered black clasts and white caliche clasts in the right half of the image is the upper tip of a large sigmoidal pod of deformed sediment.

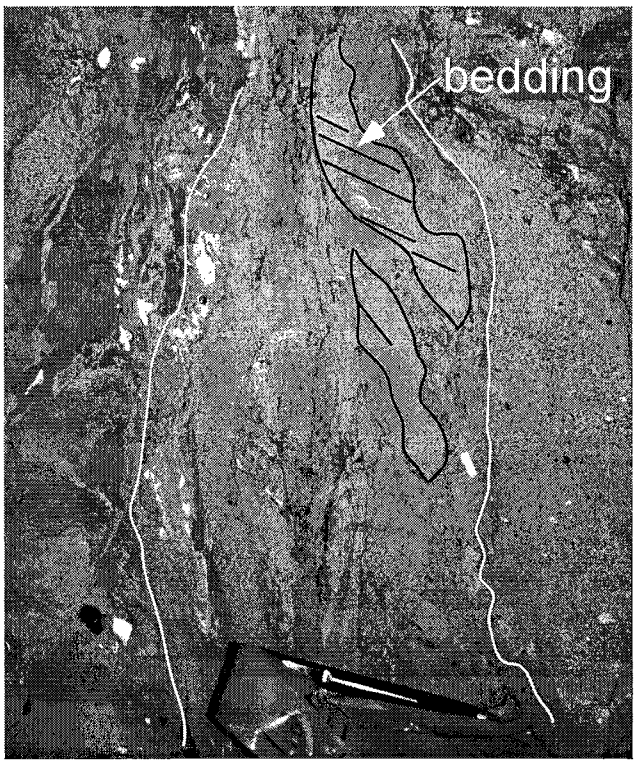

Figure 12. Compositional banding and foliation in the Waterfall outcrop. Extremely attenuated bedding in central shear zone bounded by white lines separates red, clay-rich sand with tan sand inclusions on left from tan coarse sand on right. Black lines delimit sigmoidal pods of sand in central high strain zone with relict bedding indicated. Pencil is 10 cm long. Image viewed to north, with east (right) side down.

This sediment is compositionally identical to sediments within colluvial wedges that are abundant in the hanging wall along the trace of the Sand Hill fault. However, the entire field of view of the photo is within the footwall mixed zone; the clay core of the fault is to the right (east) of the photo and separates the footwall mixed zone from the hanging wall mixed zone and colluvial wedge sediment in the undeformed hanging wall. The sediment in the left portion of Figure 12 is similar to adjacent sediments in the footwall. This is an example of local incorporation into the fault of hanging wall sediment and its subsequent deformation. We interpret this hanging-wall sediment currently residing in the footwall mixed zone as recording a slip-surface bifurcation during faulting.

2.6. Microstructural Observations

The focus of our microstructural observations in this study has been on grain orientations and pore geometry, as these parameters may be expected to document grain movements and reorganization due to particulate flow during faulting.

2.6.1. Sample Description and Preparation

We collected oriented samples from undeformed fluvial (Beckner, 1996) footwall sand 10 m from the fault, a transposed layer within the mixed zone, a pod of sand in the core zone, and a DBSZ, all at the Waterfall outcrop. Although the amount of deformation accommodated by the fault-zone samples is unknown, the mixed-zone sand sample represents a lesser degree of deformation localization than either the core sand or the DBSZ. After impregnation under vacuum with low viscosity epoxy, oriented petrographic sections were prepared from each sample. Due to the poorly lithified and

fragile nature of the samples, plucking is noticeable in some of the undeformed sediment and DBSZ sections. The mixed-zone sand sections have minimal plucking. For the undeformed sediment sample, two sections were oriented 1) perpendicular (striking northeast-southwest) and 2) parallel to approximately horizontal bedding (Figure 13). Sections from the fault zone were prepared in three orientations (Figure 14a): A - parallel to foliation (either compositional layering or planes of deformation bands), with the section long axis parallel to the down dip lineation; B - perpendicular to foliation with the long axis of the section vertical and parallel to the down dip lineation, and; C- perpendicular to both the foliation and the down dip lineation. Preliminary observations were made with the petrographic microscope, then the sections were polished and examined on the electron microprobe in back-scattered electron (BSE) mode.

2.6.2. Grain Shape Preferred Orientations

We measured shape preferred orientations (SPO) on BSE images using Scion Image image analysis software. For each thin section, grains in four to eight randomly located images were measured at the same magnification. The greyscale images were processed to black (grains) and white (background) images and touching grains were separated manually in each image. The best-fitting ellipse to each of the larger, well preserved grains was calculated and the ellipse axial ratio, and long-axis length and orientation were recorded. Partially plucked grains, clay, small fragments and flakes derived from cataclasis of larger grains, and grains truncated by the edge of the image were not measured. The number of grains measured in each image ranged from about 30 to more than 100, depending on average grain size. The data were sorted, and grains with aspect ratios < 1.4 were discarded, as their orientations cannot be determined robustly

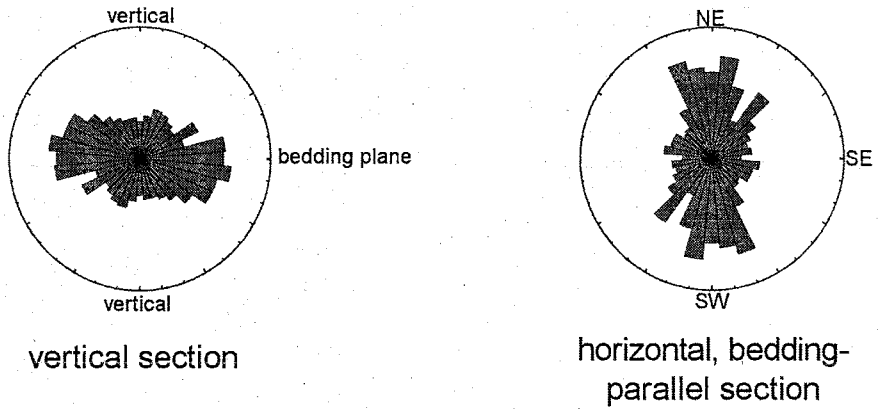

Figure 13. Rose diagrams of orientations of grain long axes in two perpendicular sections of undeformed sand. Number of data points and statistics are presented in Table 1.

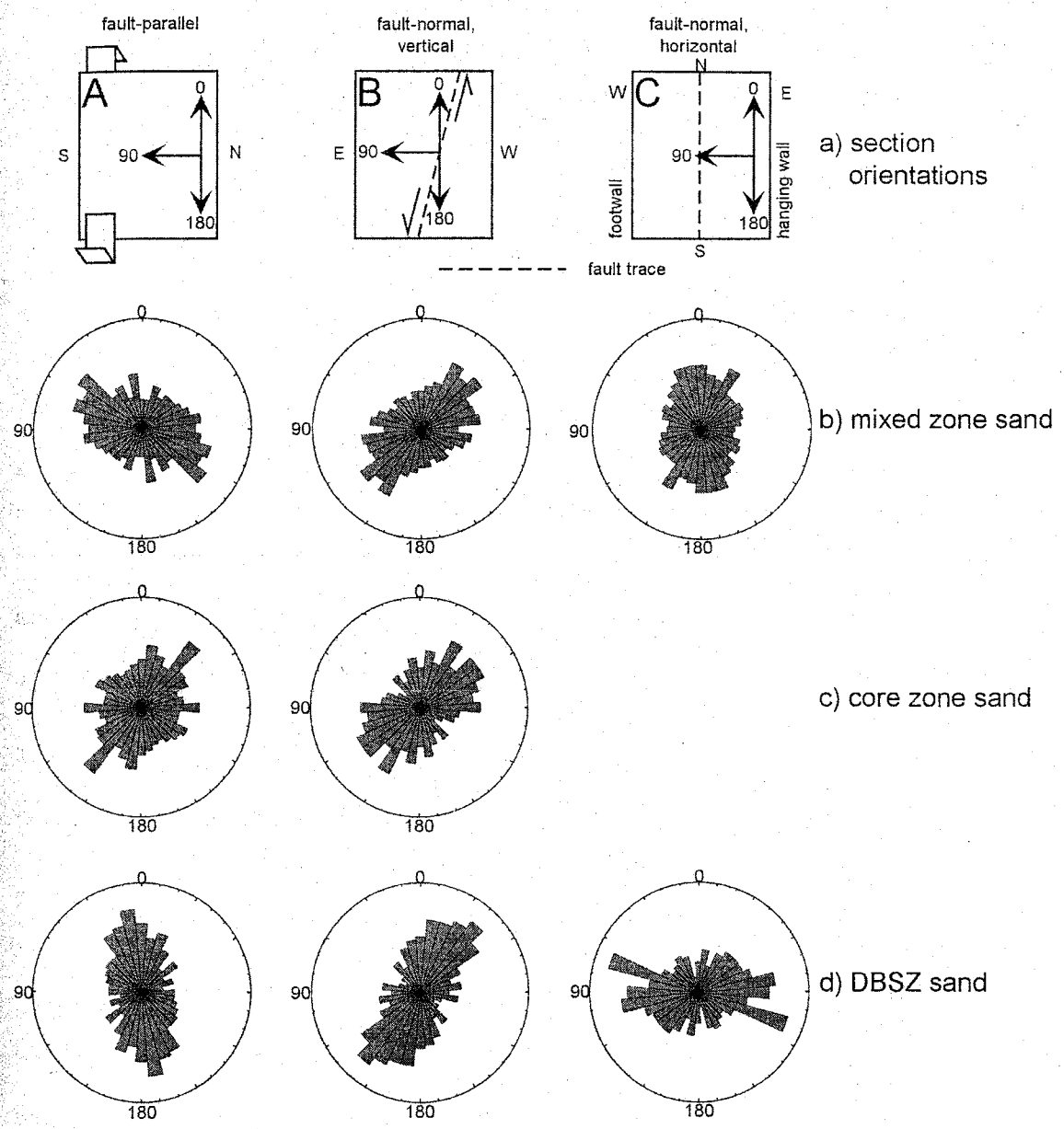

Figure 14. Rose diagrams of orientations of grain long axes in mutually perpendicular sections of deformed sands. Numbers of data and statistics are presented in Table 1. **a)** Orientation schemes for A, B, and C sections relative to fault and foliation. Data from sections of a given orientation are arranged in columns. **b)** Mixed-zone sand. **c)** Core-zone sand. **d)** Deformation-band shear-zone sand.

(Shelley, 1995; Cladouhos, 1999). The data are presented in Figures 13 and 14 and Table 1.

All samples show statistically significant grain-shape preferred orientations. Within the plane of bedding in the undeformed sample, the SPO is oriented NNE-SSW (Figure 13). This is consistent with the paleocurrent data of Beckner (1996). The SPO in the vertical plane is horizontal (Figure 13), indicating that grain long axes lie within the plane of bedding. In A sections from the deformed samples (Figure 14), SPOs are varied within the foliation plane, with the DBSZ sample having a down dip alignment. In B sections, all deformed samples have strong SPOs inclined to the fault, similar in orientation to a P-foliation or S-foliation (cf. Rutter et al., 1986; Logan et al., 1992). The angle of inclination is shallower for the DBSZ sample than for the mixed zone and core zone sands (Figure 14 and Table 1). C sections could only be made for the mixed zone and DBSZ samples. The SPO of the mixed-zone sample is aligned parallel to fault strike, whereas the SPO of the DBSZ sample is aligned normal to the foliation.

2.6.3. Pore Geometry

Two-point Correlation Functions. To characterize the pore geometry, we have calculated two-point correlation functions of the pore space from the same images that were used for measuring grain-shape preferred orientations. Two-point correlation functions are a compact, efficient, and robust way of describing the pore-space geometry of rocks and other porous materials in terms of their spatial correlation structure (Blair et al., 1996). The mathematical development of spatial correlation functions and a methodology for their calculation via image processing techniques may be found in

Table 1. Sample descriptions and grain-shape preferred orientation statistics.

Description	orientation of thin section*	n†	mean§	interval#
Footwall sediment	within bedding plane	401	049° (NE)	±16°
Footwall sediment	normal to bedding plane	507	99° (~horz.)	±19°
Mixed zone sand	**A** (foliation //, lineation //)	460	071°	±24°
Mixed zone sand	**B** (foliation ⊥, lineation //)	493	130°	±22°
Mixed zone sand	**C** (foliation ⊥, lineation ⊥)	548	178°	±25°
Core zone sand	**A** (foliation //, lineation //)	396	145°	±50°
Core zone sand	**B** (foliation ⊥, lineation //)	241	133°	±27°
DBSZ** sand	**A** (foliation //, lineation //)	229	010°	±23°
DBSZ sand	**B** (foliation ⊥, lineation //)	274	155°	±16°
DBSZ sand	**C** (foliation ⊥, lineation ⊥)	271	096°	±24°

* ⊥= normal, // = parallel; also see Figure 14.
† number of measurements.
§ mean direction of grain shape preferred orientation; reference scheme for fault samples in Figure 14.
# 95% confidence interval about mean direction.
** deformation band shear zone.

Berryman (1985). If we consider a rock as a two-phase medium, composed of pore space (phase I) and minerals (phase II), then the two-point correlation function of phase I (represented as $S_2(\mathbf{r})$) represents the probability, averaged over the entire image, that any two points in the medium separated by some distance r (known as the lag) in a given direction will both lie in a pore, as a function of r. If $r = 0$, then the two-point correlation function reduces to the one-point correlation function, which is equivalent to a constant; for the case of phase I it is the porosity of the rock (in other words, it represents the probability that any one point in the rock is in a pore). We have calculated two mutually perpendicular, two-point correlation functions (see section 2.10 for the methodology) in the A, B, and C directions of Figure 14, depending on the section orientation.

Permeability is but one of many petrophysical properties that may be derived from a knowledge of the two-point correlation function (Berryman and Blair, 1986; Berryman and Blair, 1987). In a lucid summary of the topic of spatial correlation functions, Blair et al. (1996) used the two-point correlation function and measured or estimated electrical formation factors (the ratio of pore-fluid conductivity to the effective conductivity of the porous medium saturated with that fluid) to calculate permeabilities for a suite of natural and synthetic sandstones. The results were within a factor of three of measured permeabilities. Blair et al. (1996) also reviewed sample preparation and image processing methods and demonstrated how quantitative microstructural parameters and qualitative information about the pore geometry can be derived graphically from a plot of the two-point correlation function.

Although care was taken to image only areas without extensive plucking, obvious plucked grains are present in some of the undeformed sediment and DBSZ sections. The

sites of plucked grains are filled with epoxy and appear as porosity in a BSE image, so it is important to consider what impact they may have on the structure of the two-point correlation functions. An image of undeformed sediment was processed to fill in the holes left by plucked grains and the two orthogonal two-point correlation functions were recalculated. The filled in $S_2(\mathbf{r})$ curves have ~1% lower porosity, as indicated by their values at $r = 0$. However, the shapes of the $S_2(\mathbf{r})$ curves for the original and filled in images are very similar and the relative correlation of the two orthogonal $S_2(\mathbf{r})$ curves at any given lag r is the same. So, at least for minor amounts of grain plucking, the effect is only to shift the $S_2(\mathbf{r})$ curves vertically, reflecting the effective porosity change caused by the plucked grains. With these results in mind, we have used only qualitative aspects of the $S_2(\mathbf{r})$ curves in our analysis, particularly the relative correlation at a given lag in two orthogonal directions within a particular image.

Anisotropy of Pore Geometry. The two-point correlation functions reveal a subtle, but systematic, anisotropy in the pore space geometry. Figure 15 is an example of mutually orthogonal, two-point correlation functions from a single BSE image from an A-oriented (foliation //, lineation //) petrographic section. The value at $r = 0$ corresponds to the porosity of the image, and as the lag r increases, the $S_2(\mathbf{r})$ curves decrease to approximately the square of porosity, indicating that at $r \geq 0.12$ mm, the pore structure is uncorrelated (cf. Blair et al., 1996). For $0 < r \leq 0.12$ mm, length scales which correspond to the size of single pores, the values of the $S_2(\mathbf{r})$ curves are determined by the spatially averaged cross-sectional shapes of single pores. As indicated in Figure 15d, the correlation in this lag range is higher in the down dip direction, indicating a subtle elongation of the pores in the down dip direction; i.e., for $0 < r \leq 0.12$ mm, two points

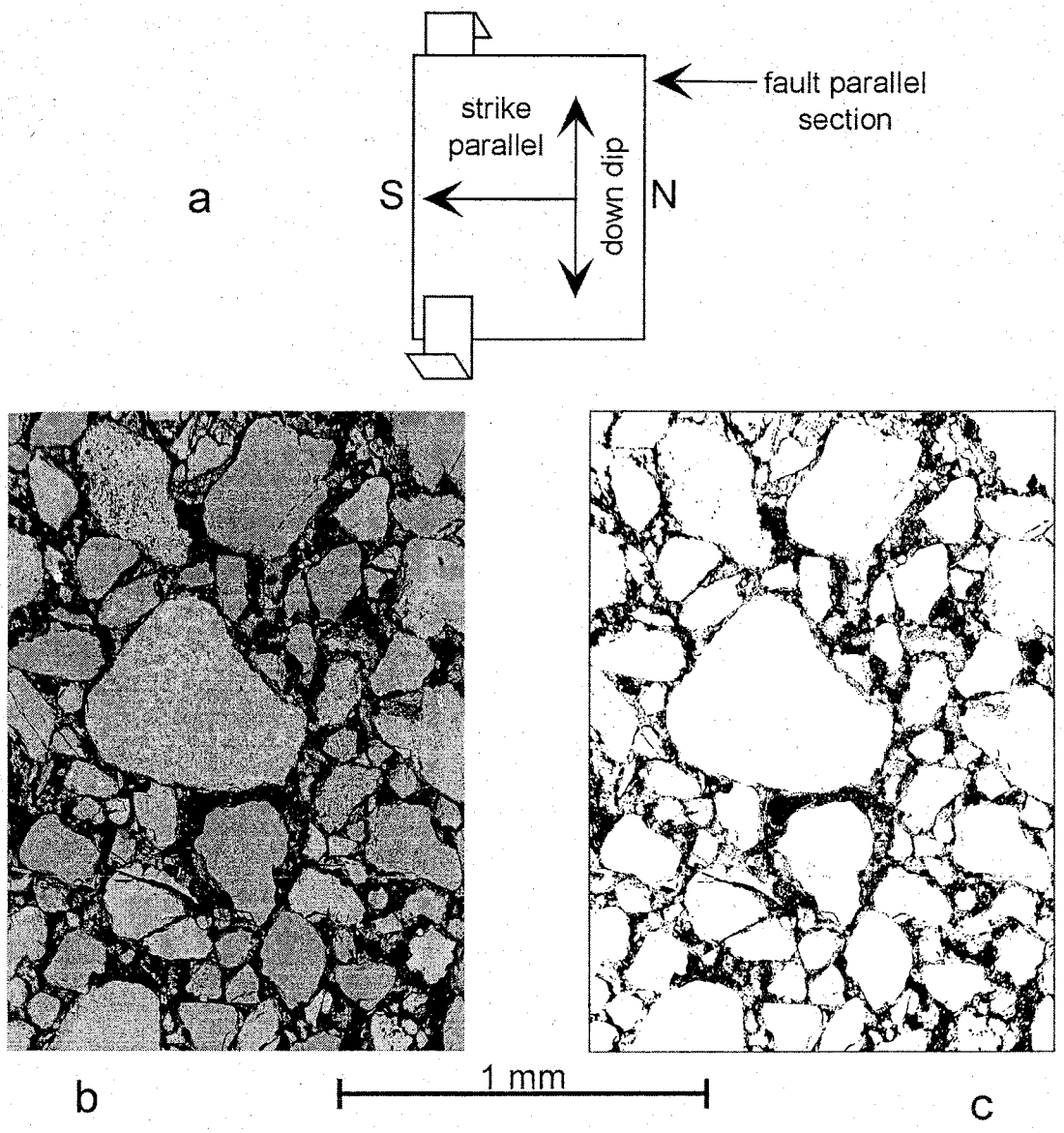
a
strike parallel
down dip
S
N
fault parallel section
b
1 mm
c
d
0.20
Φ
0.15
0.10
0.05
Φ²
0.00
S₂(r)
strike parallel
down dip
higher correlation in down dip direction
0.00
0.05
0.10
0.15
0.20
0.25
0.30
0.35
0.40
r (mm)

Figure 15. Example of calculation of two-point correlation functions for a section within the plane of the fault (following page). **a)** Orientations of two perpendicular directions (arrows) along which two-point correlation functions are calculated for the image. **b)** Greyscale BSE image. **c)** Processed binary image; pores are black. **d)** Orthogonal two-point correlation functions for the image in c. Higher correlations at small lags are indicated. Φ is the porosity of the image.

separated by a distance r in the down dip direction are more likely to both reside in a pore than two points separated by the same distance r in the strike parallel direction. Although the difference in spatial correlation is small, this is a robust result, as each datum within a given $S_2(\mathbf{r})$ curve is the result of spatial averaging of thousands of pairs of points over the entire image.

We observe this subtle directional difference of spatial correlation, or pore elongation, in almost all of the images examined, in sections of all orientations from samples of undeformed and deformed units. To emphasize these directional differences, in Figures 16 and 17 the $S_2(\mathbf{r})$ curves have been replotted as the difference between the two orthogonal $S_2(\mathbf{r})$ curves for a given image. Only lags less than $r = 0.2$ mm are plotted, to emphasize the short lags at which resolvable differences in directional spatial correlation are present.

We examined four to seven images from each section. Within any section of the deformed samples there is qualitative consistency of the results, even though the grain size in some sections varies considerably. Comparison of Figures 14 and 17 reveals that for the deformed samples, the direction closest to the orientation of the grain shape preferred orientation consistently has the higher spatial correlation of porosity. For example, the DBSZ sample has a grain SPO that is down dip when measured in the A orientation (foliation //, lineation //; Figure 14d). For the same thin section of this sample, in 4 of the 5 images examined, the pore geometry shows more correlation in the down dip direction than in the strike-parallel direction. This is indicated in Figure 17d by the solid $S_2(\mathbf{r})$ difference curves. $S_2(\mathbf{r})$ difference curves for all images in which this correspondence of grain SPO and pore geometry holds are shown as solid lines in Figures

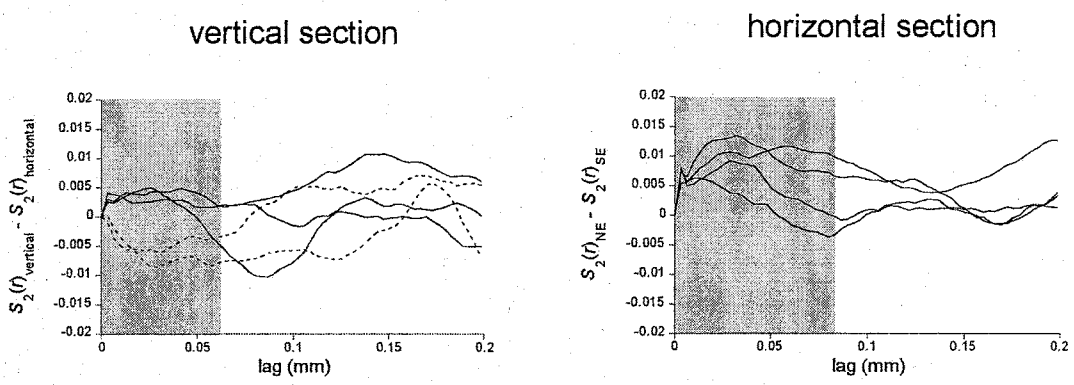

Figure 16. Two-point correlation function difference plots for images from two perpendicular sections of undeformed sand. Each curve is from a different image . $S_2(\mathbf{r})$ difference curves for images in which there is correspondence between grain SPO and pore elongation are shown as solid lines; where the is little or no correlation, the curve is dashed. The gray portions of the plots highlight the correlation differences at small lags.

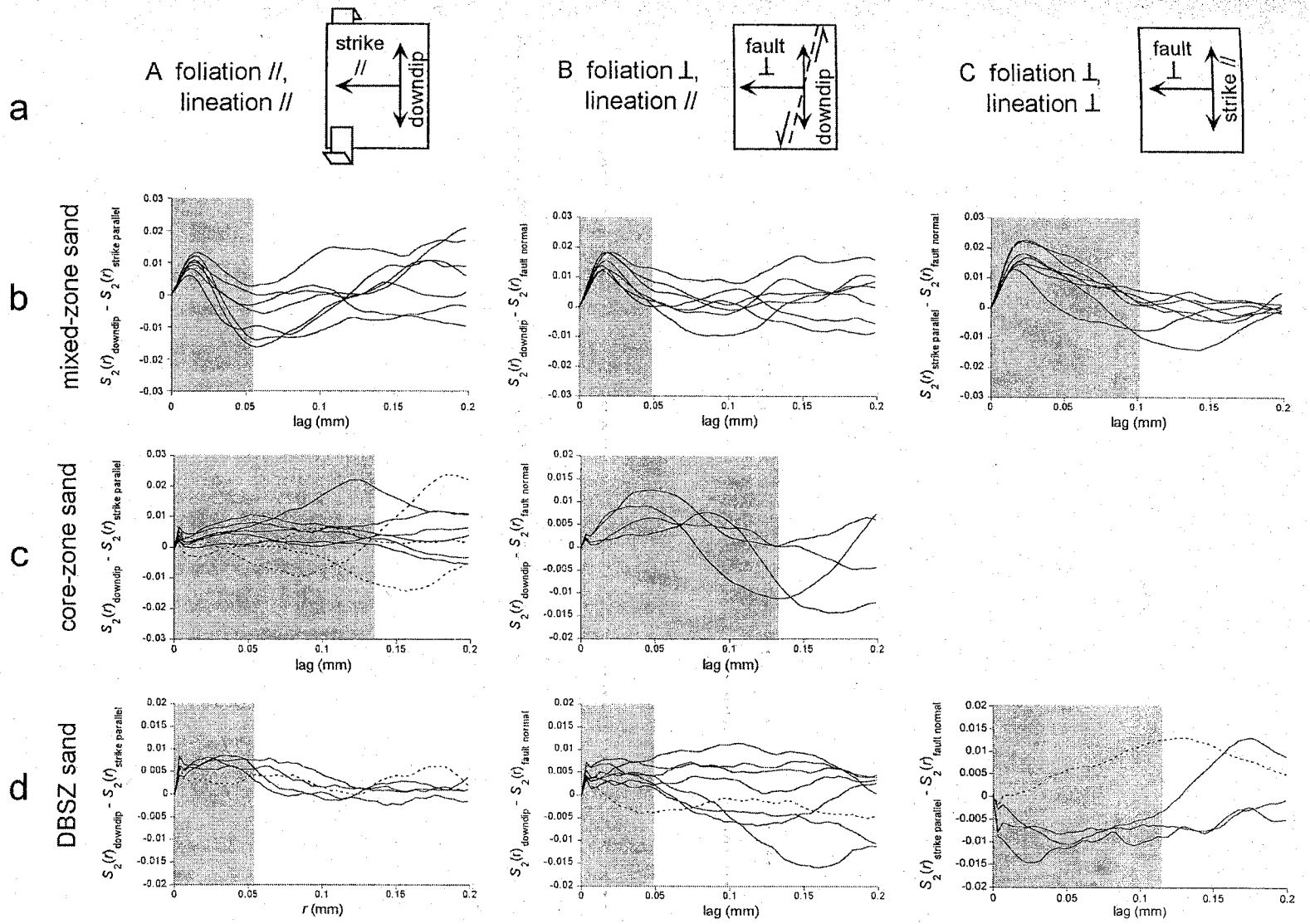
a
A foliation //, lineation //
strike //
downdip
B foliation ⊥, lineation //
fault ⊥
downdip
C foliation ⊥, lineation ⊥
fault ⊥
strike //
b
mixed-zone sand
c
core-zone sand
d
DBSZ sand
$S_2(r)_{downdip} - S_2(r)_{strike\ parallel}$
$S_2(r)_{downdip} - S_2(r)_{fault\ normal}$
$S_2(r)_{strike\ parallel} - S_2(r)_{fault\ normal}$
lag (mm)
r (mm)

Figure 17. Two-point correlation function difference plots for images from mutually perpendicular sections of deformed sand (following page). **a)** Orientations of two perpendicular directions along which two-point correlation functions were calculated for each image. Data from sections of a given orientation are arranged in columns. Two-point correlation function difference plots for: **b)** mixed-zone sand, **c)** core-zone sand, and **d)** DBSZ sand. Each curve is from a different image. $S_2(\mathbf{r})$ difference curves for images in which there is correspondence between grain SPO and pore elongation are shown as solid lines; where the is little or no correlation, the curve is dashed. The gray portions of the plots highlight the correlation differences at small lags.

16 and 17. The dashed lines are $S_2(\mathbf{r})$ difference curves from images in which this association of grain SPO and pore elongation is weak or nonexistent. The gray portions of the plots highlight the correlation differences at small lags. The correlation of grain SPO with pore-space anisotropy is not as strong for the vertically oriented section of the undeformed sediment sample (compare Figures 13 and 16), in which 2 of the 5 images examined show the opposite correlation.

2.7. Discussion

In this section we review and integrate the field and microstructural observations into a generalized, genetic sequence of fault-zone structures and deformation processes. We emphasize the development of mixed zones.

2.7.1. Incorporation of Sediment into the Fault Zone

Based on observations of normal faults at a variety of scales, Childs et al. (1996) proposed that much of the internal complexity of brittle fault zones may be explained by two processes: tip-line bifurcation and asperity bifurcation. The first process occurs when a propagating fault tip bifurcates into two or more, often subparallel, slip surfaces. Heterogeneity of the rock mass through which the tip line propagates will promote this bifurcation. This is easily envisioned in the case of a normal fault propagating through a layered sedimentary sequence. With continued slip, the tip-lines may rejoin, enclosing a body of rock within the fault as a lens or horse.

Asperity bifurcation occurs when wall rock irregularities are sheared off by local slip-surface bifurcation, and an intact block, often undeformed internally, is incorporated

into the fault zone (Watterson et al., 1998). Again, this process is easily envisioned as occurring in a normal fault propagating through a layered sedimentary sequence with some folding of beds by flexural-slip folding. The corners of beds projecting into the fault zone are removed by local slip-surface bifurcation. It is analogous to tip-line bifurcation but may occur throughout the deformation history of a given fault, not just during initial propagation.

In Figure 2, the subsidiary fault in the hanging wall bifurcates in several places within the relatively thickly bedded, clay-rich layers at the top of the outcrop. The splays range from vertical, to shallowly dipping, to bedding-parallel. The splays enclose essentially undeformed bodies of clay. Regardless of how this complex array of shears develops into a localized shear surface, continued movement on this series of splays will necessarily result in the incorporation of a significant amount of clay into the growing fault zone.

Evidence for asperity bifurcation is not available within the studied outcrops of the Sand Hill fault. However, we may reasonably infer its contribution as a fundamental fault-zone process. Watterson et al. (1998) argued that the contribution by asperity bifurcation to fault-rock thickness increases with increasing bed thickness and rotation. The widest portion of the Sand Hill fault includes the Waterfall site, which also has the widest mixed zone. Here the footwall stratigraphy is more sand-rich, more thickly bedded, and dips more steeply into the fault zone than at the Shooting Gallery site (Heynekamp et al., 1999). As the displacement is ~ 200m at both sites, these observations are consistent with at least some of the variation being due to asperity bifurcation at a

scale larger than the outcrop exposures, rather than being totally the result of tip-line bifurcation during the initial propagation of the fault.

Mixed-zone size is roughly correlated with fault slip, as mixed zones are absent in small displacement (<3m) faults (Sigda et al., 1999; Herrin, 2001), nascent to well developed in the Santa Ana fault, and extensively developed, although variable in width, in the Sand Hill fault. In addition, Heynekamp et al. (1999) observed some correlation between mixed zone composition and the composition of the immediately adjacent sediments. This would not be expected if the mixed zone was entirely formed during fault-tip propagation and/or by incorporation of sediment by asperity bifurcation. The above observations imply that sediment can potentially be added to the mixed zone throughout the life of the fault, but not necessarily continuously. Thus the mixed zone at any point in a large-displacement fault is composed of sediments that have been incorporated at different times in the fault movement history and that have been transported and deformed by varying amounts.

2.7.2. Ductile Deformation and Particulate Flow

Compositional Layering. Material incorporated into brittle fault zones in crystalline and lithified sedimentary rocks by the above processes often includes discrete, subangular blocks of variably deformed host rock surrounded by gouge (e.g., Childs et al., 1996; Foxford et al., 1998; Watterson et al., 1998). This pattern is not observed within the Sand Hill fault zone; indeed, many of the structures within the fault zones resemble structures from deep crustal shear zones. Pods of sand within the clay core and compositional layers within the mixed zones are elongate parallel to the fault and vary greatly in thickness. These thickness variations include smooth pinch and swell

morphologies, local attenuation of layers, and down dip thinning (Figures 8, 9, and 12). Compositional layers are generally thinner (<<1m) than bedding in the adjacent host sediment, and are commonly slightly inclined and/or asymptotic to the fault core, in a pattern similar to S-surfaces. Intermixing of disparate sediment types is common at layer boundaries. These patterns are also observed at the Santa Ana fault, which has much less displacement. Note the elongation and down dip narrowing of the tan medium-grained sand within the hanging wall mixed zone in Figure 2. These examples of ductile morphology would not be expected if the incorporated bedding were merely a rotated block of sediment incorporated into the fault, but are consistent with the incorporated sediment having been pervasively deformed.

Mesoscopic Structures. In addition to the geometry of compositional layering, mesoscopic structures are also indicative of penetrative ductile deformation. Figure 10, from the upper Shooting Gallery outcrop, illustrates an S-C fabric defined by intermixed medium-grained sand and clay. Also present are steeply dipping compositional layers 1-2 cm thick, defined by slight color and surface-textural differences related largely to clay content. An elongate pod of coarse sand with relict, slightly dipping bedding, is surrounded by homogenous sand with a subtle, steeply dipping foliation.

Figure 8 shows a complex array of deformation bands within tan medium-grained sand in the footwall mixed zone at the Shooting Gallery site. Bedding laminae are only locally preserved in the sand and are steeply dipping and subparallel to the clay-rich layers just above. Although the network of deformation bands is impressive, the total deformation accommodated by the network is small, as the offset along any one band is no more than 2-3 cm. Almost all of the bands terminate at the mixed zone – damage zone

boundary and at the contact with the red-tan, clay-rich medium sand, which shows no discrete deformation structures, yet is similarly rotated. The bulk strain represented by the network is down dip extension parallel to the fault, not rotation. The ~ 60° rotation required to place transposed bedding in its current steeply dipping orientation must have been accommodated by penetrative deformation that resulted in destruction of most of the bedding laminae.

Microscopic Fabric - Grain Shape Preferred Orientations. Grain SPOs also preserve evidence for penetrative ductile deformation. In vertical, fault-perpendicular (B) sections from all three architectural elements, the SPO dips 40° to 55° from horizontal (Figure 14, middle column). Even given reasonable uncertainty in section orientation (5-10°), this is a shallower dip than either the compositional layering in the mixed zone or the fault zone as a whole (see Figure 14), indicating that the SPO is inclined to potential shear zone boundaries. The angle of inclination (<30°) is similar to that reported by Cladouhos (1999) for survivor grains in clay-rich fault gouge, and is similar in orientation to P-foliations (Figure 5f) and S-surfaces.

That the SPO is a record of penetrative deformation via particulate flow is suggested by the fact that in the B sections it faithfully records the east-side down, normal fault kinematics in all of the fault samples, and perhaps records the varying degrees of localization and/or total deformation as well. Although statistically not significant, the SPO in the DBSZ dips more steeply (hence, forms a smaller angle with the fault) than that of the mixed zone sample. This is consistent with greater deformation localization within the DBSZ. Furthermore, if we assume that the undeformed grain SPO of Figure 13 is representative, we may consider the effect of rigid-body rotation of a bed

of undeformed footwall sand into parallelism with the fault zone. If the compositional layering in the mixed zone (Figure 8) were formed solely by rigid-body rotation of bedding, then the inclination of the grain SPO in a B section from the fault should match the dip of compositional layering. This is not the case for any of the fault zone samples.

The consistency of the grain SPOs in the B sections suggests that, in this plane, the SPO from all three architectural elements reflects the bulk kinematics of the fault zone (Figure 14, middle column). However, there are differences in SPOs evident in the other sections. The SPO in the fault-parallel (A) section from the DBSZ is down dip (Figure 14d, left column), similar to sand lineations visible on foliation planes in outcrop. The SPO in the horizontal, fault-perpendicular (C) section, however, is perpendicular to the fault (Figure 14d, right column) – an unusual orientation that we believe has not been described elsewhere. Nevertheless, taken together, the three mutually orthogonal SPO measurements from the DBSZ define a fabric with monoclinic symmetry that records the bulk kinematics of the fault zone.

In contrast, the grain SPO in the fault-parallel (A) section from the mixed zone is neither down dip nor strike-parallel (Figure 14b, left column). The grain SPO in the horizontal, fault-perpendicular (C) section from the mixed zone is parallel to the fault (Figure 14b, right column). Thus, the three mutually orthogonal SPO measurements from the mixed zone do not correlate with the kinematics of the fault zone (i.e., they do not record pure dip-slip motion), but instead apparently record oblique slip. The grain SPO in the fault-parallel (A) section from the core zone sand is also moderately inclined, but it is poorly developed (Figure 14c, left column). There are several possible explanations for these deviations from the simple kinematic picture recorded by the grain SPO within the

DBSZ: (1) the DBSZ either experienced greater deformation localization or represents a different portion of the fault zone deformation history (see section 2.6.4); (2) the mixed and core zone SPOs may record local variations in deformation intensity caused by irregular shear zone boundaries or sediment heterogeneity, which could result in, for example, development of oblique-slip or fault-parallel extension; (3) The kinematic regime within the mixed and core zones is not just simple shear but general shear, in which lineations need not record the transport direction in the shear zone (e.g., Jiang and Williams, 1998; Lin et al., 1998).

Microscopic Fabric - Anisotropy of Pore Geometry. In general, the anisotropy of pore geometry reflects the grain SPO. In the undeformed samples, the $S_2(r)$ difference curves show that the pores are elongate parallel to the grain SPO in the horizontal plane (Figure 16). However, in the vertical plane (Figure 16), the correlation of pore elongation with grain SPO is ambiguous. This may reflect that, on average, the pores are equant in the vertical plane.

In A and B sections, all fault zone samples show an elongation of pores down dip in the plane of the fault (Figure 17). The weak development of this elongation in the A section of the core zone sand (Figure 17c) is consistent with the weak development of grain SPO in this section (Figure 14c). This again suggests that the anisotropy of pore geometry is largely determined by the reorganization of grains and development of grain SPO. In the C sections, the anisotropy of pore geometry in the mixed zone is orthogonal to that in the DBSZ, a relationship that is also exhibited by the grain SPOs. Viewed in this orientation, pores are elongate parallel to fault strike in the mixed zone sample and elongate normal to the fault in the DBSZ sample. Together, the grain SPOs and the

anisotropy of pore geometry provide complementary evidence to suggest that the mixed zone sediments have undergone penetrative deformation, which was accomplished by particulate flow and cataclasis. We do not currently understand the significance of the fault perpendicular grain and pore elongation evident in the C section of the DBSZ. Interestingly, it is perpendicular to the foliation visible in outcrop.

2.7.3. Deformation Bands

Consistent overprinting relationships between individual deformation bands and other fault-zone structures indicate that they represent a later, more localized style of deformation. Individual deformation bands typically terminate at compositional layer boundaries (Figures 2, 3, and 8), and are poorly developed to absent in clay-rich sands (Figures 2, 8, 9). As they are present in deformed mixed-zone sands that show evidence of penetrative particulate flow (Figure 8), they must have formed after this penetrative deformation occurred, as such deformation would distort their planar geometry or erase them completely (Miller, 1996).

Even complex networks of deformation bands accommodated little bulk strain (Figure 8). This strain is not sufficient to account for the extensive bed rotation commonly observed within the mixed zones. The strain accommodated by the deformation bands is largely plane strain related to dip-slip movement along the fault. This can be seen from the compiled orientation data from the damage and mixed zones (Figure 5) – the majority of the deformation bands are steeply dipping and strike subparallel to the main fault. This contrasts with the more complex and heterogeneous strain field recorded by grain SPOs and the anisotropy of pore geometry (Figures 14 and 17).

The contacts between sandy mixed zones and damage zones are commonly DBSZs, as are some internal contacts within mixed zones (Figures 2, 4, and 9). DBSZs within mixed zones may be offset by individual deformation bands (Figure 3). However, DBSZs forming mixed zone – damage zone contacts appear to have formed contemporaneously and/or after the mixed zones, as they truncate or are parallel to deformation structures and transposed bedding in the mixed zones, and truncate bedding in the damage zones.

2.7.4. Fault-zone Structural Development

The observations reported here suggest that most of the sediment incorporated into the fault zone by asperity or tip-line bifurcation does not remain as distinct blocks, but is transposed into fault-parallel compositional layering by penetrative particulate flow. This particulate flow is accompanied and/or facilitated by cataclasis in sandy sediments and, presumably, by penetrative shear in clay-rich sediments that results in foliation development in the transposed bedding (Figures 8 and 9). The individual sedimentary layers may undergo considerable internal deformation and extension, as indicated by thinning and development of an internal foliation and lineation, yet remain coherent, and so their origin as sedimentary layers remains identifiable.

Damage Zones and Deformation Bands. The macroscopically ductile structures in the mixed zones are overprinted by deformation bands, which are the result of localized cataclastic deformation. Evidence for cataclasis has been observed in individual deformation bands and small-displacement normal faults composed of deformation bands within the Santa Fe Group (Sigda et al., 1999; Herrin, 2001), within poorly lithified sediments in accretionary wedges (Lucas and Moore, 1986), and within unlithified

Pleistocene beach sands associated with an active thrust fault (Cashman and Cashman, 2000). In the Sand Hill fault zone, cataclastic deformation in DBSZs is much more intense than within adjacent mixed-zone sands. If the DBSZs formed contemporaneously with mixed-zone structures, the more intense cataclasis indicates that they are zones of more intense deformation. The differences between DBSZs and the bulk of the mixed zones would therefore be due to higher strain within the DBSZ. Conversely, if they formed after the mixed-zone structures, the more intense cataclasis may reflect a transition in deformation mechanisms from distributed particulate flow with subordinate cataclasis to highly localized deformation in which cataclasis plays a greater role.

In the exposures examined in this study, extensive networks of deformation bands are only present within the mixed zone (Figures 2 and 8). Arrays of deformation bands in the damage zones are much simpler or nonexistent in both large-displacement (Figure 9) and small-displacement (Figure 2) faults. The subsidiary fault in the hanging wall of the Santa Ana fault is highly localized as a DBSZ in sand and bifurcates where it enters the clay layer. As analogs to the early stages of the large-displacement Sand Hill fault, this subsidiary fault and the adjacent Santa Ana fault imply that fault-zone evolution, even in sandy layers, does not require extensive damage-zone development before a through-going slip surface or clay core is formed. The overprinting of deformation bands on foliations and compositional layering do, however, argue for the relatively early development of mixed zones.

Our observations suggest that deformation in damage zones may represent local accommodation of movement at fault-zone irregularities, perhaps releasing or extensional bends. However, in a study of deformation band formation in Santa Fe Group sediments,

Herrin (2001) observed a 50+ meter-wide zone of small-displacement DBSZs with no development of mixed zones or extensive localization of slip. Due to erosion, maximum displacement on the DBSZs could not be determined, but was estimated to be 6.4 meters. It is not known whether this wide zone of DBSZs represents a damage zone formed prior to a large-displacement fault with mixed zones. Heynekamp et al. (1999) proposed that damage zones formed early in the evolution of the Sand Hill fault zone and continued to widen and increase in complexity until a thoroughgoing clay core developed, facilitating localization of deformation. Our data do not support this model. It is apparent that further study is needed to determine the ultimate controls on damage-zone development and evolution in poorly-lithified sediments.

Mixed Zones and Penetrative Deformation. Penetrative ductile deformation and mixing within clay-rich gouge and cataclasite have been documented previously in brittle faults in hard rocks (e.g., Miller, 1996; Chester and Chester, 1998; Cladouhos, 1999). However, in these studies, the fault rocks were derived via brittle deformation and alteration by water-rock interaction of originally crystalline and well lithified sedimentary rocks. All of the documented faults have undergone very large total displacement. In contrast, due to the poorly lithified and inherently weak nature of the Santa Fe group sediments, initial deformation was accomplished largely by sediment disaggregation and penetrative flow at the grain scale, even at relatively low total displacement (e.g., the Santa Ana fault).

Mechanical Considerations. The majority of the observations from the Sand Hill fault are from the well-exposed footwall. Because it is a growth fault, the footwall sediment will record more of the structural history of the fault as it was progressively

uplifted, excepting intervals in which erosion removed the stratigraphic and structural record. With reasonable inferences about the stress history of the footwall materials, the behavior of unlithified sediments can be compared to predictions from critical-state soil mechanics theory (cf., Jones and Addis, 1986; Karig, 1986).

Normally consolidated sediments have never experienced greater stresses than those at their ambient conditions, and are to be expected in subsiding sedimentary basins (Jones and Addis, 1984; Jones and Addis, 1986). The deformation behavior of normally consolidated sediments is characterized by distributed deformation that is penetrative at the grain scale and bulk strain hardening throughout the deforming mass (Atkinson and Bransby, 1978; Scott, 1980). This can result in a progressive thickening of the deforming zone (Moore and Byrne, 1987). We infer the style of deformation evident in the mixed zones to represent distributed deformation of normally consolidated sediments.

With progressive footwall uplift and unloading due to fault motion and erosion, the ambient stress decreases below the maximum stresses to which the sediments and fault rocks have been subjected. The footwall sediments and footwall damage and mixed zones will therefore be in an overconsolidated state for this portion of the fault history (Atkinson and Bransby, 1978; Scott, 1980). Deformation of overconsolidated sandy and clay-rich sediments is characterized by the attainment of a peak strength followed by strain-softening (Bishop, 1975; Skempton, 1985). This has also been observed during the experimental formation of deformation bands in Berea sandstone (Menéndez et al., 1996). This results in spatial localization of deformation and the formation of discrete shear zones (Ellen and Fleming, 1987; Moore and Byrne, 1987), which in our case are deformation bands. Thus a time sequence of distributed deformation by grain-scale flow

in normally consolidated sediments followed by the formation of localized deformation bands is consistent with the observed overprinting relationships in the Santa Ana and Sand Hill fault zones.

2.8. Implications

Our observations indicate that mixed zones may initiate early in the deformation history of a given fault zone. In a region undergoing extensive sedimentation and subsidence, growth faults may form and remain active as they are progressively buried. With burial, compaction, and lithification, early–formed mixed zones may be preserved and/or overprinted with macroscopically brittle structures. Post-lithification deformation likely would be more localized, as in the form of discrete fractures, fracture networks, and relatively narrow cataclastic shear zones. It is therefore probable that prelithification structures such as mixed zones can be preserved through protracted post-lithification deformation, and may in fact form the host rock to these later structures. This has implications for correlating and interpreting the deformational, burial, diagenetic, and fluid-flow histories of faults and their host rocks (cf. Hippler ,1993; Byrne, 1994).

An example of these implications is provided by the study of Berg and Avery (1995). They identified faults as sheared zones in cores from 3900 to 4500m depth within the lower Eocene of the Texas Gulf coast. They described several types of macroscopically ductile structures and fabrics: intimately intermixed sand, silt and shale, and several types of compositional foliations, which are commonly folded and crosscut each other. They observed a rough sequence of structures which they inferred represented an increase in deformation intensity, but these were randomly located in space relative to

the main plane of the fault. The ductile structures were locally overprinted by discrete normal faults with millimeters of displacement, suggestive of post-lithification deformation. Berg and Avery (1995) argued that the majority of the structures and fabrics formed by ductile flow of poorly lithified sediment (shale), but with additional incorporation of sediments from the hanging wall and footwall.

Many of the ductile fabrics and structural features described by Berg and Avery (1995) are similar in appearance to small-scale structures seen in the Sand Hill and Santa Ana faults. The cores were recovered from depths three to four times the maximum burial depth of Sand Hill fault outcrops examined in this study, and in photos they appeared to be well lithified. Thus, it is possible that the sheared zones of Berg and Avery (1995) are in part relict mixed zones, overprinted with more brittle deformation that occurred after lithification (e.g., the discrete small-displacement faults). The ranges of permeability measured by Berg and Avery (1995) on cores of the sheared zones (0.1 md to <0.01 md) are towards the low end of the ranges of mixed-zone permeabilities (Chapter 4). This is consistent with the sheared zones being mixed zones analogous to those within the Sand Hill fault zone, with the reduced permeability being due to diagenesis or compaction related to burial. The presence of these sheared zones strongly controlled the sealing ability of the faults and whether are not they acted as traps for hydrocarbons (Berg and Avery, 1995). Although the more clay-rich sheared zones acted as better seals, in general, homogenization of different sediment types in the sheared zones resulted in a fault rock with significant potential to trap hydrocarbons.

2.9. Conclusions

We have used field and microstructural observations from normal faults cutting poorly lithified sediments of the Santa Fe Group of the Rio Grande rift, New Mexico USA, to document the development of mixed zones. Initiation of mixed zones can occur very early during fault-zone evolution and need not be preceded or accompanied by extensive damage-zone development. The initial incorporation of sediment into a given fault zone is inferred to occur by tip-line and asperity bifurcation, and additional sediment may be incorporated throughout the movement history of the fault. Initial deformation within the mixed and core zones in the Sand Hill fault zone was accomplished by penetrative particulate flow with subordinate cataclasis, evidence of which is preserved at both the macro- and microscale even within transposed sedimentary bedding within mixed zones. Progressive deformation within mixed zones resulted in transposition of bedding into compositional foliations and the development of local, macroscopically ductile, high-strain zones, which may have been accompanied by more intense cataclasis. Ultimately, a mode of failure transition occurred and ductile structures were overprinted by deformation bands, which are a product of localized cataclastic deformation. The observed overprinting relationships are consistent with the inferred stress and consolidation history of the fault zones and their host sediments. Mixed zones may be preserved and overprinted by post-lithification deformation, characterized by discrete fractures. This study and others (e.g., Berg and Avery, 1995; Chapters 4 and 5) suggest that mixed zones significantly affect subsurface fluid flow and the sealing and trapping capacity of faults in petroleum reservoirs.

2.10. Appendix – Calculation of Two-point Correlation Functions

We calculated two-point correlation functions on 1024x768 pixel back-scattered electron (BSE) images of undeformed, DBSZ, and core-zone sand samples. Porosity is black in these images and minerals are varying shades of gray, allowing easy discrimination of pores. We used 640x480 pixel optical images from a petrographic microscope to calculate two-point correlation functions of mixed zone samples. The mixed zone samples were impregnated with blue-dyed epoxy which allowed the pores to be discriminated from mineral grains in optical images. This discrimination was performed using macro code in Scion Image image analysis software. The discrimination algorithm was based on that of Crabtree et al. (1984).

The images were processed so that pixels in pores had values of 1 and pixels in minerals had values of 0. In this form, the image is a graphical representation of a discrete indicator function for porosity, or one-point correlation function, S_1, which takes a value of 1 in a pore and a value of zero elsewhere. The average value of the indicator function over the whole image is the porosity of the image:

$$S_1 = \langle f(\mathbf{x}) \rangle = \Phi \quad . \tag{2A.1}$$

The two-point correlation function,

$$S_2(\mathbf{r}) = \langle f(\mathbf{x}) f(\mathbf{x}+\mathbf{r}) \rangle \, , \tag{2A.2}$$

is the average value of the product of the indicator functions for all pixel pairs separated by a lag r in a given direction, as a function of r (Blair et al., 1996). In this study, for each image, each datum in a correlation function represents the product of the indicator functions of at least 200,000 pixel pairs. The value of the indicator function for each pixel

and its coordinates were exported to a text file. We calculated the two-point correlation functions using a modified version of the FORTRAN program gam from the GSLIB geostatistical software library (Deutsch and Journel, 1998). The BSE images have a higher resolution then the optical images, and the resulting $S_2(\mathbf{r})$ curves are noisier than those of the optical images.

2.11. Acknowledgements

This work was supported by the National Science Foundation (grants EAR-9706482 and EAR 9526983), the New Mexico Geological Society, and the New Mexico Department of Safety. We are especially grateful to Stephen Blair for suggesting the use of two-point correlation functions to characterize pore-space geometry. We thank Sean Connell for discussions on Albuquerque Basin geology, Nelia Dunbar and Lynn Heizler for assistance with the microprobe, and John Wilson and John Sigda for discussions on spatial correlation.

2.12. References Cited

Antonellini, M. A. and Aydin, A., 1994, Effect of faulting on fluid flow in porous sandstones: petrophysical properties: American Association of Petroleum Geologists Bulletin, v. 78, p. 355-377.

Antonellini, M. A. and Aydin, A., 1995, Effect of faulting on fluid flow in porous sandstones: geometry and spatial distribution: American Association of Petroleum Geologists Bulletin, v. 79, p. 642-671.

Antonellini, M. A., Aydin, A. and Pollard, D. A., 1994, Microstructure of deformation bands in porous sandstones at Arches National Park, Utah: Journal of Structural Geology, v. 16, p. 941-959.

Atkinson, J. H., and Bransby, P. L., 1978, The mechanics of soils: an introduction to critical state soil mechanics: New York, McGraw-Hill, 375 p.

Aydin, A., 1978, Small faults formed as deformation bands in sandstones: Pure and Applied Geophysics, v. 116, p. 913-930.

Beckner, J., 1996, Cementation processes and sand petrography of the Zia Formation, Albuquerque Basin, New Mexico. M.S. Thesis, New Mexico Institute of Mining and Technology, 146 p.

Benn, D. I., and Evans, D. J. A., 1996, The interpretation and classification of subglacially deformed materials: Quaternary Science Reviews, v. 15, p. 23-52.

Berg, R. R., and Avery, A. H., 1995, Sealing properties of Tertiary growth faults, Texas gulf coast: American Association of Petroleum Geologists Bulletin, v. 70, p. 375-393.

Berryman, J. G., 1985, Measurement of spatial correlation functions using image processing techniques: Journal of Applied Physics, v. 57, p. 2374-2384.

Berryman, J. G., and Blair, S. C., 1986, Use of digital image analysis to estimate fluid permeability of porous materials: Application of two-point correlation functions: Journal of Applied Physics, v. 60, p. 1930-1938.

Berryman, J. G., and Blair, S. C., 1987, Kozeny-Carman relations and image processing methods for estimating Darcy's constant: Journal of Applied Physics, v. 62, p. 2221-2228.

Bishop, A. W., 1975, The strength of soils as engineering materials, *in* Milestones in soil mechanics; the first ten Rankine lectures: UK, Thomas Telford Ltd., p. 91-128.

Blair, S. C., Berge, P. A., and Berryman, J. G., 1996, Using two-point correlation functions to characterize microgeometry and estimate permeabilities of sandstones and porous glass: Journal of Geophysical Research, v. 101, p. 20359-20375.

Bredehoeft, J. D., Belitz, K. and Sharp-Hansen, S., 1992, The hydrodynamics of the Bighorn Basin: A study of the role of faults: American Association of Petroleum Geologists Bulletin, v. 76, p. 530-546.

Byrne, T., 1994, Sediment deformation, dewatering and diagenesis: illustrations from selected melange zones, *in* Maltman, A., ed., The geological deformation of sediments, London, Chapman and Hall, p. 239-260.

Caine, J. S., Evans, J. P. and Forster, C. B., 1996, Fault zone architecture and permeability structure: Geology, v. 24, p. 1025-1028.

Caine, J. S. and Forster, C. B., 1999, Fault zone architecture and fluid flow: insights from field data and numerical modeling, *in* Haneberg, W. C., Mozley, P. S., Moore, K. C., and Goodwin, L. B., eds., Faults and subsurface fluid flow in the shallow crust: Washington, DC, American Geophysical Union, p. 101-127.

Cashman, S., and Cashman, K., 2000, Cataclasis and deformation-band formation in unconsolidated marine-terrace sand, Humboldt County, California: Geology, v. 28, p. 111-114.

Chester, F. M. and Chester, J. S., 1998, Ultracataclasite structure and friction processes of the Punchbowl fault, San Andreas system, California: Tectonophysics, v. 295, p. 199-221.

Chester, F. M., Evans, J. P. and Biegel, R. L., 1993, Internal structure and weakening mechanisms of the San Andreas fault: Journal of Geophysical Research, v. 98, p. 771-786.

Chester, F. M., and Logan, J. M., 1986, Implications for mechanical properties of brittle faults from observations of the Punchbowl fault zone, California: Pure and Applied Geophysics, v. 124, p. 79-106.

Childs, C., Watterson, J., and Walsh, J. J., 1996, A model for the structure and development of fault zones: Journal of the Geological Society, v. 153, p. 337-340.

Cladouhos, T. T., 1999, Shape preferred orientations of survivor grains in fault gouge: Journal of Structural Geology, v. 21, p. 419-436.

Connell, S. D., Koning, D. J., and Cather, S. M., 1999, Revisions to the stratigraphic nomenclature of the Santa Fe Group, northwestern Albuquerque Basin, New Mexico, *in* Pazzaglia, F. J., and Lucas, S. G., eds., Albuquerque Geology: New Mexico Geological Society, 50th Annual Field conference, Guidebook, p. 337-353.

Crabtree, S. J., Ehrlich, R., and Prince, C., 1984, Evaluation of strategies for segmentation of blue-dyed pores in thin sections of reservoir rocks: Computer Vision, Graphics, and Image Processing, v. 28, p. 1-18.

Deutsch, C. V., and Journel, A. G., 1998, GSLIB: geostatistical software library and user's guide: New York, Oxford University Press, 369 p.

Ellen, S. D., and Fleming, R. W., 1987, Mobilization of debris flows from soil slips, San Francisco Bay region, California, *in* Costa, J. E., and Wieczorek, G. F., eds., Debris flows/avalanches: process, recognition, and mitigation: Geological Society of America, Reviews in engineering geology, v. 7, p. 31-40.

Evans, J. P., Forster, C. B. and Goddard, J. V., 1997, Permeability of fault related rocks, and implications for hydraulic structure of fault zones: Journal of Structural Geology v. 19, p. 1393-1404.

Forster, C. & Evans, J. 1991, Hydrogeology of thrust faults and crystalline thrust sheets: results of combined field and modeling studies: Geophysical Research Letters, v. 18, p. 979-982.

Foxford, K. A., Walsh, J. J., Watterson, J., Garden, I. R., Guscott, S. C. and Burley, S. D., 1998, Structure and content of the Moab Fault Zone, Utah, USA, and its implications for fault seal prediction, *in* Jones, G., Fisher, Q. J. and Knipe, R. J., eds., Faulting, fault sealing, and fluid flow in hydrocarbon reservoirs: London, The Geological Society, p. 87-103.

Goodwin, L. B., Mozley, P. S., Moore, J. C. and Haneberg, W. C., 1999, Introduction, *in* Haneberg, W. C., Mozley, P. S., Moore, K. C., and Goodwin, L. B., eds., Faults and subsurface fluid flow in the shallow crust: Washington, DC, American Geophysical Union, p. 1-5.

Haneberg, W. C., 1995, Steady-state groundwater flow across idealized faults: Water Resources Research, v. 31, p. 1815-1820.

Hawley, J.W., 1996, Hydrogeologic framework of potential recharge areas in the Albuquerque basin, central New Mexico: New Mexico Bureau of Mines and Mineral Resources Open-File Report 402 D, Chapter 1.

Hawley, J. W., Haase, C. S. and Lozinsky, R. P., 1995, An underground view of the Albuquerque Basin, *in*, The Water Future of Albuquerque and the Middle Rio Grande Basin, Proceedings of the 39th Annual New Mexico Water Conference, New Mexico Water Resources Research Institute Report 290, p. 37-55.

Herrin, M., 2001, Characteristics of deformation bands in poorly lithified sand, Rio Grande rift, New Mexico [M.S. thesis]: New Mexico Institute of Mining and Technology, 81 p.

Heynekamp, M. R., Goodwin, L. B., Mozley, P. S., and Haneberg, W. C., 1999, Controls on fault-zone architecture in poorly lithified sediments, Rio Grande Rift, New Mexico: Implications for fault-zone permeability and fluid flow, *in* Haneberg, W. C., Mozley, P. S., Moore, K. C., and Goodwin, L. B., eds., Faults and subsurface fluid flow in the shallow crust: Washington, DC, American Geophysical Union, p. 27-50.

Hippler, S. J., 1993, Deformation microstructures and diagenesis in sandstone adjacent to an extensional fault: implications for the flow and entrapment of hydrocarbons: American Association of Petroleum Geologists Bulletin, v. 77, p. 625-637.

Jiang, D. and Williams, P. F., 1998, High-strain zones: a unified model: Journal of Structural Geology, v. 20, p. 1105-1120.

Jones, M. E., and Addis, M. A., 1984, Volume change during sediment diagenesis and the development of growth faults: Marine and Petroleum Geology, v. 1, p. 118-122.

Jones, M. E., and Addis, M. A., 1986, The application of stress path and critical state analysis to sediment deformation: Journal of Structural Geology, v. 8, p. 575-580.

Karig, D. E., 1986, Physical properties and mechanical state of accreted sediments in the Nankai Trough, S.W. Japan, *in* Moore, J. C., ed., Structural fabrics in Deep Sea Drilling Project cores form forearcs: Memoir 166, Boulder, CO, The Geological Society of America, p. 117-133.

Knipe, R. J., 1993, The influence of fault zone processes and diagenesis on fluid flow, *in* Horbury, A. D. and Robinson, A. G., eds., Diagenesis and basin development: Tulsa, OK, American Association of Petroleum Geologists, p. 135-151.

Lin, S., Jiang, D., and William, P. F., 1998, Transpression (or transtension) zones of triclinic symmetry: natural example and theoretical modeling, *in* Holdsworth, R. E., Strachan, R. A., and Dewey, J. F., eds., Continental transpressional and transtensional tectonics: London, Geological Society, p. 41-57.

Lister, G. S., and Snoke, A. W., 1984, S-C mylonites: Journal of Structural Geology, v. 6, p. 617-638.

Logan, J. M., Dengo, C. A., Higgs, N. G., and Wang, Z. Z., 1992, Fabrics of experimental fault zones: their development and relationship to mechanical behavior, *in* Evans, B., and Wong, T.-f., eds., Fault mechanics and transport properties of rocks: London, Academic Press, p. 33-68.

Lucas, S. E., and Moore, J. C., 1986, Cataclastic deformation in accretionary wedges: Deep Sea Drilling Project Leg 166, southern Mexico, and on-land examples from Barbados and Kodiak Islands, *in* Moore, J. C., ed., Structural fabrics in Deep Sea

Drilling Project cores from forearcs, Memoir 166: Boulder, CO, The Geological Society of America, p. 89-104.

Menéndez, B., Zhu, W., and Wong, T.-f., 1996, Micromechanics of brittle faulting and cataclastic flow in Berea sandstone: Journal of Structural Geology, v. 18, p. 1-16.

Miller, M. G., 1996, Ductility in fault gouge from a normal fault system, Death Valley, California: a mechanism for fault zone strengthening and relevance to paleoseismicity: Geology, v. 24, p. 603-606.

Moore, J. C., and Byrne, T., 1987, Thickening of fault zones: a mechanism of melange formation in accreting sediments: Geology, v. 15, p. 1040-1043.

Mozley, P. S., and Goodwin, L. B., 1995, Patterns of cementation along a Cenozoic normal fault: A record of paleoflow orientations: Geology, v. 23, p. 539-542.

Pazzaglia, F. J., Connell, S. D., Hawley, J., Tedford, R. H., Personius, S., Smith, G. A., Cather, S., Lucas, S., Hester, P., Gilmore, J., and Woodward, L., 1999, Second-day trip 2 road log, from Albuquerque to San Ysidro, Loma Creston, La Ceja, and Sand Hill fault, *in* Pazzaglia, F. J., and Lucas, S. G., eds., Albuquerque Geology: New Mexico Geological Society, 50th Annual Field conference, Guidebook, p. 47-66.

Rutter, E. H., 1986, On the nomenclature of mode of failure transitions in rocks: Tectonophysics, v. 122, p. 381-387.

Rutter, E. H., Maddock, R. H., Hall, S. H., and White, S. H., 1986, Comparative microstructures of natural and experimentally produced clay bearing fault gouges: Pure and Applied Geophysics, v. 124, p. 3-29.

Scott, C. R., 1980, An introduction to soil mechanics and foundations: London, Applied Science Publishers, 406 p.

Shelley, D., 1995, Asymmetric shape preferred orientations as shear-sense indicators: Journal of Structural Geology, v. 17, p. 509-517.

Sigda, J. M., Goodwin, L. B., Mozley, P. S., and Wilson, J. L., 1999, Permeability alteration in small-displacement faults in poorly lithified sediments: Rio Grande Rift, Central New Mexico, *in* Haneberg, W. C., Mozley, P. S., Moore, K. C., and Goodwin, L. B., eds., Faults and subsurface fluid flow in the shallow crust: Washington, DC, American Geophysical Union, p. 51-68.

Skempton, A. W., 1985, Residual strength of clays in landslides, folded strata, and in the laboratory: Geotechnique, v. 35, p. 3-18

Smith, L., Forster, C., and Evans, J., 1990, Interaction of fault zones, fluid flow, and heat transfer at the basin scale, *in* Neuman, S. P., and Neretnieks, I., eds., Hydrogeology of low permeability environments, Hanover, Verlag Heinz Heisse, p. 41-67.

Starkey, J., 1977, The contouring of orientation data represented in spherical projection: Canadian Journal of Earth Sciences, v. 14, p. 268-277.

Tedford, R. H., and Barghoorn, S., 1999, Santa Fe Group (Neogene), Ceja del Rio Puerco, Northwestern Albuquerque Basin, Sandoval County, New Mexico, *in* Pazzaglia, F. J., and Lucas, S. G., eds., Albuquerque Geology: New Mexico Geological Society, 50th Annual Field conference, Guidebook, p. 327-335.

Underhill, J. R., and Woodcock, N. H., 1987, Faulting mechanisms in high-porosity sandstones; New Red Sandstone, Arran, Scotland, *in* Jones, M. E., and Preston, R. M.

F., eds., Deformation of Sediments and Sedimentary Rocks: London, The Geological Society, p. 91-105.

Watterson, J., Childs, C., and Walsh, J. J., 1998, Widening of fault zones by erosion of asperities formed by bed-parallel slip: Geology, v. 26, no. 1, p. 71-74.

Weber, K. J., Mandl, G., Pilaar, W. F., Lehner, F., and Precious, R. G., 1978, The role of faults in hydrocarbon migration and trapping in Nigerian growth fault structures, *in* Proceedings, Offshore Technology Conference, 10th, Houston: Dallas, Offshore Technology Conference, p. 2643-2653.

CHAPTER 3. CATACLASIS AND PARTICULATE FLOW IN FAULTED, POORLY LITHIFIED SEDIMENTS*

3.1. Abstract

Microscopic observations of faulted, poorly lithified sediments from the Rio Grande rift, New Mexico, U.S.A., reveal that the mode of grain fracture within the fault zone is controlled by relative grain strength. Transgranular fracturing of quartz is rarely observed - quartz typically deforms by flaking of grain edges, feldspar by transgranular fracture facilitated by easy cleavage, and lithic fragments by transgranular fracture or distributed microcracking. Particle size measurements indicate that progressive deformation produces a particle size distribution that can be described by power-law models, characterized by low D values (1.7 – 2.1). This indicates a preponderance of large particles beyond that expected for cataclasis by constrained comminution ($D \sim 2.6$). We interpret the results in terms of cataclastic deformation by controlled particulate flow under low confining pressure, in which extensive transgranular fracturing is not necessary

* Geoffrey C. Rawling and Laurel B. Goodwin, submitted to Journal of Structural Geology

for strain accumulation. This style of cataclastic deformation is different from that observed in crystalline and lithified sedimentary rocks. It is in part responsible for the characteristic internal structure and hydrologic properties of faults in poorly lithified sediments, and has implications for diagenetic processes and interpreting fault zone deformation history.

3.2. Introduction

Brittle faulting of porous sandy sediments and sedimentary rocks in the shallow crust is accomplished by cataclasis, a deformation mechanism which "...involves the brittle fragmentation of mineral grains with rotation of grain fragments accompanied by frictional grain boundary sliding and dilatancy" (Sibson, 1977). There is abundant evidence from field studies of faults in sandstones that cataclasis is the dominant low temperature deformation mechanism in sandstones, both in small displacement faults or deformation bands (Aydin, 1978; Underhill and Woodcock, 1987; Antonellini et al., 1994) and large displacement fault zones (Engelder, 1974; Blenkinsop and Rutter, 1986). This has been verified through experimental deformation of sandstones (e.g., Dunn et al., 1973; Menéndez et al., 1996; Wong et al., 1997).

Compared to lithified sandstones, there have been few studies of cataclasis in unlithified sediments. Antonellini et al. (1994) suggested that deformation bands in lithified sandstones formed without cataclasis under low normal stress conditions when the sandstones were not fully lithified. Lucas and Moore (1986) documented extensive cataclasis that occurred in accretionary wedges when the sediments were partially lithified. Hooke and Iverson (1995) presented evidence for cataclasis in deformed glacial

till. Although primarily concerned with fault-zone cementation and effects of faults on fluid flow, Mozley and Goodwin (1995), Heynekamp et al. (1999), and Sigda et al. (1999) noted evidence for cataclasis in studies of faults in poorly lithified sediments. Recently, Cashman and Cashman (2000) documented cataclasis in deformation bands in unlithified Pleistocene sands, and argued that they formed under very low confining pressure, possibly during seismic slip events. Cataclasis has been observed in laboratory deformation of various granular materials and sand (Borg et al., 1960; Mandl et al., 1977; Marone and Scholz, 1989; Been et al., 1991).

The particle size distribution (PSD) of cataclastically deformed materials is of particular importance for elucidating the micromechanics of the deformation process. Sammis et al. (1987) investigated the PSD of gouge from a large-displacement fault in crystalline rock over four orders of magnitude of particle sizes They concluded that the gouge was self-similar, or fractal, in terms of the number of particles vs. their size. That is, the gouge appeared identical when viewed at different scales. Mathematically, this means that the relationship between particle frequency and size can be described by a power law, and the number of particles larger than a given size versus that size plots as a straight line on a double log plot, the slope of which is the fractal dimension, D. Sammis et al. (1987) proposed a simple constrained comminution model for the development of this gouge texture in which the probability of fracture of a particle is independent of its size or strength but strongly dependent on the size of its nearest neighbors. In the model, when two particles of equal size come into contact, one will fracture. Particles with nearest neighbors of similar sizes are most likely to fracture, and, in the limit, this will result in a statistically self-similar gouge with a fractal dimension D of ~ 2.6. This results

in a characteristic microstructure of relict grains surrounded by a matrix of comminution debris, in which no two particles of similar size are nearest neighbors.

Blenkinsop (1991) measured the PSD of gouges from crystalline and lithified sedimentary rocks and observed D values from 1.88 to 3.08. In a study of gouges derived from crystalline rocks from three faults in Southern California, An and Sammis (1994) observed that PSDs for the smaller particles are generally consistent with a power law, or fractal, distribution with D values of 2.5-3.0. The fractal distributions broke down at larger particle sizes. Marone and Scholz (1989) deformed an artificial gouge of Ottawa sand between steel blocks to varying strains. The D value of the resulting PSDs increased with increasing shear strain and reached a plateau of ~2.6 at a shear strain of about 2, supporting the constrained comminution model of Sammis et al. (1987). However, they observed larger D values and smaller average grain sizes in localized, Reidel shear zones.

In most studies, the actual process of cataclasis under hydrostatic compaction or shear deformation has been observed to be transgranular fracturing initiated by loading at grain-to-grain contacts (e.g., Zhang et al., 1990; Antonellini et al., 1994; Menéndez et al., 1996). Exceptions include Hooke and Iverson (1995), who suggested that abrasion, flaking, or spalling from grain edges was the mode of fracturing in deformed glacial till; Marone and Scholz (1989), who observed that hydrostatically compressed gouge particles showed fracture dominantly along their edges; and Blenkinsop (1991), who related low D values (<2) to in-situ alteration, intermediate D values ($2<D<3$) to deformation by constrained comminution and high D values (>3) to selective fracture of large particles after strain localization.

The above discussion focuses on the nature and occurrence of grain fracturing. The other component of cataclasis as defined by Sibson (1977) is frictional grain boundary sliding. Borradaile (1981) treated cataclasis as a particular example of the more general deformation mechanism of particulate flow, of which he identified three types. Independent particulate flow involves grain boundary sliding with no intragranular deformation. Dependent particulate flow occurs when grains cannot move relative to one another unless there is intragranular deformation, such as crystal plasticity, diffusive mass transfer, or fracturing. In controlled particulate flow, the rate of grain boundary sliding is controlled by intragranular deformation, but the amount of sliding of any individual grain is not limited by this deformation. Other workers (e.g., Porter et al., 2000) use the term particulate flow more generally to refer to deformation accommodated by frictional sliding alone, with no grain breakage or other deformation.

The variety of observations and models proposed suggests that further investigation into the occurrence and micromechanisms of cataclasis is warranted. In this study, we present evidence for cataclasis in immature, poorly lithified, Tertiary sediments naturally deformed under low confining pressures from the Sand Hill fault zone, Albuquerque Basin, and from individual deformation bands within similar Tertiary sediments in the Socorro Basin. Both basins are within the Rio Grande rift, New Mexico, USA. Microstructural observations with optical, back-scattered electron (BSE) and secondary electron (SE) microscopy indicate that the mechanism of grain breakage varies with mineralogy and relative strength. The observations are consistent with PSD measurements, which indicate a greater proportion of large grains in the faulted sediments than predicted by the constrained comminution model. We interpret these

observations as the result of deformation under low confining pressures and posit that this is an explicit example of controlled particulate flow, as it appears that the amount of grain boundary sliding is more than would be required by or dependent on the fracturing of grains (Borradaile, 1981). These results have implications for the formation of macroscopic fault zone structures, interpretation of deformation history, fault zone diagenesis, and the impacts of such faults on subsurface fluid flow.

3.3. Geologic Setting and Study Areas

3.3.1. Sand Hill Fault Site

The first study site is the Sand Hill fault. It is one of the major normal faults bounding the Rio Grande rift, and marks the western margin of the Albuquerque basin (Hawley et al., 1995; Figure 18). It is a growth fault juxtaposing synrift sediments of the Pliocene-Pleistocene upper Santa Fe Group against middle Miocene to Oligocene sediments of the lower and middle Santa Fe Group. Based on outcrop observations and geophysical and borehole geological data, displacement increases from ~10 to ~600 m downdip (Hawley et al., 1995; Heynekamp et al., 1999). The lower Santa Fe Group sediments are dominantly fine-grained sand, with subordinate medium-grained sand, silty sand, and mud. These sediments were deposited in dune, fluvial, and mixed playa and dune environments. The upper Santa Fe Group sediments are largely fluvial, with minor aeolian deposits, and include sand, silt, and mud, locally capped by gravel (Tedford and Barghoorn, 1999). In the area sampled, the footwall sediments cut by the fault are arkoses, lithic arkoses, and feldspathic litharenites (Beckner and Mozley, 1998; Figure 19). Most of the lithic fragments (70-90%) are volcanic rock fragments. Excepting zones

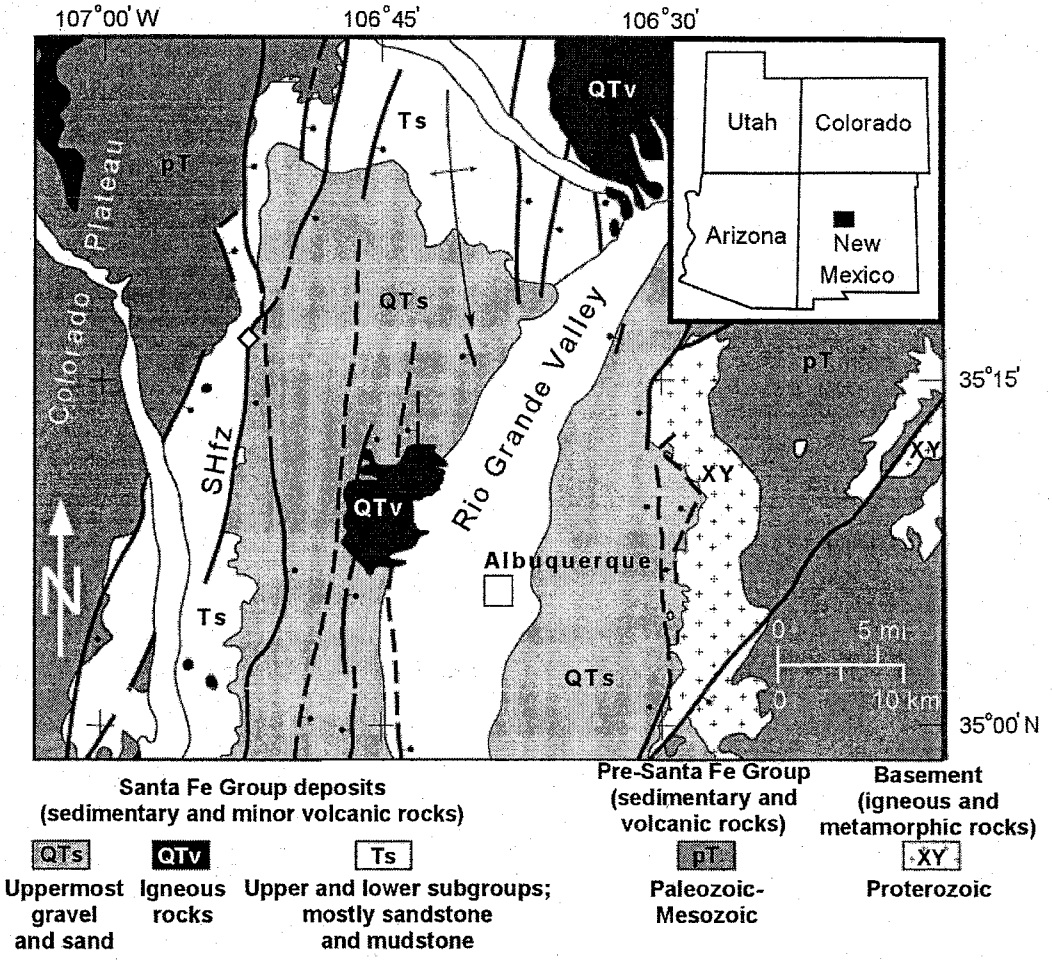

Figure 18. Study site (open diamond) along Sand Hill fault zone (SHfz) in Albuquerque basin of Rio Grande rift. Inset shows regional location. Faults are generalized; not all faults are shown. Modified from Hawley et al. (1995) and Hawley (1996) by S. Connell. The second site is south of the map area shown (cf. Herrin, 2001).

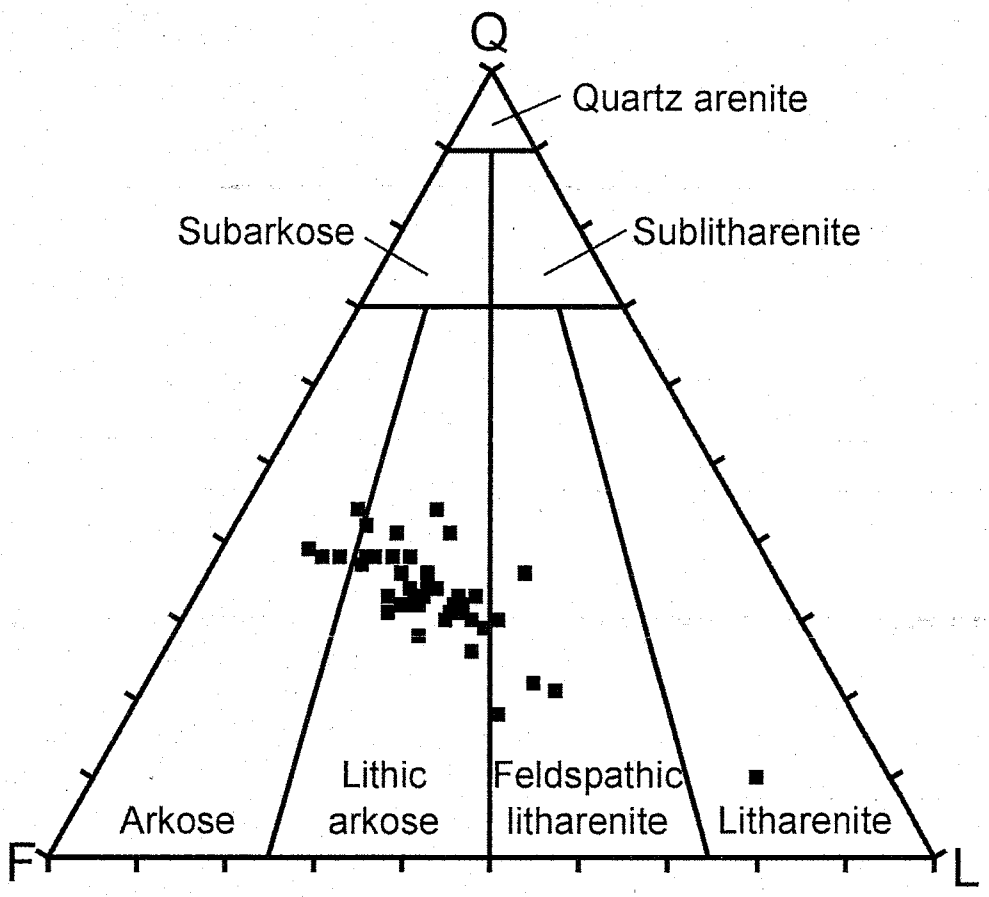

Figure 19. Ternary diagram showing the relative proportions of quartz (Q), feldspar + granitic/gneissic fragments (F) and lithic fragments (L) in thin sections of sediments from the footwall of the Sand Hill fault at the Waterfall site. Data from Beckner (1996). Sandstone classification from Folk (1974).

of calcite cementation (Mozley and Goodwin, 1995), all of the adjacent sediments and materials in the fault zone are friable and easily disaggregated, The sediments are weak enough to be excavated by hand, but strong enough to form vertical cliffs. Stratigraphic constraints (Connell et al., 1999; Tedford and Barghoorn, 1999; S. Connell, written communication, 2001) and vitrinite reflectance data (William Shea, personal communication, 1998) suggest that current exposures of the Sand Hill fault were never buried more than 1 km. This limits confining pressure during deformation to 20-30 MPa.

3.3.2 Fault Zone Structures

Fractures are the basic structural unit of faults in crystalline or lithified, low porosity sedimentary rocks. The internal structure of these faults can be subdivided into three architectural elements representing a progressive increase in deformation intensity and slip localization: protolith, damage zone, and core (Caine et al., 1996). Faults in lithified, high porosity sandstones have deformation bands (narrow, tabular zones of displacement, compaction, and/or cataclasis) as a basic structural unit and eventually develop discrete, macroscopic slip surfaces, which are effectively fractures with regard to fluid flow (Aydin, 1978; Aydin and Johnson, 1978; Underhill and Woodcock, 1987; Antonellini et al., 1994; Antonellini and Aydin, 1995). Faults in poorly lithified sandy sediments in the Rio Grande rift also have deformation bands as a basic structural unit but do not contain macroscopic fractures (Heynekamp et al., 1999; Sigda et al., 1999, Chapter 4). Where displacement is greater than the local mean bed thickness, large-displacement faults in poorly lithified sediments, exemplified by the Sand Hill fault, have an additional architectural element, the mixed zone, between the damage and core zones (Mozley and Goodwin, 1995; Heynekamp et al., 1999; Chapter 4; Figures 20 and 21).

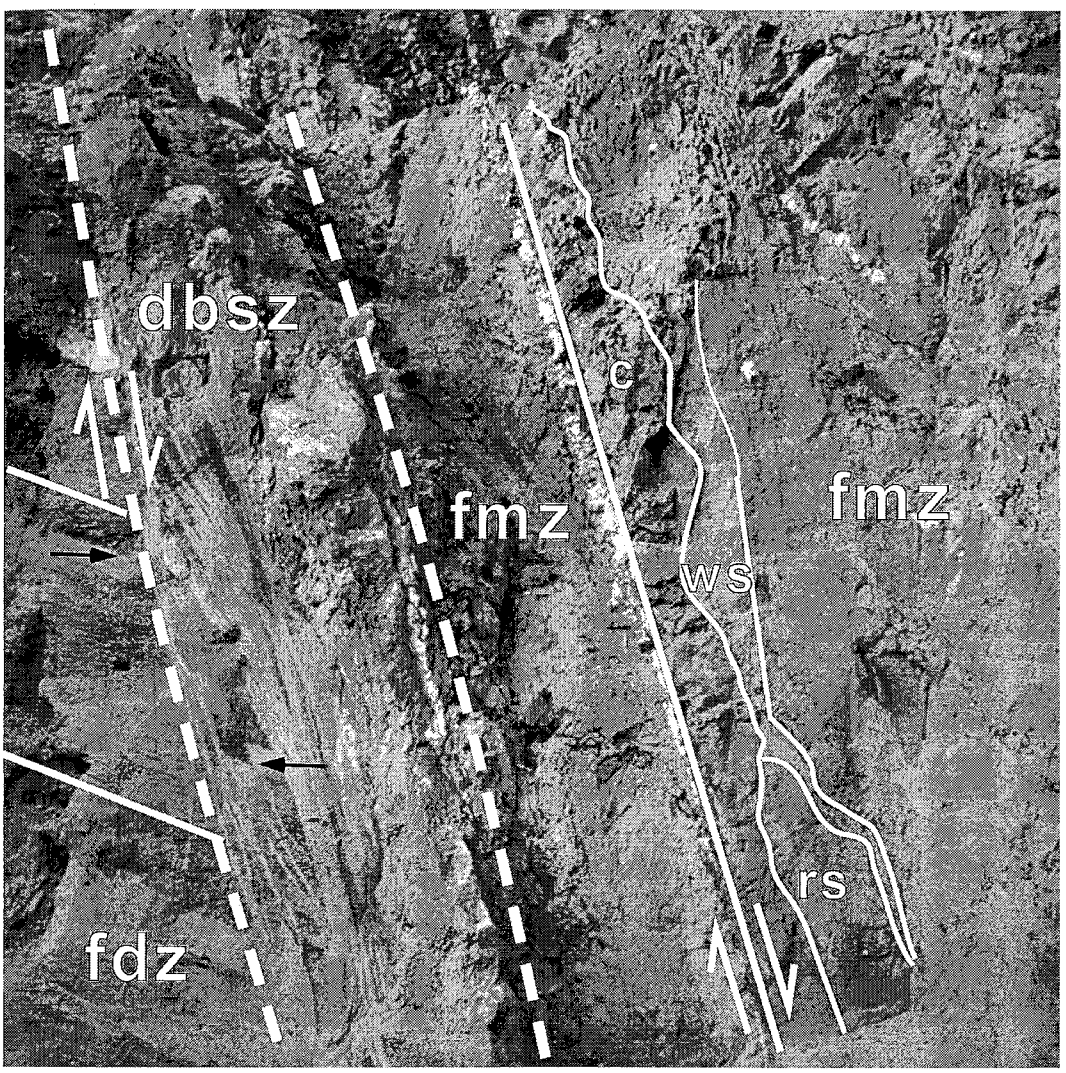

Figure 20. Shear zone of coalesced deformation bands (DBSZ, outlined by dashed lines) forming contact between footwall damage zone (fdz) and footwall mixed zone (fmz) within Sand Hill fault zone. Viewed to the north. Core zone and main slip surface of fault are right of the fmz (east). Offset is at least several meters. Solid lines delineate tilted bedding in fdz and clay-rich (c), white sand (ws), and red sand (rs) beds transposed into foliation in fmz. Black arrows indicate offset of coarse-grained layer across part of DBSZ (see text). Width of photo is 3m.

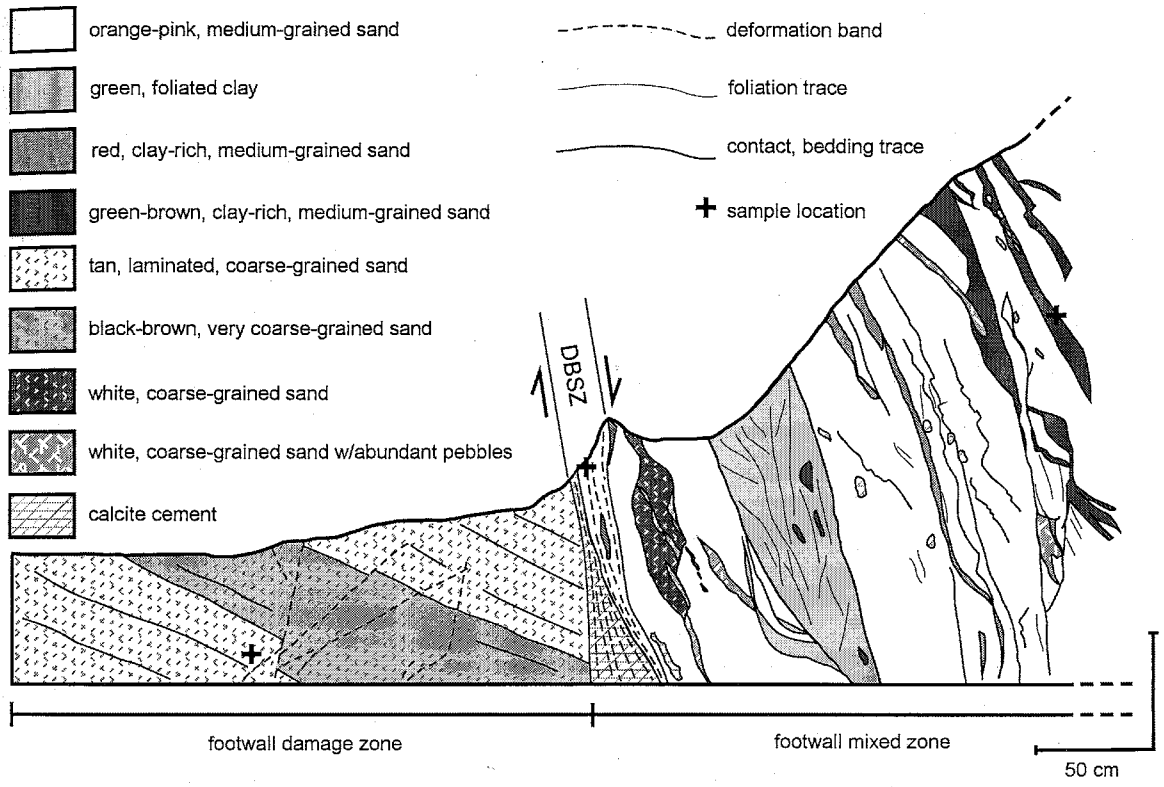

Figure 21. Map of excavated outcrop in footwall of Sand Hill fault zone. Viewed to the north. Fault core is beyond right (east) side of excavation. Crosses show locations of one of each of the protolith (sediment from damage zone), mixed zone, and deformation band shear zone (DBSZ) samples. Complex mixed zone relationships largely represent sedimentary layers transposed into fault-parallel compositional foliations, with local development of shear zones and intense sediment mixing along relict sedimentary contacts.

Mixed zones are compositionally and structurally heterogeneous. The degree of deformation may range from rotated but intact bedding, to bedding transposed into foliation, to penetrative deformation in the form of sediment disaggregation and mixing at the grain scale, all within the range of a meter or less. Commonly the boundary between the mixed zone and protolith is a shear zone of coalesced deformation bands (deformation band shear zone, hereafter referred to as DBSZ; Chapter 2). These shear zones represent localization of deformation (Figure 20) and concentrated cataclasis. In general, it is not possible to estimate the amount of shear strain across the mixed zone, as offset on the fault is too great. However, a lower bound on the shear strain in the DBSZ of $\gamma = 7$ to 11 at the Sand Hill fault site is obtained from the offset of a sliver of coarse-grained sediment (Figure 20).

3.3.3. Bosque del Apache Site

The second study site is at the southern margin of the Socorro Basin in central New Mexico, approximately 160 km south of the Sand Hill fault site. It is a railroad cut within the Bosque del Apache National Wildlife Refuge in which are exposed sand, gravel, and conglomerate beds of the Popatosa Formation of the Lower Santa Fe Group (Herrin, 2001). The sands and gravels represent alluvial fan, transitional fan, and eolian facies. Compositional data for the undeformed and deformed sands are given in Figure 22. Although the gravel beds are moderately indurated, the sands are poorly lithified and easily excavated by hand. The outcrop is 135m long and is cut by numerous DBSZs and two faults with slip surfaces, all of which strike northwest-southeast and have normal slip sense (Herrin, 2001). Structures dip both northeast and southwest. Maximum burial is not

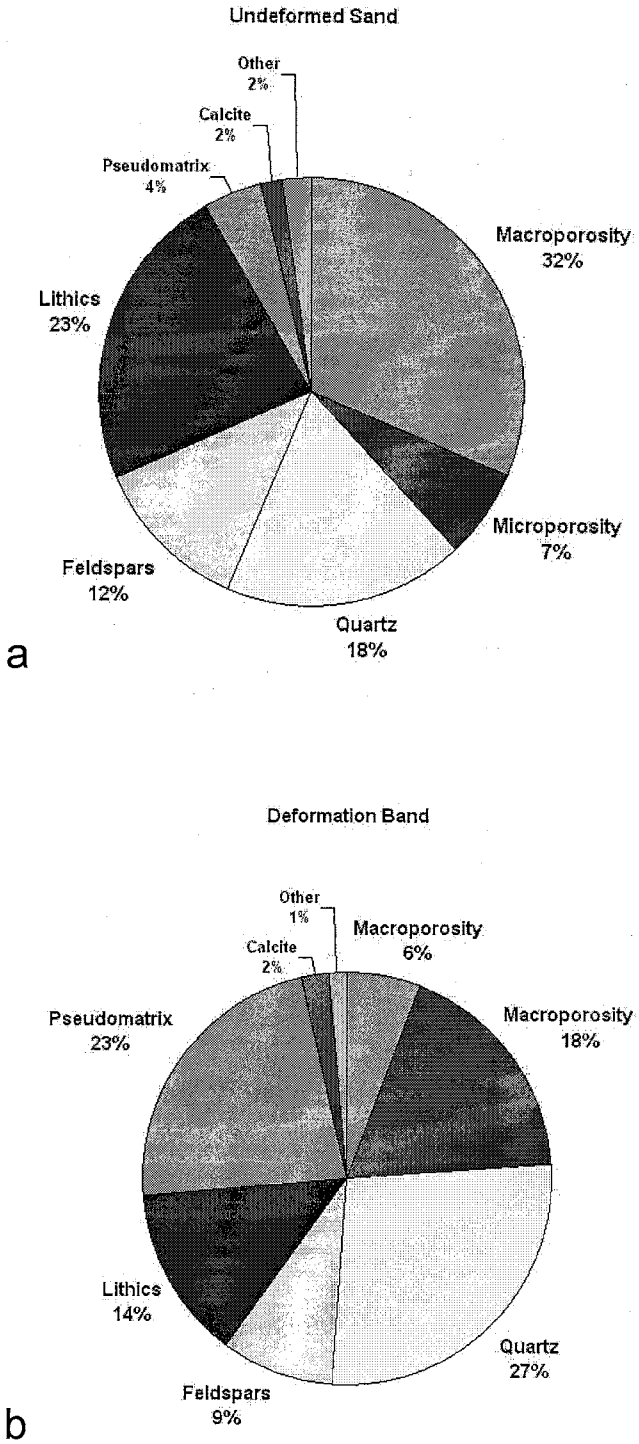

Figure 22. Compositional data from the Bosque del Apache site. **a)** Average of five point counts of the host sand. **b)** Average of five point counts of the deformation band shear zone. Data from Herrin (2001).

well constrained, but stratigraphic considerations suggest it is no greater than at the Sand Hill fault site, with similarly low confining pressures during deformation. The DBSZ studied is 10cm wide and has a throw of ~3m, resulting in a shear strain of $\gamma = 30$ across the DBSZ.

3.4. Methods

3.4.1. Sample Collection

We collected two samples each from the protolith (undeformed material within the damage zone), mixed zone, and DBSZ for PSD measurements from the footwall of the Sand Hill fault. Three of the samples were collected from the outcrop shown in Figure 21. The mixed zone and DBSZ regions sampled do not represent deformed equivalents of the adjacent protolith sediment; displacement on the fault is too great to track individual beds into the fault zone. At the Bosque del Apache study site an isolated DBSZ cutting a thick sand layer and the host sand were sampled, allowing direct comparison of a deformed sand with its protolith.

The samples were collected by gently excavating a small hole in the outcrop with a paint scraper and brushing ~3 cm^3 of loose sediment into a plastic container. In most cases, excavation and subsequent mild shaking of the sediment were sufficient to completely disaggregate the sample. We also collected multiple hand samples from all parts of the fault zone at the Sand Hill fault site for petrographic analysis by drilling into the outcrop with a hole saw and surrounding the sediment core with expanding insulation foam (method by B.C. Dimeo, personal communication, 1997).

3.4.2. Particle Size Measurement

We measured particle size distributions with Scion Image image analysis software interfaced with a video camera attached to a petrographic microscope. A small portion of the sample was scattered onto a glass slide and the slide was traversed until 30 or 60 non-overlapping images of the disaggregated grains were collected. A magnification of 4x was used, which provides a resolution (smallest resolvable particle size) of 0.0064 mm and a large enough depth of field that all visible particles were in sharp focus for accurate digitization. The largest particles observed were 0.5 to 0.7 mm in diameter for all datasets, resulting in an observable size range of two orders of magnitude. This size range is the same as that considered by Blenkinsop (1991). Typically, several hundred grains were visible in each image, and no particles larger than the field of view were encountered. The greyscale images were converted to pure black (grains) and white (background) images and touching grains were separated manually in each image. Using code written in the Scion Image macro language, we calculated the nominal section diameter and corrected count for each grain. The nominal section diameter is the diameter of a circle equal in area to the area of the grain in the plane of its largest and intermediate diameters (Mazzulo and Kennedy, 1985) and is calculated based on the digitized projected area of the grain. This method gives a direct estimate of the size of the grain in three-dimensional space, because the images are projections of the grains, not slices through them (as in a thin section). The corrected count accounts for the fact that large grains are more likely to intersect the edge of the image, and thus their area cannot be determined, and they cannot be counted. This would result in the larger grains being underrepresented in the PSD. The corrected count of each grain is defined as

$$(W_x W_y)/((W_x - F_x)(W_y - F_y)) \quad (3.1)$$

where W_x and W_y are the image widths in the X and Y directions and F_x and F_y are the maximum grain dimensions, or caliper dimensions in the X and Y directions (Russ, 1991; Russ, 1999 p. 529-532). Thus the count of each grain is a real number (say, 1.15), not the integer 1, and the corrected count increases with grain size. In this study, we found that using corrected or uncorrected counts has little effect on the resulting PSDs or the fitted models.

The raw data of calibrated grain sizes and corrected counts were output from Scion Image as a text file and cumulative particle size distributions were calculated with a FORTRAN program. Consistent with previous workers (Sammis et al., 1987; Marone and Scholz, 1989) we estimated counting errors by assuming the data were selected from a Poisson spatial distribution of particles (Wilson, 1952). The data are presented as cumulative distributions in log(number) – log(size) space. This follows directly from the definition of a fractal set:

$$N = C/r^D \quad (3.2)$$

where N is the number of objects with a characteristic linear dimension greater than r, C is a constant, and D is the fractal dimension (Turcotte and Huang, 1995). We used a weighted, least-squares routine to fit a power law model to the linear regions of the data sets. The weights are based on the standard deviation of the measurements, thus giving greater weight to data points representing more counts.

To check the precision and accuracy of this method, we measured the PSD of a sample of crushed quartz sand by both our image analysis method and traditional sieving

techniques. Unless the particles under consideration are perfect spheres, accuracy is extremely difficult to determine or even define for PSD measurements, as different size measurement techniques measure different size and/or shape attributes of the particles and all report particle size as some convolution of size and shape (Kennedy and Mazzulo, 1991; McCave and Syvitski, 1991). Differences between techniques increase with increasing irregularity in particle shape. To a first approximation, sieving yields particle size as the intermediate axis of the particle, whereas projected images of grains on a slide include the intermediate and long axes of the particles, and the derived nominal sectional diameter is probably a closer measure of the true particle size (Mazzulo and Kennedy, 1985). Thus, for a given particle, sieving yields a smaller size estimate than the nominal section diameter determined from image analysis. Of greater importance is whether a given technique reproduces the true shape of the PSD being investigated, e.g. the number of modes, the skewness, etc. PSDs determined by sieving are by weight, i.e., they report the distribution of particle sizes as a function of the weight of the particles in each size class. To compare our two datasets, we converted the PSDs by number from the image analysis method to PSDs by weight by calculating an equivalent spherical weight for each measured grain. This was done by calculating the volume of a sphere with the same diameter as the nominal section diameter, and assuming a grain density of 2.65 g/cm^3.

The shape of the PSD of the crushed quartz sand determined by image analysis closely matched that determined from sieving and, as would be expected from the above discussion, was offset to larger particle sizes by ~ 150 μm (Figure 23). This offset is larger than that observed by Mazzulo and Kennedy (1985) in a similar comparison, but

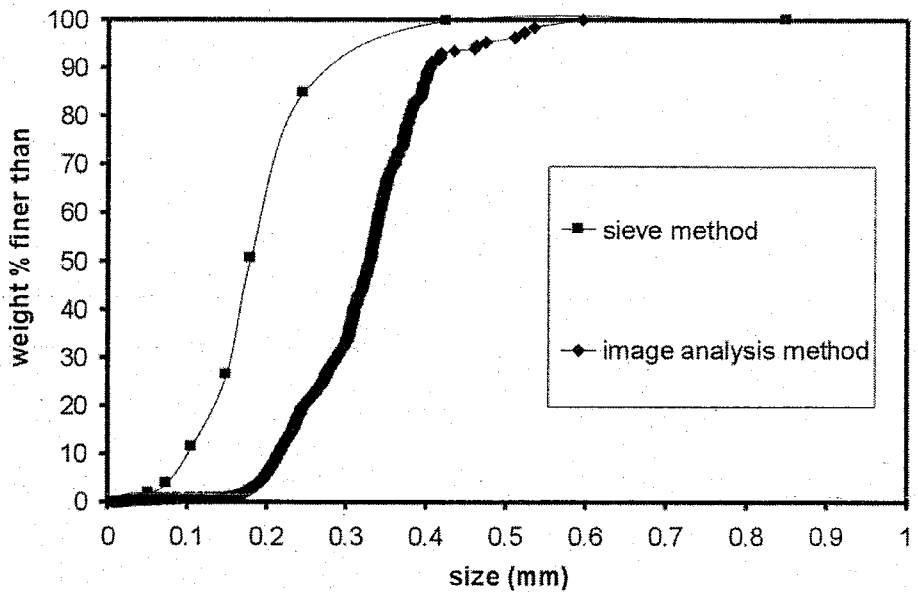

Figure 23. Crushed quartz sand PSDs by weight determined by seiving and image analysis methods. Image analysis distribution by number was converted to distribution by weight by calculating equivalent spherical sizes from nominal section diameters and assuming a density for all particles of 2.65 g/cm^3.

the crushed quartz particles in our test were highly angular whereas Mazzulo and Kennedy (1985) studied well rounded beach sands. We conclude that the imaging technique provides a sufficiently accurate and precise measure of the PSD over the size range investigated (0.006 mm to ~1mm). Its advantages are that minimal sample preparation is required, very small samples can be easily measured, thousands of grains can be quickly counted, and the derived nominal section diameters of individual grains are probably a better measure of the true particle size.

3.4.3. Microscopy

Thin sections were made from Sand Hill fault samples impregnated with low viscosity epoxy; however, the samples were extremely fragile and friable and plucking is a problem in thin-section preparation. We examined the thin sections with optical and back-scattered electron (BSE) microscopy. We also examined loose grains from subsets of several of the Sand Hill fault PSD samples to characterize grain-surface morphology. The grains were boiled for 10 minutes in concentrated HCl, rinsed with water and acetone, and air-dried. They were then mounted on double-sided tape on stubs, carbon-coated, and observed with a Cameca SX-100 electron microprobe in secondary electron mode (SEM). Several dozen grains were examined from each sample, which is a sufficient number to address the variability in the samples (Krinsley and Doornkamp, 1973). We did not make thin sections or grain mounts of the Bosque del Apache samples. However, previous studies indicate that the sands and DBSZs at this site are compositionally, petrographically, and microstructurally similar to the sands at the Sand Hill fault study site (Sigda et al., 1999; Herrin, 2001; Figures 19 and 22).

3.5. Results

3.5.1. BSE and SEM Microscopy

In BSE images of thin sections, mixed zone and DBSZ samples typically exhibit rounded relict grains, with their interstices filled by smaller, more angular grains, fine grained comminution debris, agglomerations of clay-size particles and occasional irregular blebs of calcite (Figure 24a). The large grains commonly touch and generally are not surrounded and isolated from their neighbors by finer-grained matrix. Transgranular fractures are rare. At higher magnifications it is apparent that much of the comminution debris is composed of small quartz fragments (Figure 24b). The most striking observation is that many of the quartz grains have ragged perimeters with fresh conchoidal fracture surfaces (Figures 24b and c). Figure 24c shows a typical example of a quartz grain with fresh conchoidal fractures around ~ 50% of its margin and rougher, but less angular, surface textures around the remainder. The matching of elongate, sharp flakes to adjacent fresh fractures is quite common. Occasionally flakes are seen still partially attached to the host grain. Conspicuous by their scarcity are transgranular fractures that shatter grains into highly angular fragments, and large numbers of blocky or tabular fragments bound by smooth, curved surfaces that would be the product of such fracturing. These more typical cataclastic textures have been observed in naturally deformed sands and sandstones (e.g., Lucas and Moore, 1986; Antonellini et al., 1994), and have been created in experimentally deformed sand and sandstone (e.g., Borg et al., 1960; Marone and Scholz, 1989; Menéndez et al., 1996). Most of the transgranular fractures in samples from the Sand Hill fault were observed in feldspars (Figure 24d) and volcanic lithic grains. Volcanic lithic grains also commonly deform by distributed

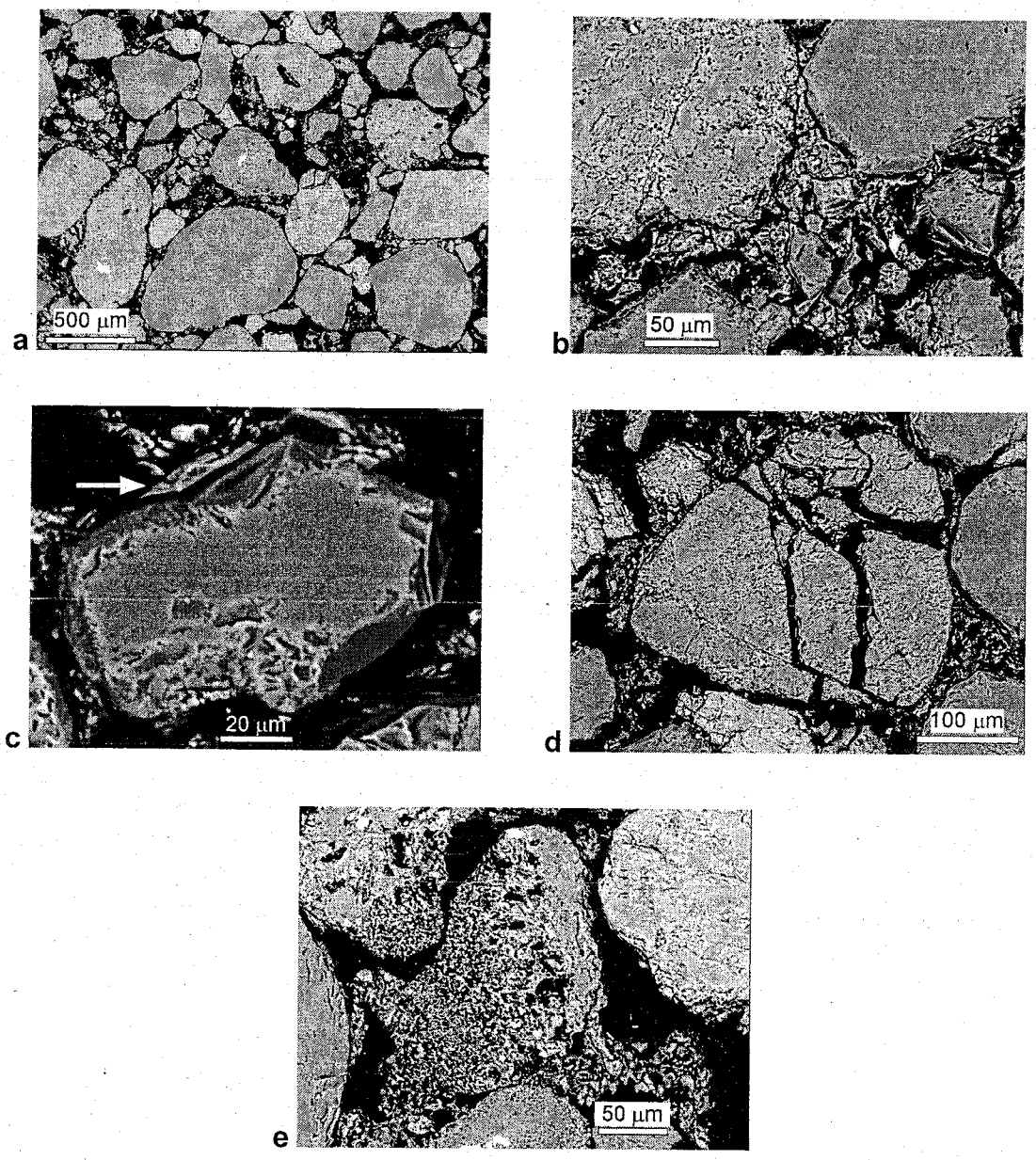
a
500 µm
b
50 µm
c
20 µm
d
100 µm
e
50 µm

Figure 24. Back-scattered electron images from DBSZ at Sand Hill fault site (following page). **a)** Typical texture evident in thin section. Note large, rounded relict grains touching each other and scarcity of transgranular fractures. Quartz is dark gray and smooth; feldspar and lithic fragments are light gray and rough. Large black spaces are gaps left by plucked grains. **b)** Close-up of fine-grained material from DBSZ. Note conchoidal fractures on quartz grain margins and fine quartz flakes mixed with feldspar and clay(?) between sand grains. **c)** Quartz; approximately 50% of margin is composed of fresh, smooth conchoidal fracture surfaces. Note the elongate, sharp flake immediately adjacent to matching fracture surface (arrow). **d)** Feldspar broken by transgranular fractures. **e)** Apparently ductile deformation of a volcanic lithic fragment, probably by distributed microcracking and/or deformation following alteration.

deformation, which may be distributed microcracking of the fine-grained matrix of the grain (cf. Herrin, 2001) and/or deformation following alteration to minerals such as clays (Figure 24e).

SEM imaging of individual particles allows examination of the morphology of a large proportion of the particle's surface, and there is a large literature on the subject (see Krinsley and Marshall, 1987 for a review). However, it has the disadvantage of not preserving spatial relationships amongst the particles as in BSE imaging of thin sections (e.g., Figures 24a and c). We examined grains from the protolith, mixed zone and DBSZ. Protolith grains (Figure 25a) are well rounded and have surface textures such as v-shaped mechanical indentations, small upturned cleavage plates, and precipitated surface coatings indicative of their sedimentary and diagenetic history (cf. Krinsley and Doornkamp, 1973). No evidence of tectonic deformation was observed. Undeformed sand grains from the mixed zone and DBSZ are similar in appearance to protolith grains.

Many grains from the mixed zone, however, show evidence of flaking along their edges. For example, Figures 25b and c show a small area of fresh conchoidal fracture on an irregular quartz grain. The remainder of the grain surface may be older fractures covered with diagenetic coatings. Compared to the DBSZ sample, cleavage fragments and flakes are rare.

The majority of the grains from the DBSZ show shapes and surface textures indicative of cataclasis, consistent with optical and BSE observations in thin section. The differing modes of fracture of feldspars (largely transgranular fracturing), lithic fragments (alteration and/or crushing to fine particles and transgranular fracturing), and quartz (flaking of edges) are evident. Broken feldspars (Figure 25d) appear to be the products of

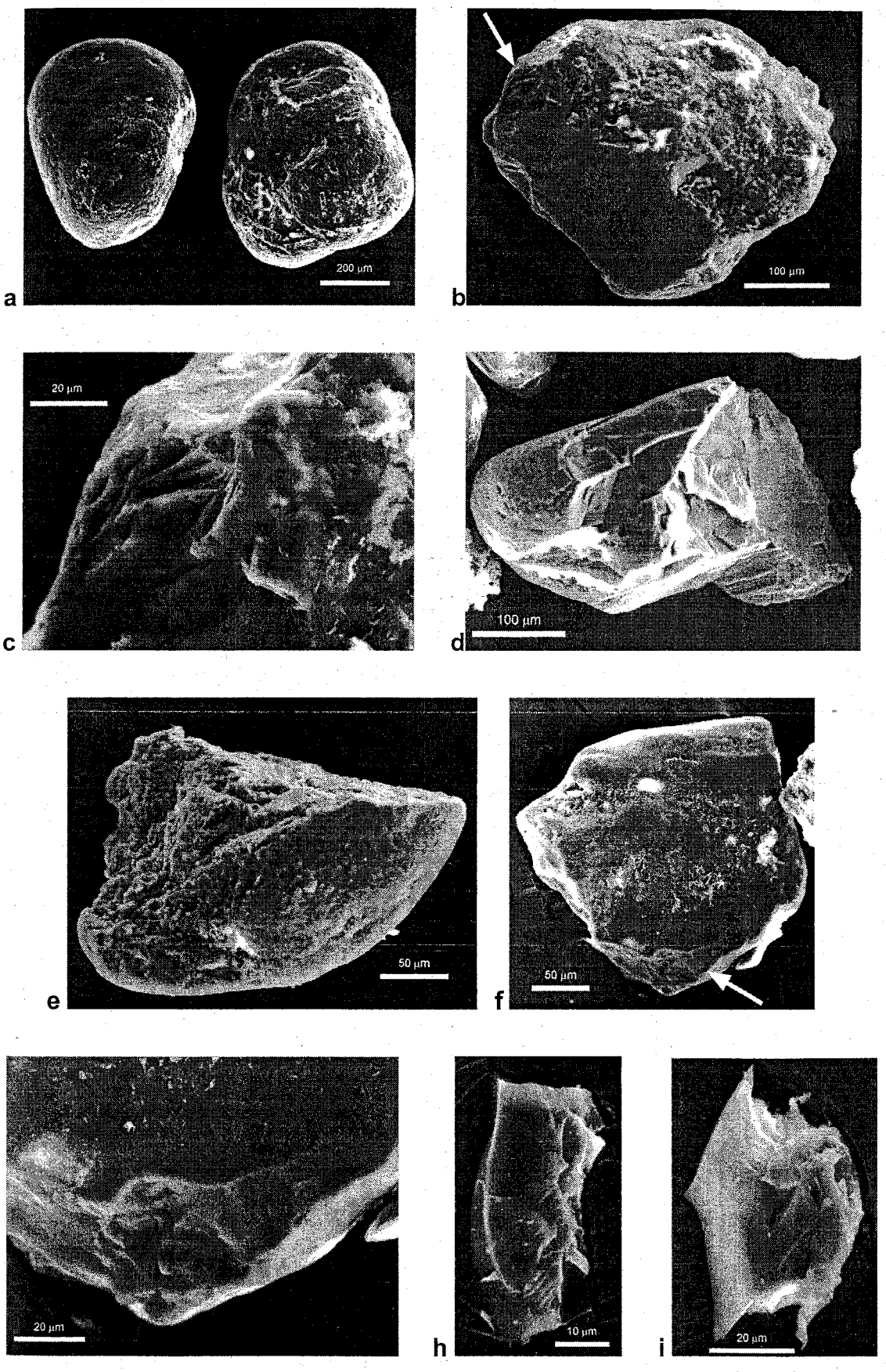
a
200 µm
b
100 µm
c
20 µm
d
100 µm
e
50 µm
f
50 µm
g
20 µm
h
10 µm
i
20 µm

Figure 25. Secondary electron images (following page): **a)** Undeformed quartz and lithic grains from protolith. **b)** Area of fresh conchoidal fracture (arrow) on quartz from mixed zone. Remainder of grain surface may consist of older fracture surfaces covered with diagenetic coatings. **c)** Close-up of region indicated by arrow in b). Note smooth, curving fracture surfaces, compared to other coated areas. **d)** Broken feldspar from DBSZ. **e)** Broken lithic fragment from DBSZ. **f)** Area of fresh conchoidal fracture (arrow) on quartz from DBSZ. **g)** Close-up of region indicated by arrow in **f)**. Note small (cleavage?) flakes on remainder of grain surface. **h)** and **i)** Quartz fracture flakes from DBSZ. Flakes are completely bounded by fresh, smooth, often ribbed conchoidal fractures, and have delicate protrusions.

transgranular fracturing of detrital grains. Rounded edges with relict sedimentary textures are visible adjacent to jagged edges composed of large, clean, fracture surfaces. The fractures in feldspar are largely cleavage-controlled. Figure 25e shows a lithic fragment with a similar overall morphology to the feldspar in 25d, but it is uncertain whether this grain deformed by transgranular fracturing or crushing and generation of fine particles (cf. Figure 24e).

Figures 25f and g show irregular quartz grains partly bounded by fresh, smooth, conchoidal fracture surfaces. The remainder of the surface textures appear similar to those of the protolith grains. Quartz fracture flakes are abundant in the DBSZ sample (Figures 25h and i). They have smooth, conchoidal fracture surfaces and extremely sharp, delicate edges. These flakes are the disaggregated equivalents of the flakes observed in thin section (e.g., Figures 24b and c), and most have dimensions on the order of 20 – 30 μm.

3.5.2. Particle Size Distributions

Sand Hill Fault Samples. The protolith samples (Figures 26a and b) are characterized by highly nonlinear PSDs with kinks at intermediate grain sizes. These data are consistent with field estimates of the relative particle size distributions of the two samples. The PSDs of both mixed zone samples (Figures 26c and d) show more subdued 'bumps'. In contrast, the PSDs of DBSZ samples are largely linear with tails at the smallest and largest grain sizes. Qualitatively, the progression from undeformed protolith to DBSZ involves a flattening of the PSD to a linear trend and a relative decrease in the number of intermediate sized particles. This progression is consistent with the field

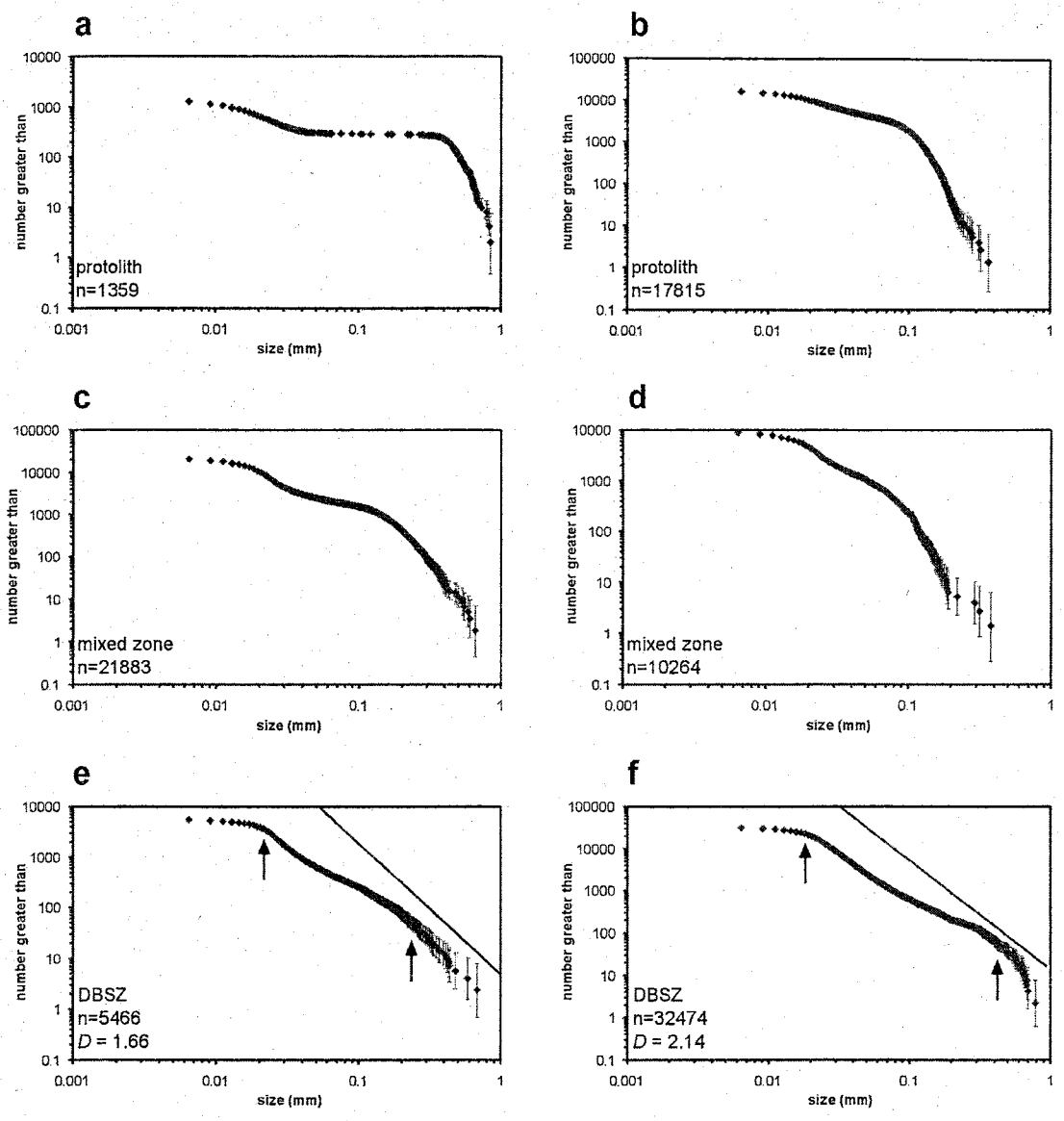

Figure 26. Sand Hill fault PSD data. Numbers of particles measured are indicated on each plot: **a), b)** protolith; **c), d)** mixed zone; **e), f)** DBSZ samples. *D* values from power law models are given. Dashed reference lines have slopes (*D* values) equal to 2.6.

interpretation that the DBSZ has undergone more intense, localized deformation than the mixed zone.

By the chi-squared goodness-of-fit test, a power law model adequately describes the PSD of both of the DBSZ samples (Figures 26e and f and Table 2). Although in both cases an acceptable fit can be made to the entire range of data, we have only used the most linear portion, bounded by the arrows in Figures 26e and f, in fitting the models. In terms of a fractal model, these are the lower and upper fractal limits (cf. Blenkinsop, 1991). The fitting parameters for these models and the resulting D values (power law exponents) are shown in Table 2. These D values are three-dimensional fractal dimensions because, as noted above, the particle sizes are nominal sectional diameters determined from projected areas of grains. The three-dimensional D values are 1.66 and 2.14 (Table 2), and indicate a greater proportion of large particles in the PSD than predicted by the constrained comminution model of Sammis et al. (1987; $D \sim 2.6$).

Bosque del Apache Samples. The PSDs of DBSZ material and its host sand at the Bosque del Apache site allow a direct comparison of a deformed sand with its protolith. Qualitatively, the undeformed and deformed sands show similar PSDs to the analogous Sand Hill fault materials (Figures 27a and b). The DBSZ data can be fit with a power law model over its entire range; however, we have only fit a model between lower and upper fractal limits as indicated (Figure 27b). The resulting three-dimensional D value is 2.07 (Table 2).

Table 2. Deformation band shear zone particle size distribution data.

Sample locality	n*	$D^{\dagger}$	$\chi^2 \leq \chi^2_{crit}$ ($\alpha = 0.01^{\S}$)		
Sand Hill fault	5466	1.66	4.6	<	404
Sand Hill fault	32474	2.14	15.7	<	664
Bosque del Apache	22729	2.07	20.5	<	434

* number of particles measured.
† power law exponent (3-D fractal dimension).
§ chi^2 goodness-of-fit test results at 99% confidence level.

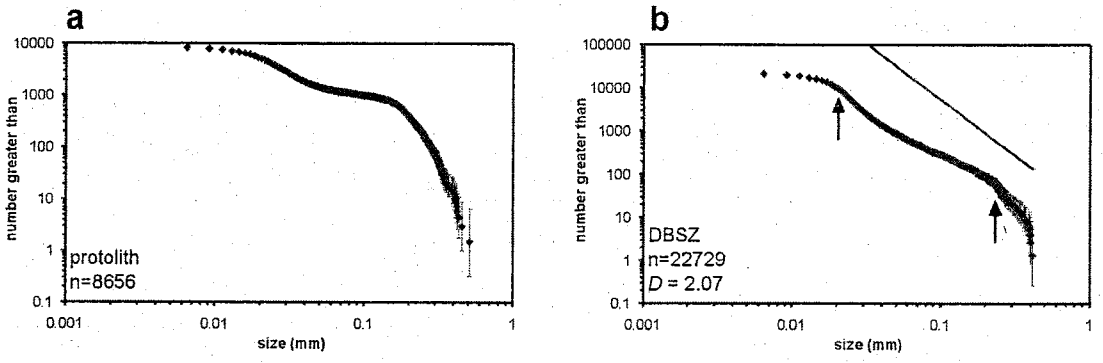

Figure 27. Bosque del Apache PSD data. Numbers of particles measured are indicated on each plot: **a)** protolith (compare with Figures 26a and b); **b)** DBSZ (compare with Figures 26e and f). *D* value from power law models is given. Dashed reference line has slope (*D* value) equal to 2.6.

3.6. Discussion

3.6.1. Mechanisms of Cataclasis

The constrained comminution model of Sammis et al. (1987) predicts that when two particles of equal size come into contact, one will fracture. Ultimately, this results in a characteristic microstructure in which large relict grains are surrounded by a finer grained matrix, and in general, no two grains of equal size are touching. This has been observed in natural (e.g., figure 22a in Blenkinsop, 1991) and artificial (e.g., figures 8a and b, Marone and Scholz, 1989) fault gouges. However, we observe in thin section that relict grains in our samples are relatively abundant and often in contact (Figure 24a), and transgranular fractures are relatively uncommon and appear to be mineralogy dependent. These facts, together with the observations of ragged edges on quartz grains, associated small quartz flakes, distributed deformation of lithic grains, progressive flattening of the PSDs, and the low D values of the DBSZ PSDs imply that the nature of cataclasis in poorly lithified sands is not constrained comminution.

The low D values, ~1.7 to 2.1, compared to the value of 2.6 predicted by constrained comminution, indicate that for a given number of large particles, there are fewer intermediate and small particles in deformed poorly lithified sediments (compare the PSDs with the reference lines in Figures 26e and f and 27b). The progressive flattening of the PSDs with increased deformation in both the Sand Hill fault and Bosque del Apache samples indicates that cataclasis preferentially removed the intermediate size particles. Many of the quartz flakes and conchoidal fracture surfaces on quartz grains have dimensions of roughly 20 – 40 μm (Figures 24b and c and 25b, g, h and i). If this is generally the case, then flaking of relatively small fragments from grain margins will

more efficiently break down the intermediate size particles in the PSD than the largest particles. Also note that this size range, 20 – 40 μm, corresponds to the upper tail, or fractal limit, of all three DBSZ PSDs (Figures 26e and f, and 27b). This may indicate that particles in this size range are the smallest that are produced in abundance during cataclasis, and that once produced, these fragments do not break down further.

Why is the mode of grain fracture different from constrained comminution? Hooke and Iverson (1995) studied the PSD of glacial tills that had undergone shear deformation. Recalculating PSDs by weight to PSDs by number, they observed D values that are slightly higher (2.84 – 2.96) than predicted by the constrained comminution model of Sammis et al. (1987), indicating more fine particles. Grain surface textures in deformed glacial tills were also indicative of cataclasis. They argued that the preponderance of fines was due to abrasion and chipping of particles as they slid past each other during deformation of the till. Transgranular fracturing was of secondary importance.

We believe the above scenario of cataclasis under low confining pressure, with a large component of grain boundary sliding, can explain our microstructural and textural observations and PSD data. Marone and Scholz (1989) conducted shear experiments on Ottawa sand at 20 MPa confining pressure to $\gamma = 2.3$. They observed fewer transgranular fractures in particles of all sizes and more spalling or flaking of grains than in experiments conducted at 100 MPa. The ragged grain boundaries on the larger particles and many quartz flakes in their photomicrographs (figures 9d and e of Marone and Scholz, 1989) are similar to the quartz textures from the Sand Hill fault zone. Many of

the smallest, most elongate flakes are comparable in size to those in this study. The D value they determined was 2.40, slightly less than the value for constrained comminution.

An important caveat is that our D values are lower than those of both Marone and Scholz (1989) and Hooke and Iverson (1995). There are several possible explanations for this. It may be a matter of degree; i.e., the proportion of available grains that are actively being flaked or crushed, and the number of flakes removed from each grain may vary. The grains imaged by Hooke and Iverson (1995; figure 3) are much more angular than those in this study. This also is apparent in the photomicrographs of Sammis et al. (1987) and Blenkinsop (1991), as may be expected in gouges derived from intact igneous and metamorphic rocks as opposed to our samples, which are derived from unlithified, rounded sedimentary grains.

The proportion of available grains that are being flaked or crushed may be related to mineralogy. Marone and Scholz (1989) deformed a starting material of nearly pure quartz sand, whereas our protolith materials have less quartz (Figures 19 and 22a). The protolith of the tills imaged by Hooke and Iverson (1995) was unspecified. Figure 22 shows the composition of material from a DBSZ and an adjacent undeformed sand at the Bosque site. The total proportion of framework grains (quartz + feldspar + lithic fragments) changes little from the undeformed sand (53%) to the DBSZ (50%). However, the relative proportion of quartz in this total increases from 34% in the undeformed sand to 53% in the DBSZ. This is consistent with flaking of small chips off of the margins of quartz grains being less efficient than wholesale fracturing at reducing the grain size. The decrease in percentage of lithic fragments and the increase in pseudomatrix suggests that many lithic fragments are being crushed and/or altered by diagenetic processes. In

general, the compositional data in Figure 22 are consistent with the microstructural observations. However, it seems likely that the D value of cataclastically deformed, poorly-lithified sediments may sensitive to composition. This warrants a more systematic study.

Another possible explanation for the low D values is that more of the deformation in our samples may be accommodated by grain boundary sliding during controlled particulate flow. This is explored further below.

3.6.2. Deformation Model

A simple explanation for the effect of confining pressure on the mode of grain fracture is provided by the grain bridge model. Mandl et al. (1977) observed via in-situ stress measurements that the state of stress in a deforming granular medium is highly heterogeneous. They attributed this to the formation and destruction of grain bridges coaxial with the applied maximum principal stress (Figure 28). Resistance to shear in the granular medium is provided by compressive stress across the grain bridges. Biegel et al. (1989) argued that failure of these grain bridges can be accomplished by slip along the boundaries of the shear zone, failure of asperities along the boundaries of the shear zone, intergranular slip between grains composing the bridge, or transgranular fracture of grains composing the bridge. They proposed that in most gouges, grain bridges fail dominantly by transgranular fracturing (Figure 28c), eventually resulting in fractal PSDs with D values of 2.6. Conversely, Hooke and Iverson (1995) hypothesized that grain bridges in deformed till failed largely by grain slippage with concomitant flaking or spalling (Figure 28b).

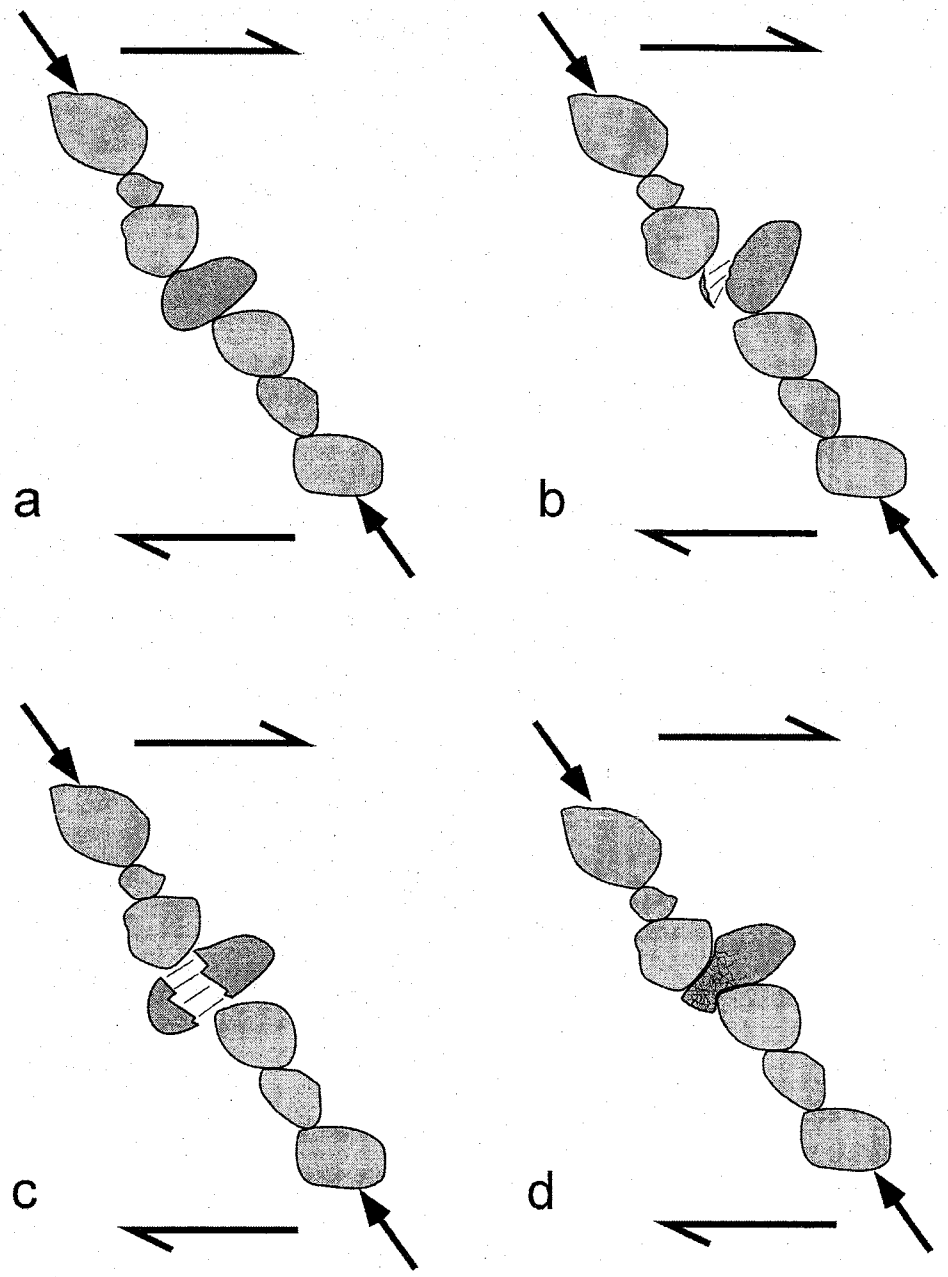

Figure 28. Grain bridge model for deformation within fault in poorly lithified sediment. **a)** Grains aligned coaxial to applied stress (arrows) offer resistance to shear within deforming zone. Concept after Biegel et al. (1989) and Hooke and Iverson (1995). Grain bridges may fail by **b)** flaking or spalling of quartz, **c)** transgranular fracturing of feldspar or lithic fragments, or **d)** distributed microcracking of lithic fragments.

The grain bridge model can also be applied to the Sand Hill fault zone, with the mode of failure of the grain bridge dependent in part on the mineralogy and relative strength of the particles in the bridge (Figure 28). Quartz grains fail by slip and associated abrasion or flaking (Figure 28b). Volcanic lithic fragments fail by transgranular fracturing or pervasive microcracking (Figures 28c and d), and feldspars fail by transgranular fracturing (Figure 28c). These processes, in concert with a large component of grain bridge failure by grain slippage alone, unaccompanied by cataclasis, can explain the lower D values we observe.

Deformation within the Sand Hill fault zone occurred dominantly by particulate flow of disaggregated sediment. Field evidence for this deformation mechanism includes transposition of bedding into foliation, resulting in macroscopically ductile-appearing structures, and the tectonic mixing of disparate sediment types (Heynekamp et al., 1999, Chapter 2). This style of deformation is commonly overprinted by later, more localized deformation in the form of deformation bands. The microscopic observations and PSD measurements presented here indicate that grain fracture occurred, but the relative movements of most grains did not require intense intragranular deformation. Borradaile (1981) defined controlled particulate flow largely in terms of strain rate, for which we have no constraints. However, we suggest that the flaking or spalling type of grain fracture of quartz during cataclasis in the Sand Hill fault, together with the low D values in the PSDs, are evidence for controlled particulate flow. The strong quartz grains fractured only enough to facilitate easy slip between adjacent grains. Often grains were able to move past each other with no intragranular deformation at all, resulting in lower D values than in the tills studied by Hooke and Iverson (1995). In this context, the extensive

transgranular fracturing causing the failure of grain bridges and accumulation of strain in fault gouges from crystalline and lithified sedimentary rocks is interpreted to be the product of dependent particulate flow. This is to say that, due to some combination of higher confining pressure, greater host rock stiffness, and the geometric constraints imposed by relatively rigid shear zone boundaries, grain size must be reduced by constrained comminution in the high-strain zone to allow continued localization of slip. Conversely, in the Sand Hill fault zone transgranular fracturing was largely a function of particle strength.

3.6.3. Implications

This study supports the observations of Lucas and Moore (1986) and Cashman and Cashman (2000) that cataclasis can occur during very low pressure deformation in poorly lithified and unlithified sediments. This has often been greeted with skepticism by structural geologists. However, as is apparent from our observations and those of the other studies summarized herein, there does not appear to be a simple, all-encompassing explanation for cataclasis in sediments and related materials. This warrants more detailed laboratory study, with particular emphasis on mechanical parameters that are difficult to constrain in the field, such as strain rate and fluid and confining pressure. Many important questions are unanswered. For example, based on ^{14}C dating of associated sediments, Cashman and Cashman (2000) suggested that the DBSZs in their study formed during seismic slip events. There are no such constraints in our study, and it is not known whether seismic slip rates are required for cataclasis in these materials.

Documentation of cataclasis in unlithified sediments implies that localized deformation may occur relatively soon after deposition of the sediments, or at least before

significant diagenesis. In the event that early-formed structures and textures are completely overprinted by later deformation, a potentially significant portion of the deformation history of the fault may be erased. Considering the Sand Hill fault, the microstructures and grain surface textures reported in this study would surely be lost if overprinted by constrained comminution after lithification. However, post-lithification deformation likely would be more localized, say in the form of discrete fractures, fracture networks, and relatively narrow zones of constrained comminution. Thus it is probable that prelithification structures and textures can be preserved through protracted postlithification deformation, and may in fact be recorded in the matrix between these later structures. Examination of lithified samples from greater depth along the fault, perhaps recovered from drill holes, could shed light on this issue. Our observations suggest a direction for consideration of the relative timing of formation of deformation bands and diagenesis of currently well lithified sandstones (cf. Byrne, 1994). Deformation bands that contain evidence for extensive transgranular fracture of quartz must have formed under higher confining pressure (e.g., Antonellini et al., 1994). Quartz grains deformed dominantly by flaking at the edges record deformation at lower confining pressure in a poorly lithified state, followed by diagenesis.

In addition, cataclasis in unlithified sediment may significantly impact subsequent diagenetic processes. Particle size reduction due to cataclasis may induce preferential cementation of the fault relative to the surrounding sediments due to the more reactive fine-grained comminution products and/or membrane effects during cross-fault flow (e.g., Whitworth et al., 1999).

An understanding of the nature of cataclasis in the unlithified sediments examined here is of more than structural interest. The grain scale deformation mechanisms in fault zones produce the macroscopic structures observed in the field. The macroscopic structures and their arrangement into architectural elements in the Sand Hill fault zone result in hydrologic properties of the fault zone as a whole that are distinctly different from brittle faults in crystalline and lithified sedimentary rocks (Chapter 4). For example, the mixed zone is an architectural element with physical and hydrologic properties which are the result of controlled particulate flow of sediment under low stress conditions. Thus, the deformation mechanisms operative during faulting, themselves the result of the interaction between protolith material properties, strain rate and confining pressure, etc., define the resulting hydrologic impact of the fault within regional groundwater flow systems. In petroleum reservoirs, in addition to effects on saturated permeability, cataclasis in poorly lithified sediments will make these structures more likely to act as capillary barriers.

3.7. Conclusions

Based on microstructural observations, grain surface textures, and PSD measurements of undeformed and deformed sediments from the Sand Hill fault zone and small-displacement deformation band shear zones, we note that the mechanism of cataclasis in poorly lithified sediments is different from constrained comminution. The style of grain breakage is dependent on relative grain strength. From strongest to weakest:

1) Quartz deformation was accomplished by flaking or spalling of small chips from the perimeters of grains.

2) Feldspars deformed by transgranular fracturing, facilitated by their strong cleavage.

3) Volcanic lithic grains deformed primarily by distributed microcracking and to a lesser extent, transgranular fracturing.

Deformation preferentially removes intermediate sized particles, resulting in a progressive flattening of the original PSDs. The PSDs of all of the deformation band shear zone samples can be described by power law relations, with D values of 1.7 – 2.1. These values are lower than those predicted by the constrained comminution model, and indicate a preponderance of large particles. The D values may also be sensitive to the composition of the sediments being deformed. Deformation in the unlithified sediments occurred by controlled particulate flow under low confining pressures (20-30 MPa). The cataclasis facilitated extensive grain boundary sliding, which accommodated the majority of the deformation. As the heavily faulted extensional basins of the western United States are filled with immature, poorly lithified sediments similar to the Santa Fe Group, we expect these conclusions to be generally applicable to many other fault zones.

3.8. Acknowledgements

Support was provided by the National Science Foundation (grants EAR-9706482 and EAR 9526983) and the New Mexico Geological Society. Thorough reviews by Julia Morgan and Haakon Fossen, and comments from Editor Jim Evans, greatly improved the manuscript. We are grateful to William Stone for discussions on data analysis, Sean Connell for discussions on Santa Fe group stratigraphy, Nelia Dunbar and Lynn Heizler

for assistance with the microprobe, Bruce Harrison for the use of his lab, and the U.S. Fish and Wildlife Service and Burlington Northern Santa Fe Railroad for granting access to the Bosque del Apache site. We thank Andy Dunn for the sieve analysis.

3.9. References Cited

An, L. -j., and Sammis, C., 1994, Particle size distribution of cataclastic fault materials from southern California: a 3-d study: Pure and Applied Geophysics, v. 143, p. 203-227.

Antonellini, M., and Aydin, A., 1995, Effect of faulting on fluid flow in porous sandstones: geometry and spatial distribution: American Association of Petroleum Geologists Bulletin, v. 79, p. 642-671.

Antonellini, M., Aydin, A., and Pollard, D. A., 1994, Microstrucuture of deformation bands in porous sandstones at Arches National Park, Utah: Journal of Structural Geology, v. 16, p. 941-959.

Aydin, A., 1978, Small faults formed as deformation bands in sandstones: Pure and Applied Geophysics, v. 116, p. 913-930.

Aydin, A., and Johnson, A. M., 1978, Development of faults as zones of deformation bands and as slip surfaces in sandstone: Pure and Applied Geophysics, v. 116, p. 931-942.

Beckner, J., 1996, Cementation processes and sand petrography of the Zia Formation, Albuquerque Basin, New Mexico. M.S. Thesis, New Mexico Institute of Mining and Technology, 146 p.

Beckner, J., and Mozley, P. S., 1998, Origin and spatial distribution of early phreatic and vadose calcite cements in the Zia formation, Albuquerque Basin, New Mexico, USA, *in* Morad, S., ed., Carbonate Cements in Sandstones: International Association of Sedimentologists Special Publication, v. 26, p. 27-51.

Been, K., Jefferies, M. G., and Hachey, J., 1991, The critical state of sands: Geotechnique v. 41, p. 365-381.

Biegel, R. L., Sammis, C. G., and Dieterich, J. H., 1989, The frictional properties of simulated gouge having a fractal particle distribution: Journal of Structural Geology, v. 11, p. 827-846.

Blenkinsop, T. G., 1991, Cataclasis and processes of particle size reduction: Pure and Applied Geophysics. v. 136, p. 59-86.

Blenkinsop, T. G., and Rutter, E. H., 1986, Cataclastic deformation of quartzite in the Moine Thrust Zone: Journal of Structural Geology. v. 8, p. 669-682.

Borg, I., Friedman, M., Handin, J., and Higgs, D. V., 1960, Experimental deformation of St. Peter sand: a study of cataclastic flow, *in* Griggs, D., and Handin, J., eds., Rock Deformation: Geological Society of America Memoir 79, Boulder, CO, The Geological Society of America, p. 133-191.

Borradaile, G. J., 1981, Particulate flow of rock and the formation of cleavage: Tectonophysics, v. 72, p. 305-321.

Byrne, T. 1994, Sediment deformation, dewatering and diagenesis: illustrations from selected melange zones, *in* Maltman, A., ed., The geological deformation of sediments: London, Chapman and Hall, p. 239-260.

Caine, J. S., Evans, J. P., and Forster, C. B., 1996, Fault zone architecture and permeability structure: Geology, v. 24, p. 1025-1028.

Cashman, S., and Cashman, K., 2000, Cataclasis and deformation-band formation in unconsolidated marine-terrace sand, Humboldt County, California: Geology, v. 28, p. 111-114.

Connell, S. D., Koning, D. J, and Cather, S. M., 1999, Revisions to the stratigraphic nomenclature of the Santa Fe Group, northwestern Albuquerque Basin, New Mexico, *in* Pazzaglia, F. J., and Lucas, S. G., eds., Albuquerque Geology: New Mexico Geological Society, 50th Annual Field conference, Guidebook, p. 337-353.

Dunn, D. E., LaFountain, L. J., and Jackson, R. E., 1973, Porosity dependence and mechanism of brittle fracture in sandstones: Journal of Geophysical Research, v. 78, p. 2403-2417.

Engelder, J. T., 1974, Cataclasis and the generation of fault gouge: Geological Society of America Bulletin, v. 85, p. 1515-1522.

Folk, R. L., 1974, Petrology of sedimentary rocks, Austin, TX, Hemphill, 182 p.

Hawley, J. W., 1996, Hydrogeologic framework of potential recharge areas in the Albuquerque basin, central New Mexico: New Mexico Bureau of Mines and Mineral Resources Open-File Report 402 D, Chapter 1, 68 p.

Hawley, J. W., Haase, C. S., Lozinsky, R. P., 1995, An underground view of the Albuquerque Basin, *in*, The Water Future of Albuquerque and the Middle Rio Grande Basin, Proceedings of the 39th Annual New Mexico Water Conference, New Mexico Water Resources Research Institute Report 290, p. 37-55.

Herrin, M., 2001, Characteristics of deformation bands in poorly lithified sand, Rio Grande rift, New Mexico. M.S. Thesis, New Mexico Institute of Mining and Technology, 81 p.

Heynekamp, M. R., Goodwin, L. B., Mozley, P. S., and Haneberg, W. C., 1999, Controls on fault-zone architecture in poorly lithified sediments, Rio Grande Rift, New Mexico: Implications for fault-zone permeability and fluid flow, *in* Haneberg, W. C., Mozley, P. S., Moore, K. C., and Goodwin, L. B., eds., Faults and subsurface fluid flow in the shallow crust: Washington, DC, American Geophysical Union, p. 27-50.

Hooke, R. L., and Iverson, N. R., 1995, Grain-size distribution in deforming sub-glacial tills: role of grain fracture: Geology, v. 23, p. 57-60.

Kennedy, S. K., and Mazzulo, J., 1991, Image analysis method of grain size measurement, *in* Syvitski, J. P. M., ed., Principles, methods, and application of particle size analysis: Cambridge University Press, p. 76-87.

Krinsley, D. H., and Doornkamp, J. C., 1973, Atlas of quartz sand surface textures: Cambridge University Press, 91 p.

Krinsley, D. H., and Marshall, J. R., 1987, Sand grain textural analysis: an assessment, *in* Marshall, J. R., ed., Clastic particles: New York, Van Nostrand Reinhold Company, p. 2-15.

Lucas, S.E., Moore, J.C., 1986, Cataclastic deformation in accretionary wedges: Deep Sea Drilling Project Leg 166, southern Mexico, and on-land examples from Barbados and Kodiak Islands, *in* Moore, J. C., ed., Structural fabrics in Deep Sea Drilling

Project cores from forearcs: Geological Society of America Memoir 166, Boulder, CO, Geological Society of America, p. 89-104.

Mandl, G., de Jong, L. N. J., and Maltha, A., 1977, Shear zones in granular material: an experimental study of their structure and genesis: Rock Mechanics, v. 9, p. 95-144.

Marone, C., and Scholz, C. H., 1989, Particle-size distribution and microstructures within simulated fault gouge: Journal of Structural Geology, v. 11, p. 799-814.

Mazzulo, J., and Kennedy, S. K., 1985, Automated measurement of the nominal sectional diameters of individual sedimentary particles: Journal of Sedimentary Petrology, v. 55, p. 593-595.

McCave, I. N., and Syvitski., J. P. M., 1991, Principles and methods of geological particle size analysis, *in* Syvitski, J. P. M., ed., Principles, methods, and application of particle size analysis: Cambridge, Cambridge University Press, p. 3-22.

Menéndez, B., Zhu, W., and Wong, T. -f., 1996, Micromechanics of brittle faulting and cataclastic flow in Berea sandstone: Journal of Structural Geology, v. 18, p. 1-16.

Mozley, P. S., and Goodwin, L. B., 1995, Patterns of cementation along a Cenozoic normal fault: A record of paleoflow orientations: Geology, v. 23, p. 539-542.

Porter, J. R., Knipe, R. J., Fisher, Q. J., Farmer, A. B., Allin, N. S., Jones, L. S., Palfrey, A. J., Garrett, S. W., and Lewis, G., 2000, Deformation processes in the Britannia Field, UKCS: Petroleum Geoscience, v. 6, p. 241-254.

Russ, J.C. 1991, Practical Stereology: New York, Plenum Press, 185 p.

Russ, J.C. 1999, The image processing handbook: Boca Raton, FL, CRC Press, 771 p.

Sammis, C., King, G., and Biegel, R., 1987, The kinematics of gouge deformation: Pure and Applied Geophysics, v. 125, p. 777-812.

Sibson, R. H. 1977, Fault rocks and fault mechanisms: Journal of the Geological Society of London, v. 133, p. 191-213.

Sigda, J. M., Goodwin, L. B., Mozley, P. S., and Wilson, J. L., 1999, Permeability alteration in small-displacement faults in poorly lithified sediments: Rio Grande Rift, Central New Mexico, *in* Haneberg, W. C., Mozley, P. S., Moore, K. C., and Goodwin, L. B., eds., Faults and subsurface fluid flow in the shallow crust: Washington, DC, American Geophysical Union, p. 51-68.

Tedford, R. H., and Barghoorn, S., 1999. Santa Fe Group (Neogene), Ceja del Rio Puerco, Northwestern Albuquerque Basin, Sandoval County, New Mexico, *in* Pazzaglia, F. J., and Lucas, S. G., eds., Albuquerque Geology: New Mexico Geological Society, 50th Annual Field conference, Guidebook, p.327-335.

Turcotte, D. L., and Huang, J., 1995, Fractal distributions in geology, scale invariance, and deterministic chaos, *in* Barton, C. C., and La Pointe, P. R., eds., Fractals in the earth sciences: New York, Plenum Press, p. 1-40.

Underhill, J. R., and Woodcock, N. H., 1987, Faulting mechanisms in high-porosity sandstones; New Red Sandstone, Arran, Scotland, *in* Jones, M. E., and Preston, R. M. F., eds., Deformation of Sediments and Sedimentary Rocks: Geological Society of London Special Publication 29, p. 91-105.

Whitworth, T. M., Haneberg, W. C., Mozley, P. S., and Goodwin, L. B., 1999, Solute-sieving induced calcite precipitation on pulverized quartz sand: experimental results

and implications for membrane behavior of fault gouge, *in* Haneberg, W. C., Mozley, P. S., Moore, K. C., and Goodwin, L. B., eds., Faults and subsurface fluid flow in the shallow crust: Washington, DC, American Geophysical Union, p. 149-158.

Wilson, E. B., 1952, An introduction to scientific research: New York, McGraw-Hill, 375 p.

Wong, T. -f., David, C., and Zhu, W., 1997, The transition from brittle faulting to cataclastic flow in porous sandstones: Mechanical deformation: Journal of Geophysical Research, v. 102, p. 3009-3025.

Zhang, J., Wong, T. -f., and Davis, D. M., 1990, Micromechanics of pressure-induced grain crushing in porous rocks: Journal of Geophysical Research, v. 95, p. 341-352.

CHAPTER 4. INTERNAL ARCHITECTURE, PERMEABILITY STRUCTURE, AND HYDROLOGIC SIGNIFICANCE OF CONTRASTING FAULT ZONE TYPES*

4.1. Abstract

The Sand Hill fault is a steeply dipping, large-displacement normal fault that cuts poorly lithified Tertiary sediments of the Albuquerque basin, New Mexico, USA. The fault zone does not contain macroscopic fractures; the basic structural element is the deformation band. The fault core is composed of foliated clay flanked by structurally and lithologically heterogeneous mixed zones, in turn flanked by damage zones. Structures present within these fault-zone architectural elements are different from those in brittle faults formed in lithified sedimentary and crystalline rocks which do contain fractures. These differences are reflected in the permeability structure of the Sand Hill fault. Equivalent permeability calculations indicate that large-displacement faults in poorly lithified sediments have little potential to act as vertical-flow conduits and have a much greater effect on horizontal flow than faults with fractures.

---

* Geoffrey C. Rawling, Laurel B. Goodwin, and John L. Wilson, Geology, v. 29, p. 43-46, 2001.

4.2. Introduction

Brittle fault zones in the upper crust exert significant control on subsurface fluid flow. Flow regimes in faulted sedimentary basins are strongly affected by differences in permeability of fault zones relative to their host rocks (Bredehoeft et al., 1992; Haneberg, 1995). Studies in hydrocarbon reservoirs have shown that individual fault zones may seal in some areas and leak in others, as a complex function of host-rock lithology, the deformation mechanisms operative during faulting, and fault zone diagenesis (e.g., Smith, 1980; Yielding et al., 1997). Fault zones are heterogeneous structures that cannot be simply defined as either barriers or conduits for fluid flow in either space or time (Knipe, 1993; Caine et al., 1996).

Consensus has grown among many workers on a simple and widely applicable structural and hydrologic model for faults formed in crystalline and lithified sedimentary rocks (e.g., Chester et al., 1993; Caine et al., 1996; hereafter abbreviated fault with fractures, FWF; cf. Goodwin et al., 1999). The basic structural component is the fracture (a surface across which the rock has broken and lost cohesion), and the model is composed of three architectural elements: (1) the protolith, which is unfaulted, but may contain regional structures; (2) the damage zone, which may contain small faults, fractures, fracture networks, and veins; and (3) the core zone, which is composed of breccia and/or cataclasite, or gouge, in varying states of induration. The core zone is flanked by the damage zone and is the locus of most of the displacement. Various combinations and degrees of development of damage and core zone yield a range of possible fault-zone architectures and permeability structures (Caine et al., 1996).

The growing need for accurate simulation of subsurface fluid-flow regimes requires incorporating at least the bulk hydrologic properties of fault zones into numerical flow models. Many heavily developed aquifers in urban areas in the southwestern United States are in poorly lithified Tertiary sediments that are pervasively cut by normal faults (Mifflin, 1988; Thorn et al., 1993). The purpose of this paper is to contrast the current model of fault-zone architecture and permeability structure, developed for FWFs, with a new model for large-displacement faults in poorly lithified sediments. Our model is based on the Sand Hill fault zone in the Albuquerque basin, New Mexico, USA. The results indicate that large-displacement faults in poorly lithified sediments have less potential to act as vertical-flow conduits and are significant impediments to cross-fault flow over a wider range of scales than FWFs. This difference is in part due to the absence of macroscopic fractures associated with faulted poorly lithified sediments.

4.3. The Sand Hill Fault

The Sand Hill fault, one of the major normal faults bounding the Rio Grande rift, marks the western margin of the Albuquerque basin (Hawley et al., 1995; Figure 29). It is a growth fault juxtaposing synrift sediments of the Pliocene-Pleistocene upper Santa Fe Group against middle Miocene to Oligocene sediments of the lower and middle Santa Fe Group, with displacement increasing from ~10 to ~600 m downdip (Hawley et al., 1995; Heynekamp et al., 1999). The lower Santa Fe Group sediments are dominantly fine-grained sand, with subordinate medium-grained sand, silty sand, and mud. The upper Santa Fe Group sediments include sand, silt, and mud, locally capped by gravel (Heynekamp et al., 1999).

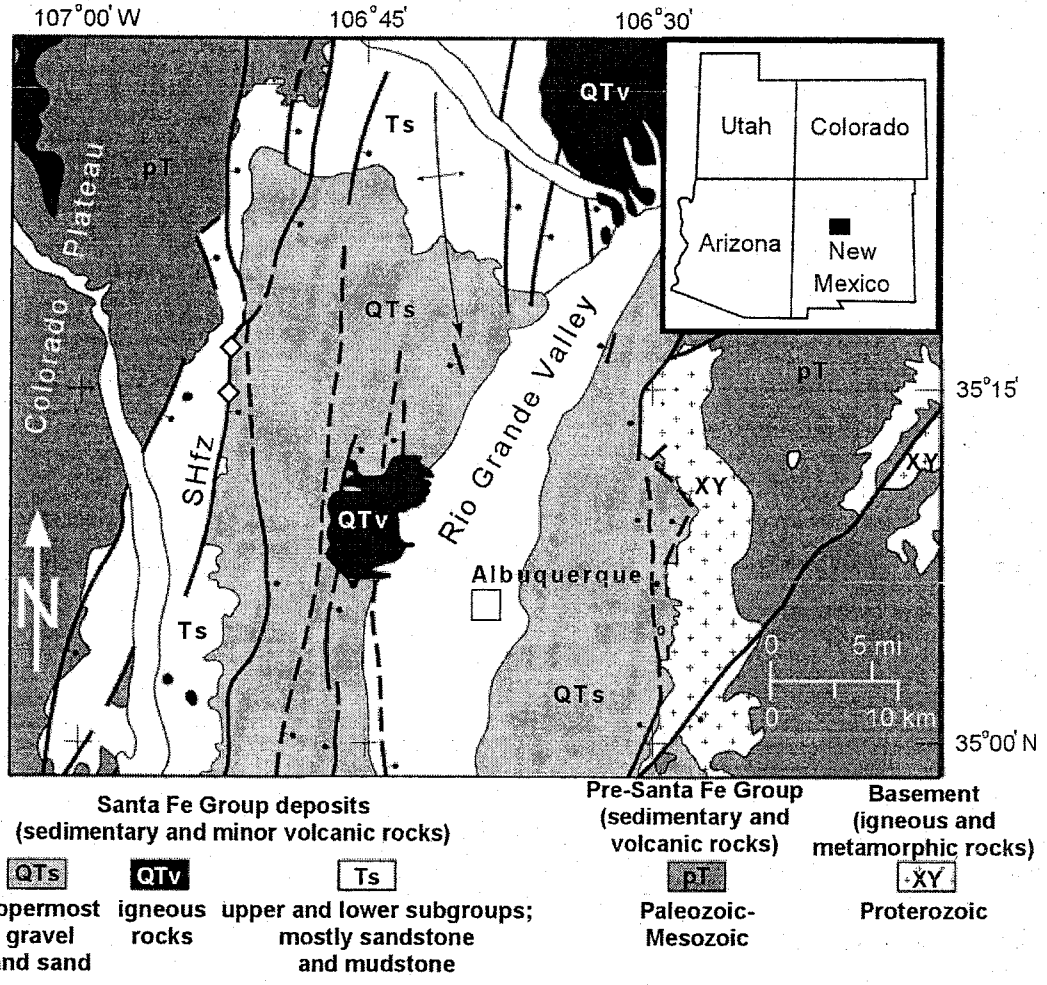

Figure 29. Study sites (open diamonds) along Sand Hill fault zone (SHfz) in Albuquerque basin of Rio Grande rift. Inset shows location. Faults are generalized; not all faults are shown. Modified from Hawley et al. (1995) and Hawley (1996) by S. Connell.

Excepting zones of calcite cementation (Mozley and Goodwin, 1995), all of the materials in the fault zone are friable and easily disaggregated.

Faults in poorly lithified sediments have deformation bands (narrow, tabular zones of displacement, compaction, and/or cataclasis; cf. Aydin, 1978) as the basic structural element and do not contain macroscopic fractures (Heynekamp et al., 1999; Sigda et al., 1999; Figure 30). However, large-displacement "deformation band faults" in poorly lithified sediments (hereafter abbreviated DBF), exemplified by the Sand Hill fault, have two significant differences from faults described previously in high-porosity sandstones (e.g., Aydin, 1978; Underhill and Woodcock, 1987; Antonellini and Aydin, 1995): (1) Where displacement is greater than the local mean bed thickness, a new fault-zone architectural element - the mixed zone - develops between the damage zone and the fault core (Mozley and Goodwin, 1995; Heynekamp et al., 1999; Sigda et al., 1999; Figure 30). The mixed zone includes rotated and attenuated beds and areas where disparate sediment types are mixed at the grain scale by particulate flow during slip. Its grain-size distribution ranges from clay to sand to gravel to virtually any tectonic combination thereof. It is easily identified in the field, and is lithologically, structurally, and hydrologically (Figure 31) distinct from the core and damage zones. Where coarse grained, the basinward hanging-wall mixed zone of the Sand Hill fault is typically cemented with calcite. (2) The fault core is a foliated clay layer as thick as 10 centimeters. Gaps in the clay core are rare, even where the host sediments are dominantly sand (Heynekamp et al., 1999). In contrast, at displacements of >1 m, DBFs in lithified, high-porosity sandstones have a "core" that is a discrete, slickensided slip surface (Antonellini and Aydin, 1995).

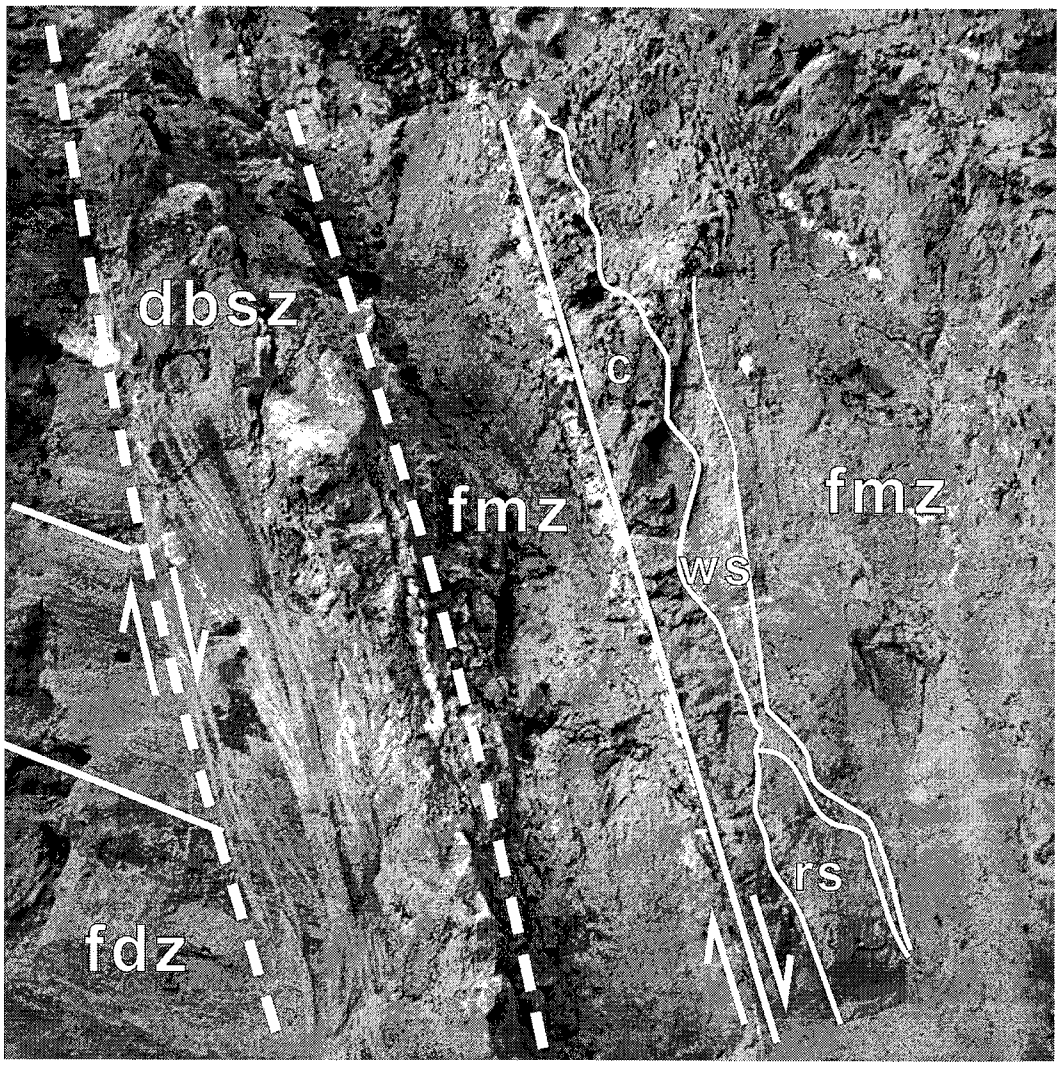

Figure 30. Shear zone of coalesced deformation bands (dbsz, outlined by dashed lines) forming contact between footwall damage zone (fdz) and footwall mixed zone (fmz) within Sand Hill fault zone. Offset is at least several meters. Solid lines delineate tilted bedding in fdz and clay-rich (c), white sand (ws), and red sand (rs) beds transposed into foliation in fmz. Width of photo is 3m.

4.4. Methods

We measured the permeability of poorly lithified sandy to moderately clay-rich (up to 13 wt %) sediments from the damage and mixed zones on three strike-perpendicular outcrops of the Sand Hill fault with a portable air mini-permeameter designed and built at the University of New Hampshire by M. Davis. The permeability of cemented mixed zone sand was measured with the same device on cut surfaces of ~0.25 m^3 samples. The permeability of clay and sandy or silty clay from the footwall mixed zone and fault core was measured in consolidation tests performed on undisturbed water-saturated samples collected with coring tubes from outcrop excavations (cf. Das, 1983). The tests were performed both parallel and perpendicular to bedding and foliation. Values reported are for consolidation pressures of 10 to 18 MPa. These data are presented in Figure 31 and compared with permeability data from the literature for FWFs in crystalline rocks at effective stress conditions of 10 MPa or less.

4.5. Discussion

4.5.1. Permeability Data

The bulk permeability structure of a fault zone is a consequence of the hydrologic properties of the architectural elements, their spatial arrangement, and their setting in the flow system (e.g., Caine and Forster, 1999). Both air mini-permeameter measurements and laboratory tests have sample volumes on the scale of cubic centimeters; as such, both data sets are an incomplete characterization of the macroscale hydrologic properties of the respective architectural elements. As noted by Evans et al. (1997), the data for an FWF damage zone are a lower bound on the bulk permeability of this architectural

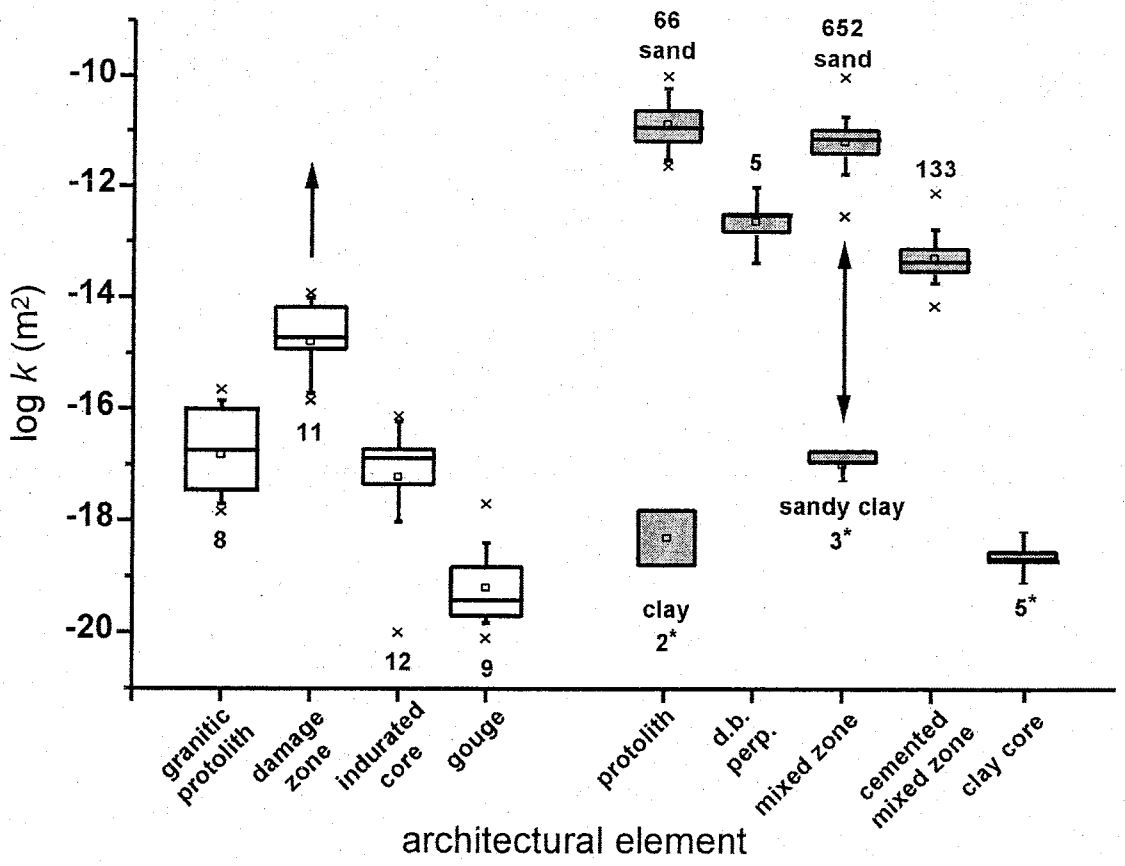

Figure 31. Permeability data for FWFs in crystalline rocks (open boxes) and DBF (grey boxes). Boxes encompass 50% of data; whiskers and x's show extrema; intermediate line is median; small open squares indicate means. Granitic protolith, damage zone, and core data are from Evans et al. (1997); gouge data are from Morrow et al. (1981, 1984). Single-headed arrow indicates that FWF damage zone data are minimum values. Measurements perpendicular to plane of deformation bands (d. b. perp.) from Sigda et al. (1999). Number of measurements is indicated next to each box; stars indicate consolidometer test data; other DBF data are air mini-permeameter measurements. Double-headed arrow indicates that mixed zone permeability varies between end members.

element as the samples do not include the macroscopic fracture networks found in FWFs, which may greatly enhance permeability. Similar scaling considerations apply to DBFs, but are less important because of the lack of fractures.

The hydrologic distinction between FWFs in lithified rocks and DBFs in poorly lithified sediments is clear. Fracture networks enhance permeability in the damage zone of FWFs relative to the protolith and core. The data from the Sand Hill fault indicate that in a poorly lithified DBF, deformational and diagenetic processes and the absence of fractures all reduce permeability in the damage zone, mixed zone, and core relative to a sand-rich protolith, and at best yield a small increase in permeability in the mixed zone relative to a clay-rich protolith (Figure 31).

4.5.2. Bulk Hydrologic Properties

We examine the horizontal and vertical equivalent permeability ratio ($k_{faulted}/k_{unfaulted}$) of a two-dimensional cross-sectional groundwater-flow model grid block containing a fault. Two simple, idealized, end-member fault-protolith systems are considered: an FWF in crystalline rock and a DBF with mixed zones in a two-layer (sand and clay) unlithified sedimentary protolith (Figure 32). For both models, each architectural element is assumed to be internally isotropic and homogeneous, and its permeability is assigned from the data in Figure 31. The damage zone, fault-zone thickness variations, mixed zone heterogeneity, and juxtaposition of different hanging-wall and footwall lithologies are not considered in the unlithified DBF model. The FWF system is treated as a vertically layered medium, in which equivalent permeabilities for horizontal and vertical flow regimes are weighted harmonic and arithmetic means, respectively. Equivalent permeabilities for the faulted poorly lithified sedimentary system

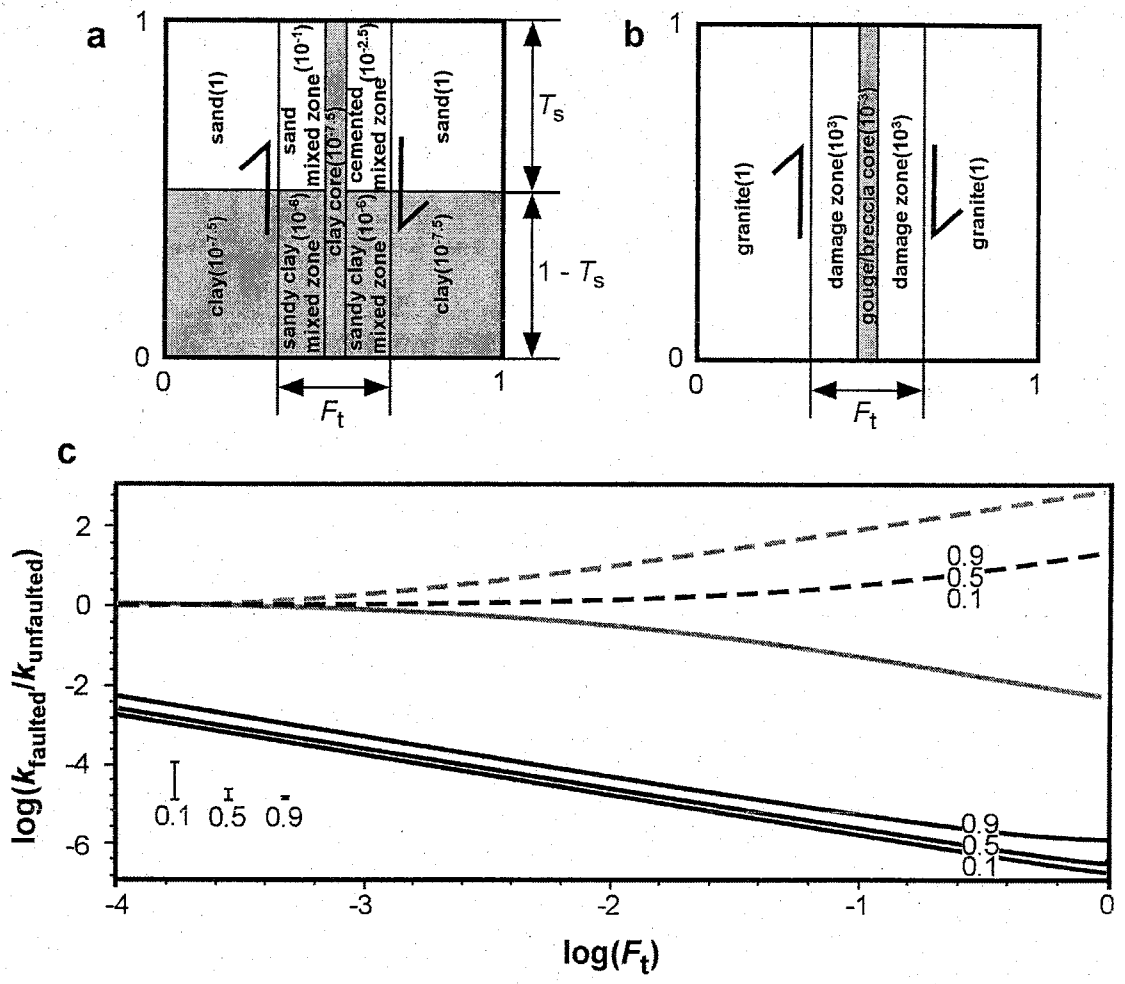

Figure 32. Hydrologic models and results of equivalent permeability calculations. **a)** Schematic illustration of DBF in poorly lithified sediment. Permeabilities (in parentheses) normalized to sand protolith. **b)** Model of FWF in crystalline rock. Permeabilities normalized to granite protolith. In both models, F_t is relative fault-zone width, as a fraction of the horizontal domain width; core width is fixed at $F_t/5$. T_s is relative thickness of sand layer. **c)** Log (equivalent permeability ratio) vs. log (F_t) for DBF model (A, in black) and FWF model (B, in gray). Vertical equivalent permeability ratios are dashed; horizontal ratios are solid. Different T_s values are indicated on DBF model curves; note that vertical curves overlap. Error bars indicate range between maximum and minimum Cardwell-Parsons bounds for case of horizontal flow for different T_s values. These bounds are smaller than curve thickness for vertical-flow case.

are taken as the geometric means of the Cardwell and Parsons' upper and lower bounds for flow in the horizontal and vertical directions (Renard and de Marsily, 1997, p. 257). These bounds are the most general (ibid., p. 271), and given the geologic simplifications and ranges in the permeability data, a more elaborate treatment is not justified.

The permeability trends of Figure 31 are reflected in the differences in the equivalent permeabilities of the two model grid blocks (Figure 32). For typical grid blocks in regional groundwater-flow models, the relative fault zone thickness, expressed as $\log(F_t)$, ranges from about –1.5 to –3 for a 10 m wide fault zone. In this range, the horizontal equivalent permeability of the unlithified DBF system relative to the two-layer undeformed protolith system is reduced as much as four orders of magnitude, with little increase in vertical equivalent permeability (Figure 32). The negligible effect of sand content (T_s) and the large effect of a small percentage of fault in the block (e.g., at $\log(F_t) = -4$) indicate that even a very thin fault with a clay core controls the equivalent permeability of this system. Increased complexity in the model either has minimal effect or will amplify the results (e.g., inclusion of the damage zone or juxtaposition of clay mixed zone against sand protolith). Conversely, over the same range of $\log(F_t)$ values, the FWF system exhibits enhanced vertical permeability and negligible reduction in horizontal permeability at the regional scale.

Several lines of evidence suggest that at shallow (<2 km) depths in extensional systems, increasing effective stress will lower absolute permeability but will not change the relative permeabilities of the architectural elements or the above results: (1) In laboratory tests, permeability in an FWF damage zone remains higher than the protolith and core as effective stress is increased (Evans et al., 1997). In addition, in situ fractures

critically oriented for slip (i.e., those with high resolved shear stresses, the potentially active fractures) are highly permeable conduits at depths as great as 3.5 km (Barton et al., 1995). Thus a large displacement normal FWF in a stress field favoring normal slip would likely be a vertical-flow conduit owing to interconnected arrays of subvertical shear fractures in the damage zone. (2) Permeability of both undeformed sediments and deformed fine-grained sands and muds decreases significantly with increasing effective stress. The decrease is generally greater in finer-grained sediments (Brown et al., 1994; Haneberg et al., 1998). As the clay core dominates the system, this last point suggests that increasing effective stress should further decrease the equivalent permeability ratio for a poorly lithified DBF.

An intermediate case between these two end members is that of a moderate- to large-displacement DBF in lithified, high-porosity sandstone. Deformation bands have significantly reduced permeability compared to their host rocks (e.g., Gibson, 1998), but the discrete slip surfaces act as open shear fractures, lending DBFs in lithified, high-porosity sandstones low fault-normal and potentially very high fault-parallel permeability (Antonellini and Aydin, 1995).

4.6. Conclusions

The internal architecture and lack of macroscopic fractures characteristic of large-displacement faults in poorly lithified sediments are easily identified in the field. The resulting bulk hydrologic properties significantly impede horizontal subsurface fluid flow at a regional scale and do not greatly enhance vertical flow, a condition much different than the conventionally accepted model of fault properties. These faults have significant

potential to compartmentalize both aquifers and hydrocarbon reservoirs resulting in, for example, greater drawdown in production wells. Their low horizontal equivalent permeability suggests representation with a finer flow model grid than would be necessary for faults with fractures. If faulting continues following lithification, pre-lithification structures may be preserved and/or overprinted with fractures. This may result in a fault with properties intermediate between the types discussed here. Depending on consolidation history, this transition may also be expected with increasing depth along a given fault.

4.7. Acknowledgements

Support provided by the National Science Foundation (grant EAR-9706482) and the New Mexico Geological Society. We thank Matt Davis and Christine Bowman for use of their permeameter, Andy Dunn for performing some of the consolidation tests, John Sigda for useful discussions, and Jim Evans and Darrel Cowan for their valuable reviews.

4.8. References Cited

Antonellini, M. A., and Aydin, A., 1995, Effect of faulting on fluid flow in porous sandstones: Geometry and spatial distribution: American Association of Petroleum Geologists Bulletin, v. 79, p. 642-671.

Aydin, A., 1978, Small faults formed as deformation bands in sandstones: Pure and Applied Geophysics, v. 116, p. 913-930.

Barton, C. A., Zoback, M. D., and Moos, D., 1995, Fluid flow along potentially active faults in crystalline rock: Geology, v. 23, p. 683-686.

Bredehoeft, J. D., Belitz, K., and Sharp-Hansen, S., 1992, The hydrodynamics of the Bighorn Basin: A study of the role of faults: American Association of Petroleum Geologists Bulletin, v. 76, p. 530-546.

Brown, K. M., Bekins, B., Clennell, B., Dewhurst, D., and Westbrook, G., 1994, Heterogeneous hydrofracture development and accretionary fault dynamics: Geology, v. 22, p. 259-262.

Caine, J. S., and Forster, C. B., 1999, Fault zone architecture and fluid flow: Insights from field data and numerical modeling, *in* Haneberg, W. C., Mozley, P. S., Moore, K. C., and Goodwin, L. B., eds., Faults and subsurface fluid flow in the shallow crust: Washington, DC, American Geophysical Union, p. 101-127.

Caine, J. S., Evans, J. P., and Forster, C. B., 1996, Fault zone architecture and permeability structure: Geology, v. 24, p. 1025-1028.

Chester, F. M., Evans, J. P., and Biegel, R. L., 1993, Internal structure and weakening mechanisms of the San Andreas Fault: Journal of Geophysical Research, v. 98, p. 771-786.

Das, B.M., 1983, Advanced soil mechanics: Washington, DC, Hemisphere Publishing Corporation, 511 p.

Evans, J. P., Forster, C. B., and Goddard, J. V., 1997, Permeability of fault related rocks, and implications for hydraulic structure of fault zones: Journal of Structural Geology, v. 19, p. 1393-1404.

Gibson, R. G., 1998, Physical character and fluid-flow properties of sandstone-derived fault zones, *in* Coward, M. P., Daltaban, T. S., and Johnson, H., eds., Structural geology in reservoir characterization: London, The Geological Society, p. 83-97.

Goodwin, L. B., Mozley, P. S., Moore, J. C., and Haneberg, W. C., 1999, Introduction, *in* Haneberg, W. C., Mozley, P. S., Moore, K. C., and Goodwin, L. B., eds., Faults and subsurface fluid flow in the shallow crust: Washington, DC, American Geophysical Union, p. 1-5.

Haneberg, W. C., 1995, Steady-state groundwater flow across idealized faults: Water Resources Research, v. 31, p. 1815-1820.

Haneberg, W. C., Gomez, P., Gibson, A., and Allred, B., 1998, Preliminary measurements of stress-dependent hydraulic conductivity of Santa Fe Group aquifer system sediments from the 98th St. core hole, Albuquerque, New Mexico: New Mexico Geology, v. 20, p. 14-20.

Hawley, J. W., 1996, Hydrogeologic framework of potential recharge areas in the Albuquerque basin, central New Mexico: New Mexico Bureau of Mines and Mineral Resources Open-File Report 402 D, Chapter 1, 68 p.

Hawley, J. W., Haase, C. S., and Lozinsky, R. P., 1995, An underground view of the Albuquerque basin, *in*, The Water Future of Albuquerque and the Middle Rio Grande Basin, Proceedings of the 39th Annual New Mexico Water Conference: New Mexico Water Resources Research Institute Report 290, p. 37-55.

Heynekamp, M. R., Goodwin, L. B., Mozley, P. S., and Haneberg, W. C., 1999, Controls on fault-zone architecture in poorly lithified sediments, Rio Grande rift, New Mexico:

Implications for fault-zone permeability and fluid flow, *in* Haneberg, W. C., Mozley, P. S., Moore, K. C., and Goodwin, L. B., eds., Faults and subsurface fluid flow in the shallow crust: Washington, DC, American Geophysical Union, p. 27-49.

Knipe, R. J., 1993, The influence of fault zone processes and diagenesis on fluid flow, *in* Horbury, A. D., and Robinson, A. G., eds., Diagenesis and basin development: Tulsa, OK, American Association of Petroleum Geologists, p. 135-151.

Mifflin, M. D., 1988, Region 5, Great Basin, *in* Back, W., Rosenshein, J. S., and Seaber, P. R., eds., Hydrogeology: Boulder, CO, Geological Society of America, Geology of North America, v. O-2, p. 69-78.

Morrow, C. A., Shi, L. Q., and Byerlee, J. D., 1981, Permeability and strength of San Andreas fault gouge under high pressure: Geophysical Research Letters, v. 8, p. 325-328.

Morrow, C. A., Shi, L. Q., and Byerlee, J. D., 1984, Permeability of fault gouge under confining pressure and shear stress: Journal of Geophysical Research, v. 89, p. 3193-3200.

Mozley, P. S., and Goodwin, L. B., 1995, Patterns of cementation along a Cenozoic normal fault: A record of paleoflow orientations: Geology, v. 23, p. 539-542.

Renard, P., and de Marsily, G., 1997, Calculating equivalent permeability: A review: Advances in Water Resources, v. 20, p. 253-278.

Sigda, J. M., Goodwin, L. B., Mozley, P. S., and Wilson, J. L., 1999, Permeability alteration in small-displacement faults in poorly lithified sediments: Rio Grande rift, central New Mexico, *in* Haneberg, W. C., Mozley, P. S., Moore, K. C., and Goodwin,

L. B., eds., Faults and subsurface fluid flow in the shallow crust: Washington, DC, American Geophysical Union, p. 51-68.

Smith, D. A., 1980, Sealing and non-sealing faults in the Louisiana Gulf Coast salt basin: American Association of Petroleum Geologists Bulletin, v. 64, p. 145-172.

Thorn, C. R., McAda, D. P., and Kernodle, J. M., 1993, Geohydrologic framework and hydrologic conditions in the Albuquerque basin, central New Mexico: U.S. Geological Survey Water Resources Investigations Report 93-4149, 106 p.

Underhill, J. R., and Woodcock, N. H., 1987, Faulting mechanisms in high-porosity sandstones; New Red Sandstone, Arran, Scotland, *in* Jones, M. E., and Preston, R. M. F., eds., Deformation of Sediments and Sedimentary Rocks: Geological Society of London Special Publication 29, p. 91-105.

Yielding, G., Freeman, B., and Needham, D. T., 1997, Quantitative fault seal prediction: American Association of Petroleum Geologists Bulletin, v. 81, p. 897-917.

CHAPTER 5. NUMERICAL MODELLING OF FLUID FLOW PATTERNS ADJACENT TO CONTRASTING FAULT-ZONE TYPES

5.1. Abstract

I have investigated subsurface fluid flow patterns adjacent to two types of steeply dipping faults with contrasting internal architecture using two-dimensional finite element flow models. Representation of faults as simple planes of offset that juxtapose strata is a geologic oversimplification, as the fault-related fluid flow patterns are not consistent with field data. Fluid flow in faults with fractures in lithified sedimentary rocks is concentrated in fracture-rich damage zones, which allow extensive vertical redistribution of flow. Faults with mixed zones in poorly lithified sediments are more effective barriers to horizontal flow. Flow is induced in low permeability layers adjacent to such faults, and there is less potential for vertical distribution, or focussing, of flow within the fault zone. Increasing internal fault zone complexity and varying the thickness of the host strata have only secondary effects on flow patterns for both fault types. Three-part fault zone models of core and bounding damage or mixed zones therefore appear adequate for simulation of fluid-flow patterns in numerical models.

5.1. Introduction

It is well known that fault zones in the upper crust can act as both conduits for, and barriers to, subsurface fluid flow and influence local and regional groundwater flow patterns (Bredehoeft et al., 1992; Kolm and Downey, 1994; Haneberg, 1995) and the migration patterns and occurrence of hydrocarbons (Hooper, 1991; Knipe, 1993). Developing an understanding of the effects of fault zones on subsurface fluid flow requires field characterization of fault zone geology, extensive permeability measurements, and integration of these data into fault zone models such that they may be applied to solve geologic and hydrologic problems. Several previous studies have addressed these issues for faults in crystalline and lithified sedimentary rocks, in which the basic structural component is the fracture (e.g., Forster and Evans, 1991; Antonellini and Aydin, 1994; Antonellini and Aydin, 1995; Caine et al., 1996; Evans et al., 1997; Caine and Forster, 1999). However, many heavily developed aquifers in the southwestern United States are in poorly lithified Tertiary sediments that are pervasively cut by normal faults (Anderson et al., 1988; Thorn et al., 1993; Kernodle, 1998). The previous chapters of this dissertation have shown that the internal architecture, operative deformation mechanisms, and hydrologic properties of these faults differ greatly from faults in crystalline and lithified sedimentary rocks. Faults in poorly lithified sandy sediments have deformation bands as their basic structural element. In Chapter 3, I showed via equivalent permeability calculations that when considered at the basin scale, large-displacement faults in poorly lithified sediments are not likely to be vertical flow conduits and have great potential to be barriers to horizontal flow. This is in distinct contrast to faults in crystalline and lithified sedimentary rocks, which are likely to be

vertical flow conduits and less significant barriers to horizontal flow. At the basin scale, the volume of the fault is small compared to the volume of the study domain, and many of the details of fault zone internal architecture can be neglected.

Matthai and Roberts (1996) used numerical flow models to study the effect of faults on fluid flow patterns within faulted sandstone and shale sequences. They studied the effect of juxtaposition alone, and that of faults that had low and high permeability relative to the host sandstones. Their models had vertical no-flow boundaries and a vertical applied fluid pressure gradient. In the case of juxtaposition alone (the fault having no properties of its own), flow was focussed at points where highly permeable sands overlapped. When the fault had a lower permeability than any of the host rocks, it was a barrier to flow, with offsets in fluid pressure isobars in the sediments on either side of the fault. In this case, even the most impermeable shales had a significant component of flow. In contrast, when the fault had higher permeability than its host rocks, it was a conduit for flow.

However, many questions remain in regard to the effect of faults on local fluid flow patterns beyond those considered by Matthai and Roberts (1996). What are the effects of fault zone structural complexity and its associated permeability heterogeneity? More specifically, what are the different effects on fluid flow patterns of faults with fractures vs. faults with deformation bands, similar to the Sand Hill fault? How are cross-fault fluid-flow patterns influenced by fault zone geology? How is fluid flow influenced by the thickness of the host sedimentary strata relative to fault zone thickness?

In this study, I first compare the results of Chapter 4 with net flux calculations for idealized models of faults in poorly lithified sediments and faults with fractures in

crystalline rocks. The model domains are identical to those for which equivalent permeability calculations were performed in Chapter 4. The reductions in flux across the model domains due to the imposition of the fault zones correlate well with the reductions in equivalent permeability shown in Chapter 4, and provide and independent confirmation of the conclusions of that chapter. They also bolster the conclusions of the second set of models.

Secondly, I use two-dimensional, cross-sectional numerical models of steady-state fluid flow in faulted sedimentary sequences to investigate the questions posed above. Net horizontal rather than vertical flow is considered, as this is more relevant to groundwater flow in the sedimentary basin aquifers of the southwestern U.S. (e.g. Shafike and Flanigan, 1999) than the vertical flow studied by Matthai and Roberts (1996). Juxtaposition of strata alone is taken as a baseline condition with which to compare the results of models with faults. Two idealized fault zone types are considered: (1) a fault with fractures in lithified sedimentary rocks, which has a low permeability core and high permeability damage zones. This hydrologic/structural architecture can represent a large displacement fault with well-developed core and damage zones, such as the Moab fault (Foxford et al., 1998), or a smaller displacement fault composed of clustered deformation bands and a discrete slip surface (Aydin and Johnson, 1978); and (2), a fault with low permeability core and mixed zones, representing a fault in poorly lithified sediments with displacement greater than local average bed thickness, such as the Sand Hill fault (Heynekamp et al., 1999, Chapter 4). The sediments under consideration in this study are weak enough to be excavated by hand, but strong enough to form vertical cliffs.

crystalline rocks. The model domains are identical to those for which equivalent permeability calculations were performed in Chapter 4. The reductions in flux across the model domains due to the imposition of the fault zones correlate well with the reductions in equivalent permeability shown in Chapter 4, and provide and independent confirmation of the conclusions of that chapter. They also bolster the conclusions of the second set of models.

Secondly, I use two-dimensional, cross-sectional numerical models of steady-state fluid flow in faulted sedimentary sequences to investigate the questions posed above. Net horizontal rather than vertical flow is considered, as this is more relevant to groundwater flow in the sedimentary basin aquifers of the southwestern U.S. (e.g. Shafike and Flanigan, 1999) than the vertical flow studied by Matthai and Roberts (1996). Juxtaposition of strata alone is taken as a baseline condition with which to compare the results of models with faults. Two idealized fault zone types are considered: (1) a fault with fractures in lithified sedimentary rocks, which has a low permeability core and high permeability damage zones. This hydrologic/structural architecture can represent a large displacement fault with well-developed core and damage zones, such as the Moab fault (Foxford et al., 1998), or a smaller displacement fault composed of clustered deformation bands and a discrete slip surface (Aydin and Johnson, 1978); and (2), a fault with low permeability core and mixed zones, representing a fault in poorly lithified sediments with displacement greater than local average bed thickness, such as the Sand Hill fault (Heynekamp et al., 1999, Chapter 4). The sediments under consideration in this study are weak enough to be excavated by hand, but strong enough to form vertical cliffs.

The main conclusions of the numerical flow models are that juxtaposition alone is too much of a geologic oversimplification to realistically simulate fluid flow patterns around and across faults. However, relatively simple, three-part fault zones with representative permeability values based on laboratory and field data are sufficient to simulate the complex flow patterns around both types of fault zone. Additional fault zone complexity does not significantly change the basics of the flow patterns, nor does varying the thicknesses of the host sedimentary strata. The model results are in agreement with equivalent permeability calculations for similar idealized fault zone models (Chapter 4), and should provide useful constraints on incorporating fault zones into basin-scale groundwater flow models.

5.2. Descriptions of the Models

5.2.1. Net Flux Calculations

In Chapter 4, I compared the equivalent permeability of faulted poorly lithified sediments and faulted granite to their unfaulted protoliths to assess the impact of different fault zone types on regional groundwater flow. The calculations were presented as the equivalent permeability ratio ($k_{faulted}/k_{unfaulted}$) as a function of the normalized fault zone thickness ($\log(F_t)$; see Figure 32). Here, using identical model geometries and hydrologic properties, I calculated the steady-state head distribution and derived total flux across the model domains using the finite element method. Derived fluxes were normalized by the flux across unfaulted model domains so the results could be directly compared to those of Chapter 4.

5.2.2. Models of Faulted Sedimentary Sequences

I investigated the influence of fault permeability on fluid-flow patterns with cross-sectional finite element models of faulted, sand, silt, and clay (fining-upward) sedimentary sequences. Where present, the fault zone is 1m wide, and embedded in sedimentary sequences that are 40 m wide and 12.5 m high, for a length/height ratio of ~3.2:1. To assess the effect of boundary conditions on fluid flow patterns in the vicinity of the fault, additional model calculations with a length/height ratio of 6:1 were performed, but the results were not significantly different. The left and right model boundaries have prescribed heads (Dirichlet boundary conditions) of 1 m on the left and 0.9 m on the right. This results in flow from left to right and an imposed head gradient of ~ .0025 across the model domain. The top and bottom model boundaries are no-flow boundaries (Neumann boundary conditions). The models are for steady-state flow conditions; thus the results may not be applicable to transient flow problems, such as the flow patterns around a pumping well near a fault. However, the results should be directly applicable to patterns of flow over geologic time scales or flow in basins without significant nearby pumping stresses.

Permeabilities in all model units are normalized to the poorly lithified sand or sandstone protolith, respectively, and are presented in Table 3. The permeability values for the protolith units are typical of the ranges of permeability for poorly lithified sediments adjacent to the Sand Hill fault (Chapter 4) and for lithified sedimentary rocks (Domenico and Schwartz, 1990), and were chosen to give a wide range in host rock permeabilities in the models. The permeability values for the fault zone architectural elements are from the ranges of permeability data in Chapter 4,

Table 3. Relative permeabilities of flow model components.

Model component	**Relative permeability**	
Sedimentary layer	Poorly lithified sediment	Sedimentary rock
Sand layer (sandstone)	1	1
Silt layer (siltstone)	$1x10^{-3}$	$1x10^{-4}$
Clay layer (mudstone)	$1x10^{-6}$	$1x10^{-6}$
Fault zone element		
Sand mixed zone *	$1x10^{-3}$	-
Silt mixed zone	$1x10^{-4}$	-
Clay mixed zone	$1x10^{-6}$	-
Sand damage zone†	-	$1x10^{3}$
Silt damage zone	-	$1x10^{-1}$
Clay damage zone	-	$1x10^{-6}$
Clay core/gouge zone	$1x10^{-6}$	$1x10^{-6}$

* also permeability of entire mixed zone in simple fault model.
† also permeability of entire damage zone in simple fault model.

Antonellini and Aydin (1994), Antonellini and Aydin (1995), and Evans et al. (1997). For simplicity, each model component has a homogenous and isotropic distribution of permeability.

5.2.3. Model 1 - Juxtaposition

In model 1, the fault zone has no properties of its own and is a plane across which the strata have moved relative to one another (Figure 33). This allows the effects of juxtaposition on fluid flow to be examined in isolation. In this model and models 2 and 3, the juxtaposition of the layers is perfect, i.e., the offset on the fault is great enough so that no layer overlaps, or is still connected to, its companion on the opposite side of the fault.

5.2.4. Model 2 – Simple Fault Zone

In model 2, the fault zone is subdivided into three architectural elements, the nature of which depend on whether the host strata are lithified or not (Figure 34). The architectural elements are internally homogenous throughout the extent of the fault and their permeabilities do not depend on the adjacent host strata. In the poorly lithified sediment case, analogous to the Sand Hill fault, the fault zone has a central core flanked by mixed zones. The damage zone is ignored, as I infer that it have minimal effect on the fluid flow patterns due to its low density of deformation-related structures. In the sedimentary rock models, the fault zone consists of a central gouge or cataclasite zone flanked by damage zones.

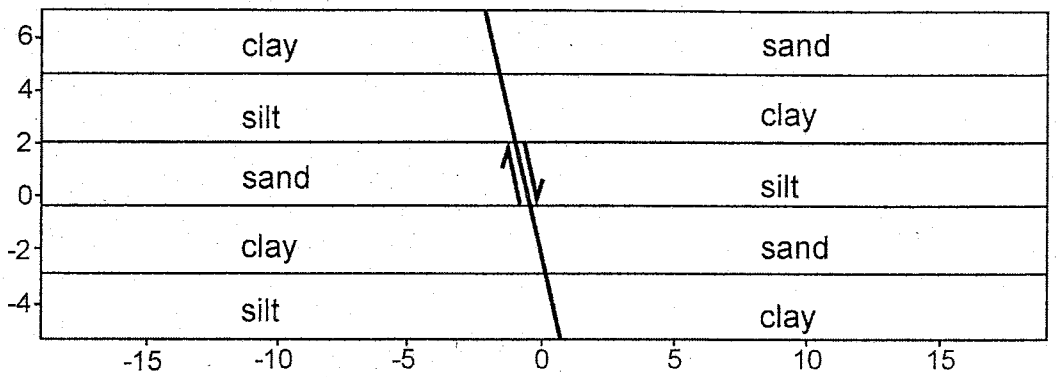

Figure 33. Model 1 (juxtaposition-only) domain. Dimensions are in m; no vertical exaggeration. Flow is from left to right.

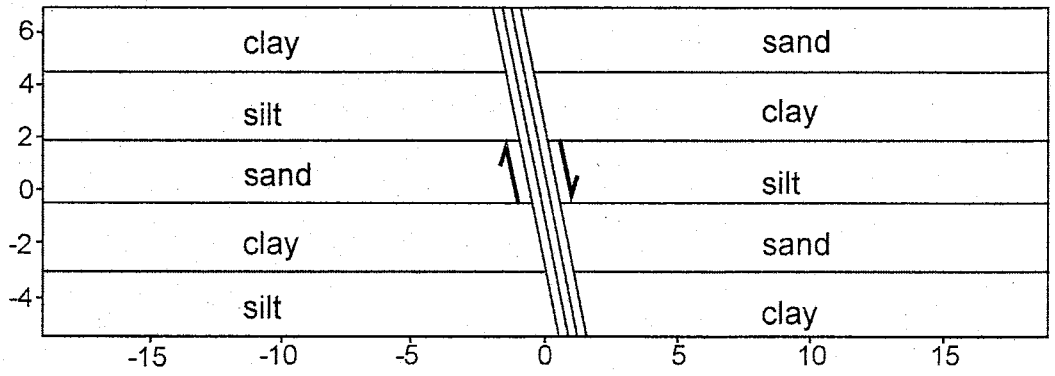

Figure 34. Model 2 (simple fault) domain. Fault consists of a core flanked by damage zones (lithified sedimentary rock model) or mixed zones (poorly lithified sediment model). Dimensions are in m; no vertical exaggeration. Flow is from left to right.

5.2.5. Model 3 – Subdivided Fault Zone

In model 3, the faults zones are composed of three architectural elements as in model 2. However, the mixed zones in the poorly lithified sediment model and the damage zones in the sedimentary rock model are subdivided (Figure 35), and their permeabilities are assigned based on the adjacent host strata (Table 3). This is a first step towards assessing the effects of the material heterogeneity present in true fault zones.

5.2.6. Model 4 – Varied Sedimentary Thickness

In the previous three models, the sedimentary strata are all of equal thickness. In model 4, the fault zones are subdivided as in model 3, but the thickness of the sedimentary strata is variable (Figure 36). The thickness of the silt layer is increased, and the thickness of the clay layer is decreased, whereas the thickness of the sand layers is roughly the same. This is a somewhat more realistic depiction of fluvial sedimentary sequences, with channel sands interbedded with finer-grained overbank silts and clays. This sequence is analogous to the sedimentary section exposed in the footwall of the Sand Hill fault at the Waterfall site (Chapter 2).

5.3. Model Computations

The finite element calculations for all of the models in this chapter were carried out using the Partial Differential Equation Toolbox in the MATLAB software package. The finite element mesh generation algorithm was constrained so that the width and/or thickness of all model components corresponded to at least two triangular finite elements. Adaptive mesh generation was used to achieve a higher density of elements in areas of

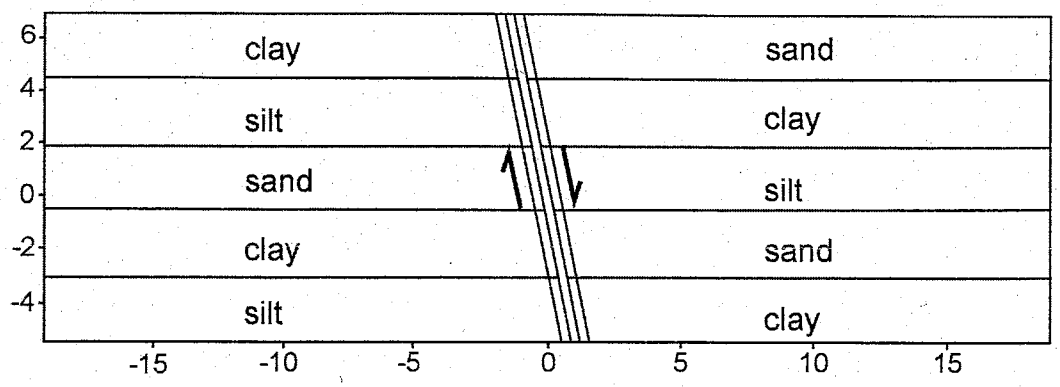

Figure 35. Model 3 (subdivided fault) domain. Fault consists of a core flanked by damage zones (lithified sedimentary rock model) or mixed zones (poorly lithified sediment model), which are internally subdivided, with properties dependent on the adjacent rock or sediment. Dimensions are in m; no vertical exaggeration. Flow is from left to right.

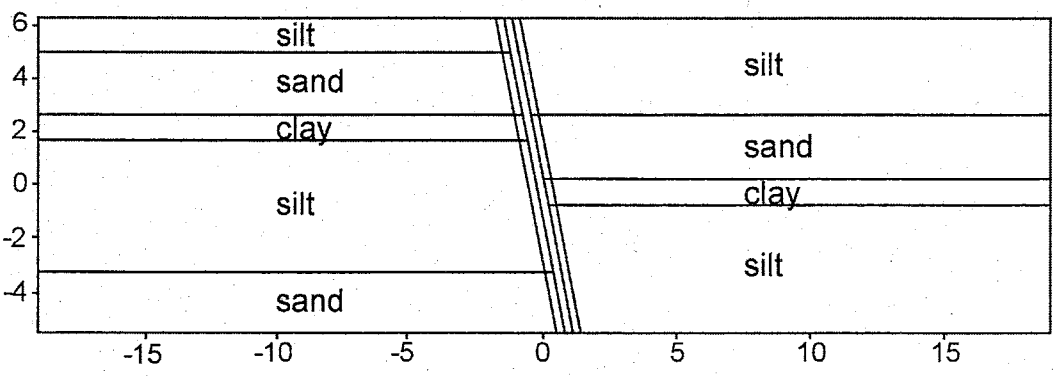

Figure 36. Model 4 (varied sedimentary thickness) domain. Fault consists of a core flanked by damage zones (lithified sedimentary rock model) or mixed zones (poorly lithified sediment model), which are internally subdivided, with properties dependent on the adjacent rock or sediment. Dimensions are in m; no vertical exaggeration. Flow is from left to right.

high head gradients. For the second set of models, the calculated head distribution was interpolated to a regular (0.1m x 0.1 m) rectangular grid over the model domain for plotting purposes. The results are presented as scalar specific discharge fields over the entire model domain and specific discharge vector fields over the region in the vicinity of the fault. The chosen rectangular grid spacing is the best compromise between showing the intricacies of the flow pattern and cluttering the vector plots with too many vectors. The interpolation of the triangular finite element mesh to a rectangular grid results in stepped and occasionally irregular model component boundaries in the scalar specific discharge fields.

The specific discharge vectors are plotted with their tails at the center of the rectangular grid blocks. Different scaling factors were used on the vector field plots to make the vectors visible across a given plot while keeping them from overlapping. These scaling factors are noted in the figure captions. The use of these scaling factors mean that the magnitudes (lengths) of the vectors are not directly comparable between some of the plots.

Note that because of the normalization of the permeability values and the arbitrary choice of head gradient, the absolute magnitude of the calculated specific discharge, either in the scalar fields or in the vector plots, is somewhat arbitrary. As long as the permeabilities chosen in any one model have the same relative values, the imposed head gradient is merely a scaling factor. In other words, it will not change the relative lengths of the specific discharge vectors or their pattern, which are our primary concern in this study.

5.4. Results

5.4.1. Net Flux Calculations

The results of the net flux calculations are presented in Table 4. For each model, the net horizontal and vertical fluxes across the model domain are normalized by the fluxes across the equivalent unfaulted domain. It can be seen that, for each model, the flux ratios are very similar to the equivalent permeability ratios of Chapter 4, for both values of fault zone thickness used. Thus, the finite element flow models support the conclusions drawn from the somewhat simpler equivalent permeability calculations of Chapter 4. The consistency of the results from the two methods also lends credence to the results of the models discussed below.

5.4.2. Model 1 - Juxtaposition

In model 1, the strata are offset across a fault with no intrinsic properties (Figure 33). Figure 37a shows the scalar specific discharge field for the unlithified sediment case. Much of the flux across the model is within the sand layers, and the across the fault is concentrated at the tips of the sand layers. This is clearly shown in Figure 37b, in which the specific discharge vectors smoothly increase in magnitude and rotate towards the constriction point across the juxtaposition plane. There is no increase in flow in any of the other units in the vicinity of the fault or near the sand-sand juxtaposition point, nor is there any flow up or down the plane of juxtaposition beyond the sand or sandstone layers.

5.4.2. Model 2 - Simple Fault Zone

Fault in Poorly Lithified Sediments. In this model, the fault has three orders of magnitude permeability reduction in the mixed zones and six orders of magnitude

Table 4. Results of net flux calculations.

Faulted poorly lithified sediment model			
Flow direction*	**log (fault zone thickness†)**	**log (flux ratio‡)**	**log (equivalent permeability ratio§)**
Horizontal	-1	-5.7	-5.6
Horizontal	-2	-4.8	-4.9
Vertical	-1	0.6	0.5
Vertical	-2	0.1	0.08
Faulted granite model			
Flow direction	**log (fault zone thickness)**	**log (flux ratio)**	**log (equivalent Permeability ratio)**
Horizontal	-1	-1.3	-1.3
Horizontal	-2	-0.5	-0.5
Vertical	-1	1.9	1.9
Vertical	-2	1.0	1.0

* horizontal = cross-fault; vertical = fault-parallel.
† relative fault zone width, as a fraction of the horizontal domain width.
‡ net flux across faulted model divided by net flux across unfaulted model (no fault present).
§ equivalent permeability ratio from Chapter Four; see Figure 32.

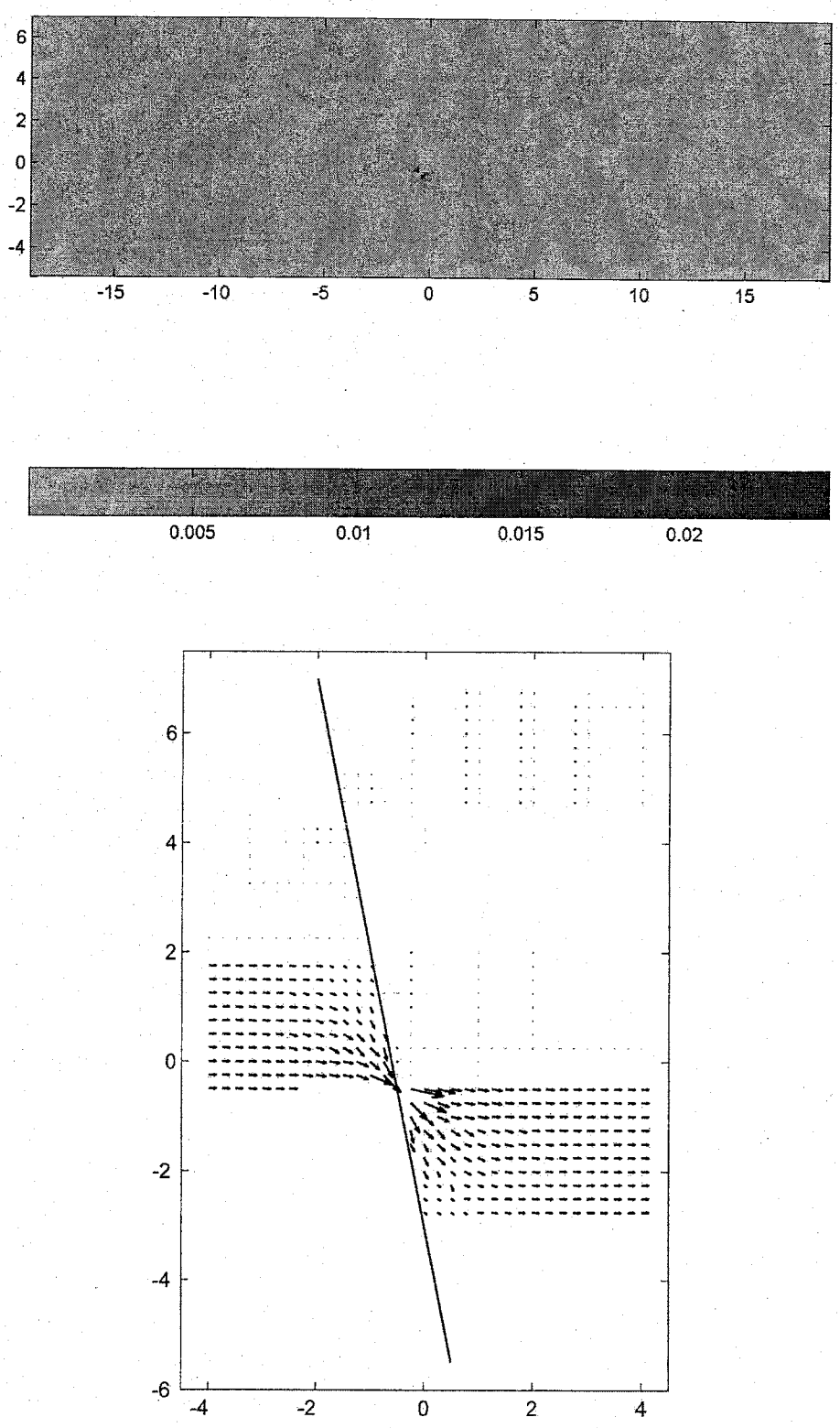

Figure 37. Results for model 1 (juxtaposition only). **a)** (top) Scalar specific discharge field. **b)** (bottom) Specific discharge vectors (length exaggerated 2x) for the region adjacent to the fault. Black line is the fault plane.

permeability reduction in the core, compared to the host sand (Table 3 and Figure 34), and so is a barrier to net horizontal flow (cf., Chapter 4). This is shown in Figure 38a by the greatly reduced flux across the entire model domain (compare the color scales of Figures 37a and 38a). This reduction of flux holds for all of the models with a fault present, as they all have low permeability cores. Flow arrives at the fault from the left, focussed primarily in the sand layer, with a minor amount in the lower silt layer. It crosses the fault and exits to the right, again primarily in the high permeability sand layers (Figure 38a). The flow patterns around the fault are much more complex than in the case of juxtaposition alone. Figure 38b shows that within a meter of the fault, flow increases in the silt layer above the sand, and deviates from horizontal in the sand and silt. Flow in the sand layer diverges at the fault, and the fluid is distributed up and down the mixed zone. This pattern is common to all of the poorly lithified sediment models and occurs because of the low permeability of the mixed zone and core – flow cannot be focussed across these units, but rather is distributed up and down the mixed zone so it can flow across the entire core. Note that the specific discharge vectors across the core have approximately the same magnitude and direction along the dip of the fault. After crossing the core, flow is again distributed up and down the mixed zone back to the high permeability sand layers. Specific discharges are largest in the mixed zone where it bypasses clay layers. The hanging wall silt collects some flow from the fault and the specific discharge vectors in this layer show that this flow is diverted back to the sand layer within two meters of the fault.

Fault with Fractures in Sandstone. In this model, the fault has three orders of magnitude permeability increase in the damage zones and six orders of magnitude

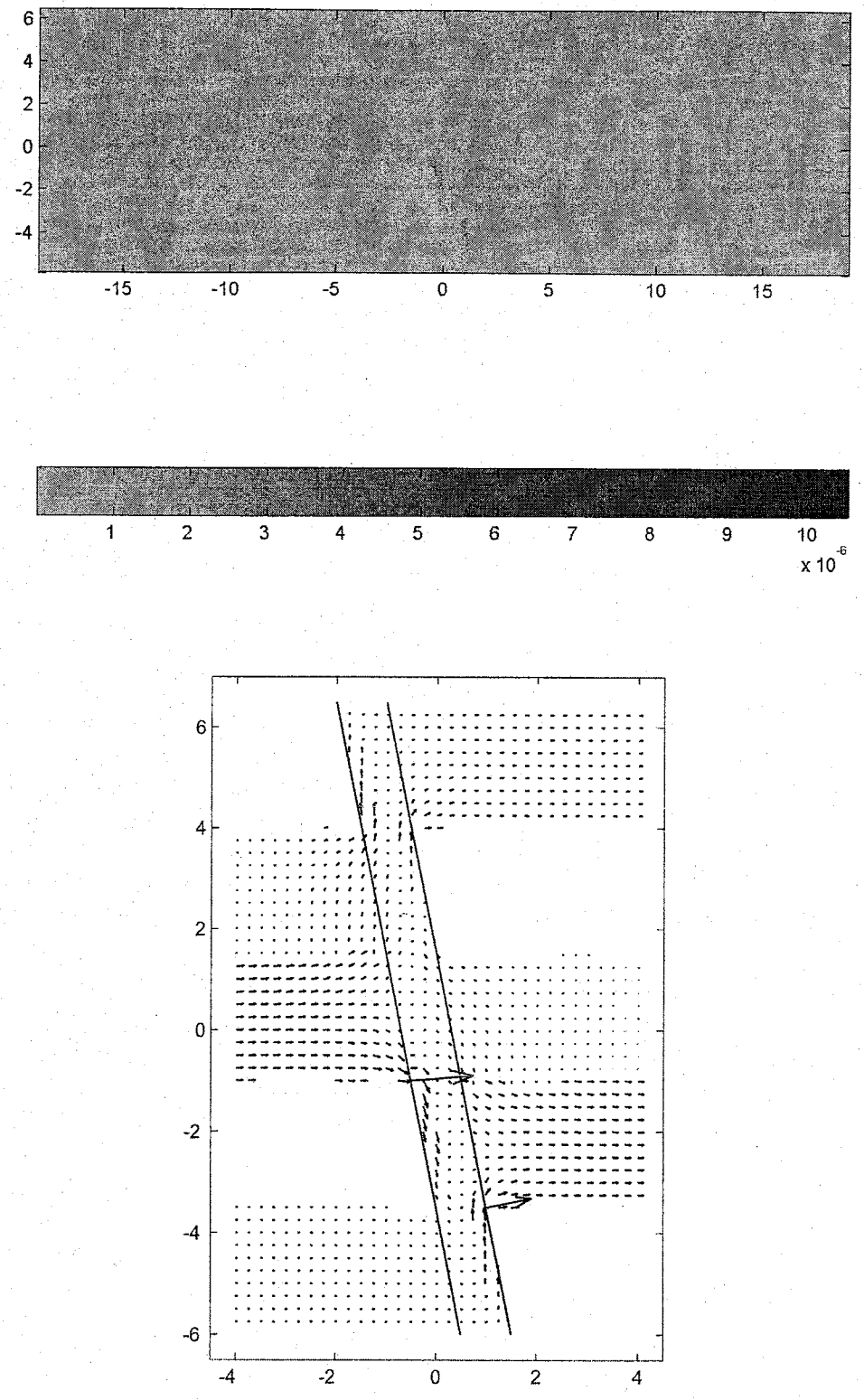

Figure 38. Results for model 2 (simple fault), poorly lithified sediment case. **a)** (top) Scalar specific discharge field. **b)** (bottom) Specific discharge vectors (length exaggerated 4x) for the region adjacent to the fault. Black lines bound the fault zone.

permeability reduction in the core, compared to the host sandstone (Table 3 and Figure 34). Flow again arrives at the fault from the left, primarily in the sand layers. However, there is no additional flow in the silt layer, unlike the previous model (Figure 39a). The specific discharge vectors away from the fault indicate that little flow is entering the fault from the other footwall units (Figure 39b). Flow is again distributed evenly across the low-permeability core.

After crossing the core, flow is effectively distributed to the high-permeability hanging-wall sandstones by the fractured hanging wall damage zone (Figure 39b). Unlike the previous model, there is no flow in the siltstone layer proximal to the fault.

5.4.3. Model 3 - Subdivided Fault Zone

Fault in Poorly Lithified Sediments. In this model, the mixed zone of the fault is subdivided into different components whose permeability depends on the adjacent sediment (Table 3 and Figure 35). Relative to the adjacent sediment, the sand mixed zone has a large reduction in permeability, whereas the silt mixed zone is slightly reduced, and the clay mixed zone permeability is identical to the host sediment. This reflects the likelihood that tectonic mixing is likely to strongly reduce the permeability of originally sand-rich (and thus very permeable) sediments (Chapter 4).

Flow into the fault is predominantly in the sand layer, and exits largely in the sand layers as well (Figure 40a). However, comparison of Figures 38b and 40b shows that, in the subdivided fault model, relatively more flow exits the fault in the lower sand layer than in the simple fault model. This is because in the subdivided fault model, the low permeability clay and silt mixed zone segments are barriers to flow, and so little flow crosses these units to reach the upper sand layer. Instead, as can be seen in the middle of

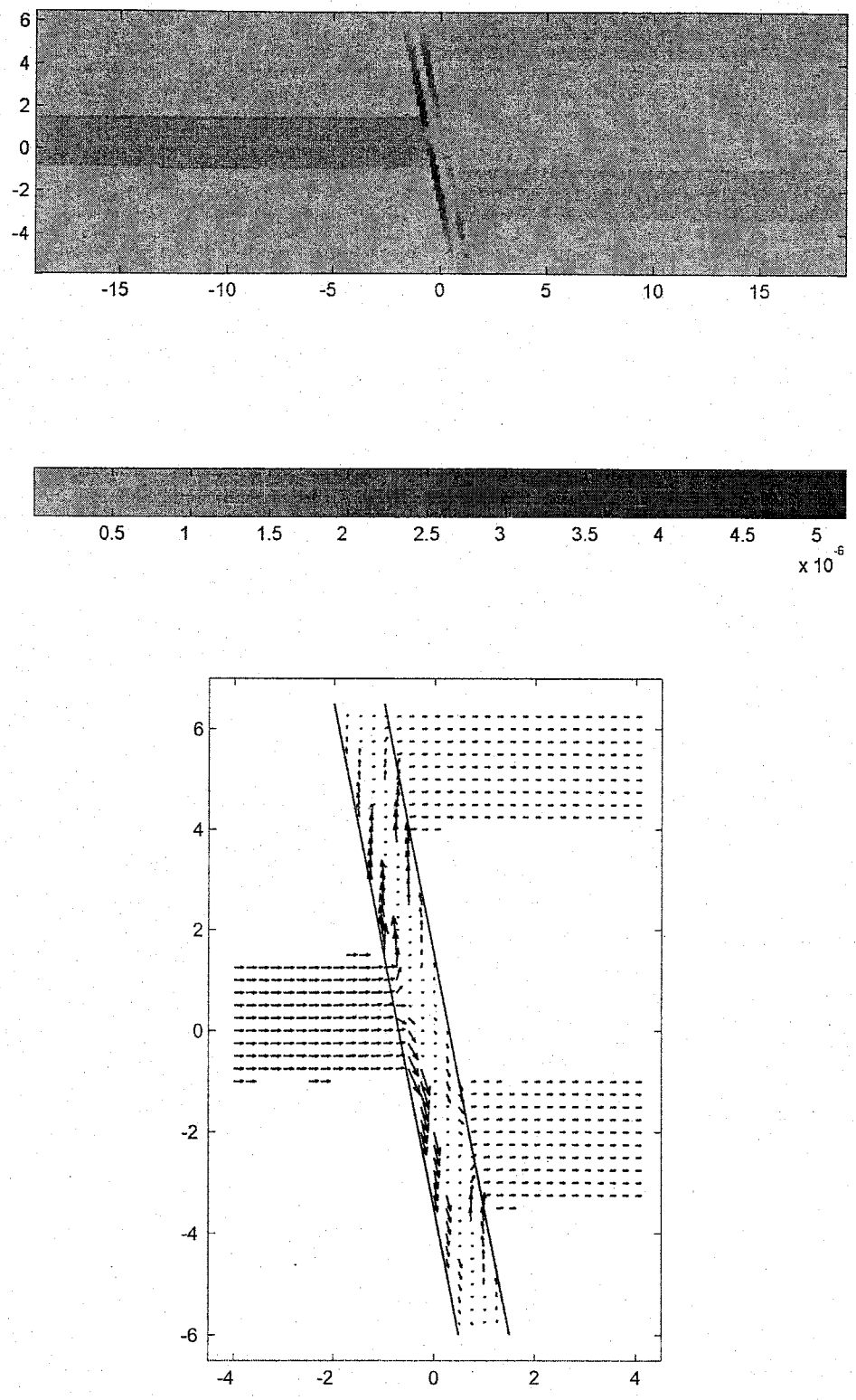

Figure 39. Results for model 2 (simple fault), lithified sedimentary rock case. **a)** (top) Scalar specific discharge field. **b)** (bottom) Specific discharge vectors (length exaggerated) for the region adjacent to the fault. Black lines bound the fault zone.

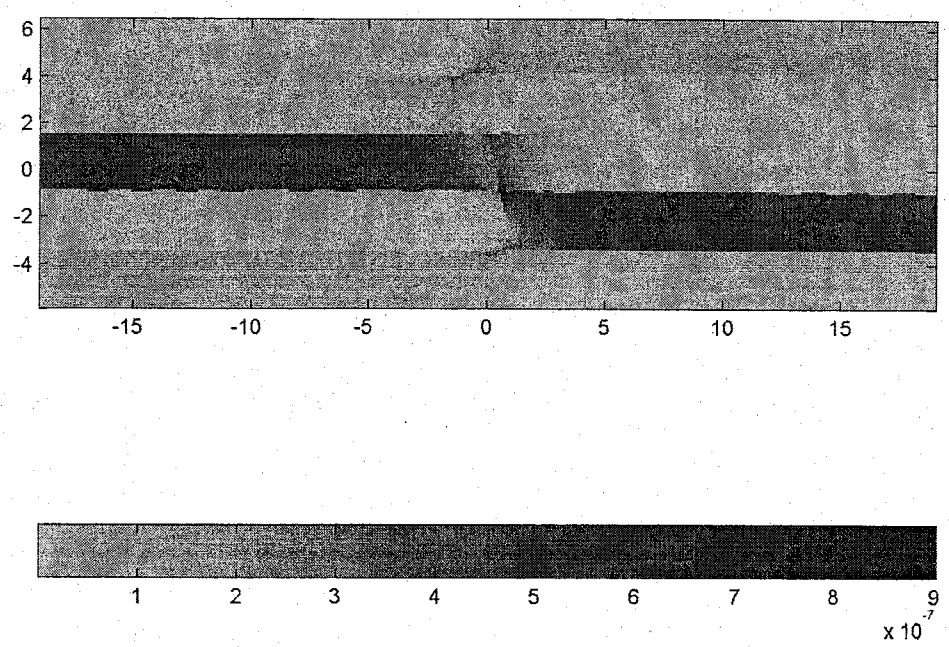

Figure 40. Results for model 3 (subdivided fault), poorly lithified sediment case. **a)** (top) Scalar specific discharge field. **b)** (bottom) Specific discharge vectors (length exaggerated 2x) for the region adjacent to the fault. Black lines bound the fault zone.

Figure 40b, much of the flow in the left-hand sand layer immediately crosses the clay core and enters the lower, right-hand sand layer through the silt mixed zone and strata. This flow in the hanging wall silt layer has all been diverted back into the lower hanging wall sand layer within approximately 4 m of the fault.

In addition, note that flow in the silt layers is focussed at their corners and is highly localized as it crosses the fault into the sand layers. In general the flow across the core is much more irregular than in the previous model, and the mixed zone no longer effectively distributes flow up and down the fault zone.

Fault with Fractures in Sandstone. Again, in this model the damage zone of the fault is subdivided into different components whose permeability depends on the adjacent sediment (Table 3 and Figure 35). The sandstone and siltstone damage zones retain high permeability due to their concentration of fractures. Permeability in claystone damage zones is unchanged, representing development of clay injections or smears.

A main observation of the subdivided poorly lithified sediment model holds true in this case as well: the subdivided mixed zone is no longer as effective at distributing flow up and down the fault zone, and flow across the core is more localized (Figure 41b). Also, when compared to the simple fault model, there is more flow exiting the fault in the lower sand layer than the upper (compare Figures 40 and 41). However, unlike the poorly lithified sediment model, there is little flow outside the fault and the sand layers – where the high permeability damage zones exist, they channel all of the flow away from the footwall sandstone and into the hanging-wall sandstone, resulting in locally high specific discharge in the fault.

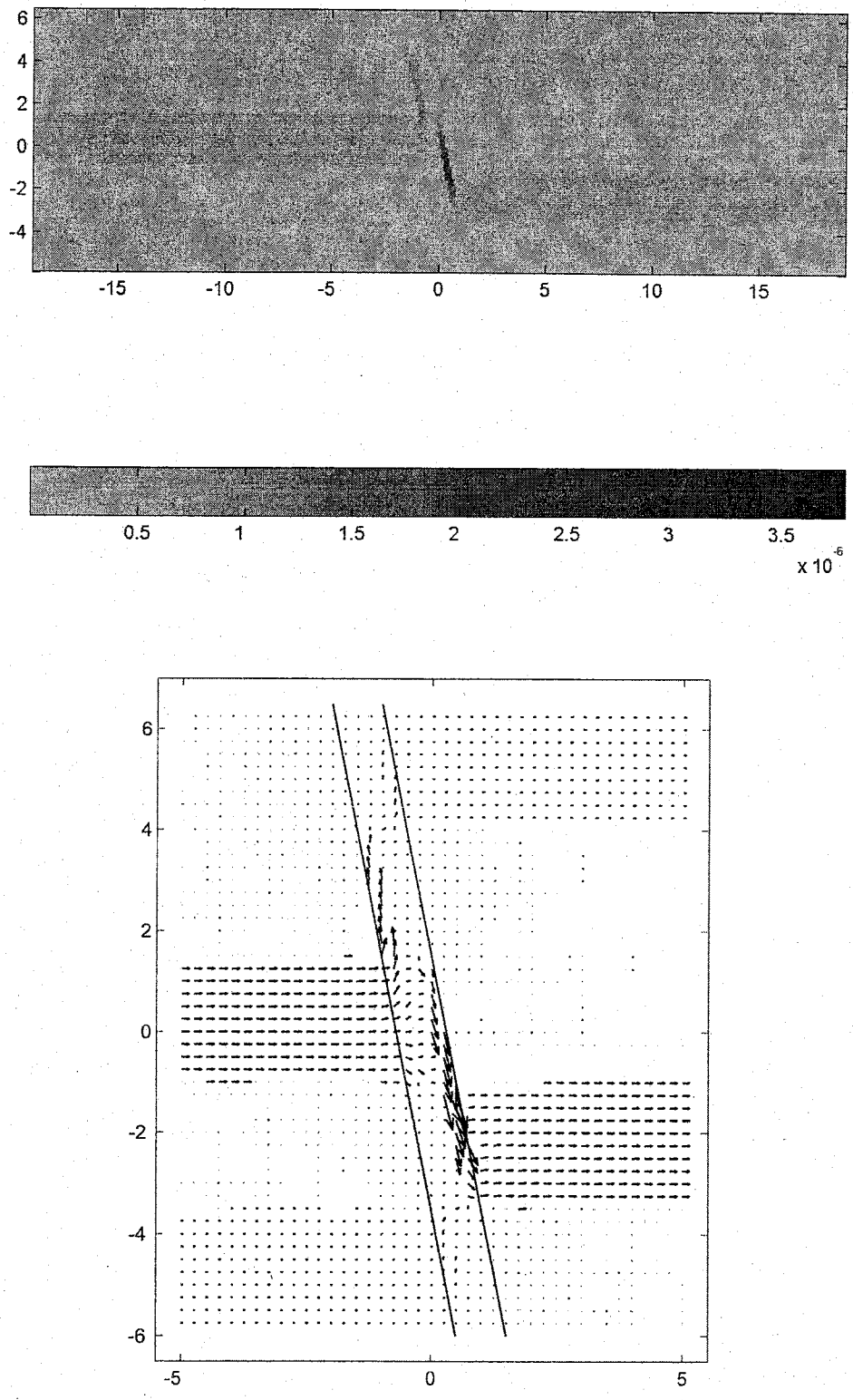

Figure 41. Results for model 3 (subdivided fault), lithified sedimentary rock case. **a)** (top) Scalar specific discharge field. **b)** (bottom) Specific discharge vectors (length exaggerated 3x) for the region adjacent to the fault. Black lines bound the fault zone.

5.4.4. Model 4 - Varied Sedimentary Thickness

In both of these models, the fault zones are subdivided as in the previous set and use the same permeability values. The thickness of the sedimentary strata are such that the silt and siltstone layers are twice as thick as the sand and sandstone layers. The clay and claystone layers are half the thickness of the sand and sandstone layers (Figure 36).

Fault in Poorly Lithified Sediments. Flow arrives at the fault from the left largely in the sand layers (Figure 42a), and exits to the right in the sand layer and the lower silt layer. However, the large amount of flow in the lower silt layer is in part an artifact of the boundary conditions, as in the idealized sedimentary sequence there is always a sand layer below the silt. The bottom no-flow boundary of the model prevents flow from entering this sand layer.

In other respects, the flow patterns are very similar to the previous models of a subdivided fault zone within sedimentary layers of equal thickness (Figure 42b). Flow increases in the silt layers near the fault and deviates strongly from horizontal. The upper hanging wall silt layer collects flow from the fault and diverts it into the hanging wall sand layer within approximately 4 m of the fault. Flow across the low permeability fault core is not even along the dip of the fault, but is much less localized than in the previous model.

Fault with Fractures in Sandstone. Flow arrives at the fault from the left in the sandstone layers (Figure 43a). It exits the fault from the right in the sand layer. Much of the flow in the lower footwall sand layer is diverted up the fault in the relatively high

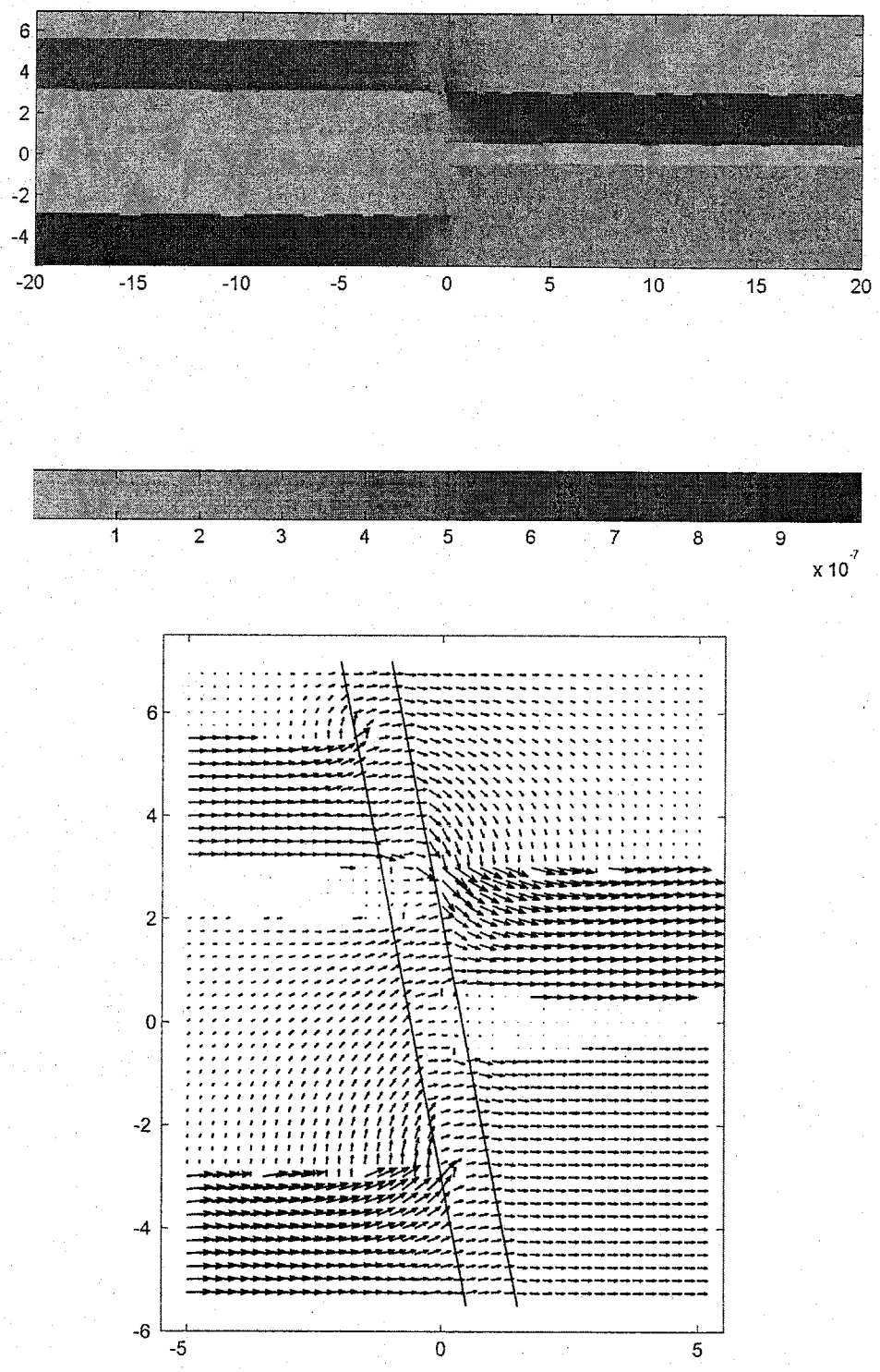

Figure 42. Results for model 4 (varied sedimentary thickness), poorly lithified sediment case. **a)** (top) Scalar specific discharge field. **b)** (bottom) Specific discharge vectors (length exaggerated 2x) for the region adjacent to the fault. Black lines bound the fault zone.

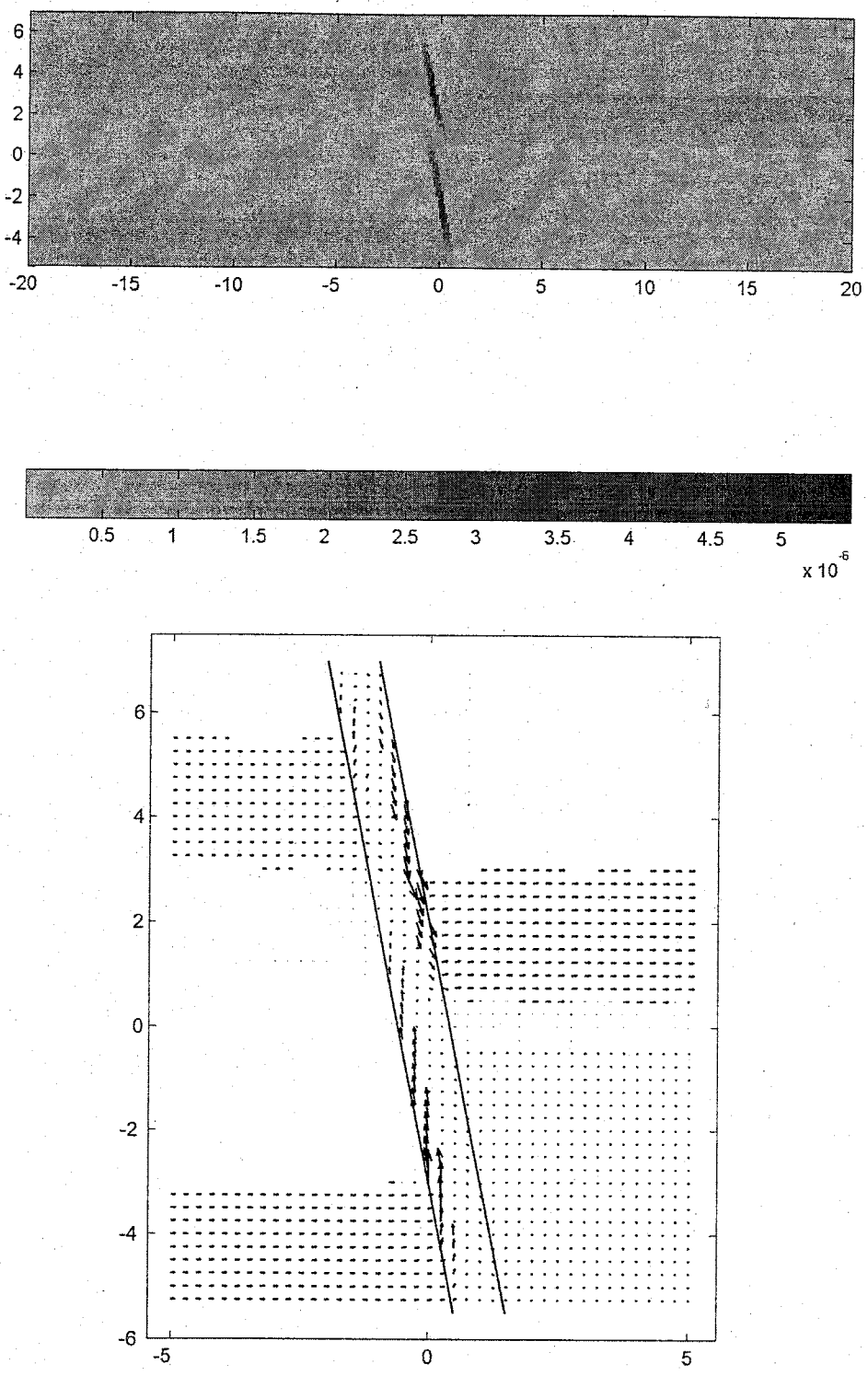

Figure 43. Results for model 4 (varied sedimentary thickness), lithified sedimentary rock case. **a)** (top) Scalar specific discharge field. **b)** (bottom) Specific discharge vectors (length exaggerated 2x) for the region adjacent to the fault. Black lines bound the fault zone.

permeability sandstone and siltstone damage zones, and then crosses the core adjacent to the hanging wall sand (Figure 43b). Flow in the upper footwall sand layer crosses the core directly and enters the hanging wall sand. In general, similar to the other sandstone models, flow is concentrated in the fault and sandstone layers, and little is distributed throughout the lower permeability sedimentary strata.

5.5. Discussion and Implications

Although the models presented here are highly simplified representations of real faulted sedimentary sequences, several significant conclusions can be drawn. The most striking observation is the dramatic difference in flow patterns between the juxtaposition-only scenario (Figure 33) and when fault zone geology is added to the model (Figures 34 and 35). The plane of juxtaposition does not allow fluid to flow up or down the dip of the fault to be redistributed into other layers. Flow travels through the constriction formed by the corner of the footwall layer and the juxtaposition plane to whichever immediately adjacent hanging wall layer has the highest permeability. In contrast, in all of the other models, the presence of a fault with internal structure allows flow to be distributed vertically (both up- and down dip) to varying degrees, to exit the fault at different structural levels. Field evidence, including oriented flow features in the cemented hanging wall mixed zone of the Sand Hill fault (Mozley and Goodwin, 1995), and isotopic compositions of gases with mantle-derived signatures in the San Andreas fault (Kharaka et al., 1999), indicate that over geologic time scales, some faults in poorly lithified sediments and faults with fractures can carry vertical flow. This is consistent with the real, but small (one order of magnitude or less), increase in vertical equivalent

permeability and flux in faults in poorly lithified sediments (Chapter 4). Thus, the juxtaposition model appears to be too much of an oversimplification to be of any use.

The primary difference in the flow patterns around a fault in poorly lithified sediments and a fault with fractures in sandstone is the amount of flow diverted out of the high permeability sand and sandstone layers. Because damage zones in lithified sedimentary rocks have high permeability fracture networks, they effectively distribute fluid up and down the fault zone and no additional flow is induced in the adjacent low permeability strata. Mixed zones in faults in poorly lithified sediments have reduced permeability. Consequently, flow is diverted out of the high permeability strata adjacent to the fault, e.g. from the sand to silt layers, in both the footwall and hanging wall (Figures 38b and 40b). Thus it appears that faults in poorly lithified sediments may induce more flow in low permeability host strata than do faults with fractures in sandstone. In addition, the flow vectors in the silt layers vary widely in orientation (e.g. Figure 42b). This offers a possible explanation for the varied orientations of flow features in the cemented hanging wall mixed zone of the Sand Hill fault.

Varying the thickness of the sedimentary layers and subdividing the fault zone units appear to have only secondary impacts on the fluid flow patterns described above. In both fault zone types, these variations cause some degree of flow focussing across the fault core. In the poorly lithified sediment case, these variations slightly increase the distance away from the fault over which flow is induced in the silt layers (compare Figures 38b, 40b, and 42b). These additional complexities therefore may not need to be included in flow models to achieve a reasonable simulation of the fluid flow patterns around faults.

On the other hand, prediction of the flow paths and travel times of contaminants from localized sources requires an understanding of geologic heterogeneity on length scales similar to the size of the source (McCord and Stephens, 1999), which may be quite small (say, <10 m). This applies to faults as well as the aquifers they cut. While at present we have a very good understanding of the average internal architecture and permeability structure of faults in poorly lithified sediments, and the basic controls on fault zone architecture (Heynekamp et al., 1999) imposed by the nature of the host sedimentary sequence, we cannot predict what a given fault's internal architecture will be at such small length scales, sight unseen. Therefore, it follows that, although this study has identified the first-order patterns of fault-proximal fluid flow, the details of the flow patterns around a given fault that may be relevant to a contaminant transport problem will depend on its local internal structure and the adjacent stratigraphy. Hydrologic studies requiring this level of detail in the subsurface flow patterns will continue to require detailed site-specific geologic characterization efforts.

5.6. Conclusions

The finite element models of horizontal fluid flow in faulted sedimentary sequence presented here show fundamental differences in fluid flow patterns when the geology of the modeled fault is varied from simple juxtaposition to a complex fault in either poorly lithified sediments or lithified sedimentary rocks. Comparison of oriented flow features and isotopic measurements of gases within faults with the fluid flow patterns predicted by juxtaposition alone shows that this is an oversimplification of fault zone geology. Simple three-part faults with realistic permeability distributions result in

significant differences in the fluid flow patterns. In faulted poorly lithified sediments, the low permeability fault zone induces flow in low permeability strata adjacent to the fault. This is not the case in faulted lithified sedimentary rocks with fracture-rich damage zones. Increasing fault zone complexity or varying the thickness of the sedimentary layers does not significantly change the fluid flow patterns around the faults. Representing the internal architecture of faults in poorly lithified sediments and in lithified sedimentary rocks with a three part model therefore appears to be adequate to model steady-state fluid flow in geologic models. These results are in accord with equivalent permeability calculations for similar idealized fault zone models.

5.7. References Cited

Anderson, T. W., Welder, G. E., Lesser, G., and Trujillo, A., 1988, Region 7, Central alluvial basins, *in* Back, W., Rosenshein, J. S., and Seaber, P. R., eds., Hydrogeology: Boulder, CO, Geological Society of America, Geology of North America, v. O-2, p. 81-86.

Antonellini, M. A., and Aydin, A., 1994, Effect of faulting on fluid flow in porous sandstones: petrophysical properties: American Association of Petroleum Geologists Bulletin, v. 78, p. 355-377.

Antonellini, M. A., and Aydin, A., 1995, Effect of faulting on fluid flow in porous sandstones: geometry and spatial distribution: American Association of Petroleum Geologists Bulletin, v. 79, p. 642-671.

Aydin, A., and Johnson, A. M., 1978, Development of faults as zones of deformation bands and as slip surfaces in sandstone: Pure and Applied Geophysics, v. 116, p. 931-942.

Bredehoeft, J. D., Belitz, K., and Sharp-Hansen, S., 1992, The hydrodynamics of the Bighorn Basin: A study of the role of faults: American Association of Petroleum Geologists Bulletin, v. 76, p. 530-546.

Caine, J. S., Evans, J. P., and Forster, C. B., 1996, Fault zone architecture and permeability structure: Geology, v. 24, p. 1025-1028.

Caine, J. S., and Forster, C. B., 1999, Fault zone architecture and fluid flow: insights from field data and numerical modeling, *in* Haneberg, W. C., Mozley, P. S., Moore, K. C., and Goodwin, L. B., eds., Faults and subsurface fluid flow in the shallow crust: Washington, DC, American Geophysical Union, p. 101-127.

Domenico, P. A., and Schwartz, F. W., 1990, Physical and chemical hydrogeology: New York, John Wiley, 824 p.

Evans, J. P., Forster, C. B., and Goddard, J. V., 1997, Permeability of fault related rocks, and implications for hydraulic structure of fault zones: Journal of Structural Geology, v. 19, p. 1393-1404.

Forster, C., and Evans, J., 1991, Hydrogeology of thrust faults and crystalline thrust sheets: results of combined field and modeling studies: Geophysical Research Letters, v. 18, p. 979-982.

Foxford, K. A., Walsh, J. J., Watterson, J., Garden, I. R., Guscott, S. C., and Burley, S. D., 1998, Structure and content of the Moab Fault Zone, Utah, USA, and its

implications for fault seal prediction, *in* Jones, G., Fisher, Q. J., and Knipe, R. J., eds., Faulting, fault sealing, and fluid flow in hydrocarbon reservoirs: London, Geological Society, p. 87-103.

Haneberg, W. C., 1995, Steady-state groundwater flow across idealized faults: Water Resources Research, v. 31, p. 1815-1820.

Heynekamp, M. R., Goodwin, L. B., Mozley, P. S., and Haneberg, W. C., 1999, Controls on fault-zone architecture in poorly lithified sediments, Rio Grande Rift, New Mexico: Implications for fault-zone permeability and fluid flow, *in* Haneberg, W. C., Mozley, P. S., Moore, K. C., and Goodwin, L. B., eds., Faults and subsurface fluid flow in the shallow crust: Washington, DC, American Geophysical Union, p. 27-50.

Hooper, E. C. D., 1991, Fluid migration along growth faults in compacting sediments: Journal of Petroleum Geology, v. 14, p. 161-180.

Kernodle, J. M., 1998, Simulation of ground-water flow in the Albuquerque Basin, central New Mexico, 1901-1995, with projections to 2020: U.S. Geological Survey Open File Report 96-209, 54 p.

Kharaka, Y. K., Thordsen, J. J., Evans, W. C., and Kennedy, B. M., 1999, Geochemistry and hydromechanical interactions of fluids associated with the San Andreas fault system, California, *in* Haneberg, W. C., Mozley, P. S., Moore, J. C., and Goodwin, L. B., eds., Faults and subsurface fluid flow in the shallow crust: Washington, DC, American Geophysical Union, p. 129-148.

Knipe, R. J., 1993, The influence of fault zone processes and diagenesis on fluid flow, *in* Horbury, A. D., and Robinson, A. G., eds., Diagenesis and basin development: AAPG

studies in geology: Tulsa, OK, American Association of Petroleum Geologists, p. 135-151.

Kolm, K. E., and Downey, J. S., 1994, Diverse flow patterns in the aquifers of the Amargosa Desert and vicinity, southern Nevada and Califronia: Association of Engineering Geologists Bulletin, v. 31, p. 33-47.

Matthai, S. K., and Roberts, S. G., 1996, The influence of fault permeability on single-phase fluid flow near fault sand intersections: results from steady-state high-resolution models of pressure-driven fluid flow: American Association of Petroleum Geologists Bulletin, v. 80, p. 1763-1779.

McCord, J. T., and Stephens, D. B., 1999, Contrasts in regional and local-scale heterogeneity in relation to ground-water supply and contamination in the Albuquerque basin, *in* Pazzaglia, F. J., and Lucas, S. G., eds., Albuquerque Geology: New Mexico Geological Society, 50th Annual Field conference, Guidebook, p. 401-408.

Mozley, P. S., and Goodwin, L. B., 1995, Patterns of cementation along a Cenozoic normal fault: A record of paleoflow orientations: Geology, v. 23, p. 539-542.

Shafike, N. G., and Flanigan, K. G., 1999, Hydrologic modeling of the Estancia Basin, New Mexico, *in* Pazzaglia, F. J., and Lucas, S. G., eds., Albuquerque Geology: New Mexico Geological Society, 50th Annual Field conference, Guidebook, p. 409-418.

Thorn, C. R., McAda, D. P., and Kernodle, J. M., 1993, Geohydrologic framework and hydrologic conditions in the Albuquerque Basin, central New Mexico: U. S. Geological Survey Water Resources Investigations Report 93-4149, 106 p.

CHAPTER 6. CONCLUSIONS

6.1. Overview

In the introduction, five questions were laid out as the objectives of this study of faults in the poorly lithified Santa Fe Group sediments of the Rio Grande rift. Below, the answers to each are summarized as the main results of the study, followed by suggestions for future work.

6.2. How do the Outcrop-scale Structures and Architectural Elements Develop?

The initial incorporation of sediment into the normal faults in poorly lithified sediments I have studied is inferred to occur by tip-line and asperity bifurcation, processes that also occur in brittle faults in crystalline and lithified sedimentary rocks. Additional sediment may be incorporated throughout the movement history of the fault. Initiation of mixed zones can occur very early during fault-zone evolution and need not be preceded or accompanied by extensive damage-zone development. Field and microstructural observations indicate that the earliest stages of deformation within the

mixed and core zones of the Sand Hill and Santa Ana faults are accomplished by sediment disaggregation by pervasive particulate flow with subordinate cataclasis. This is followed by a mode of failure transition to cataclastic deformation, which results in the overprinting of macroscopically ductile structures with deformation bands. These overprinting relationships are consistent with the inferred stress and consolidation history of the studied faults and their host sediments.

6.3. What are the Primary Deformation Mechanisms?

The majority of the deformation in the faults studied is accommodated by grain boundary sliding. This is facilitated to varying degrees by cataclasis. The nature of cataclasis in these faults is different from that in brittle faults in crystalline and lithified sedimentary rocks. I observe that the style of grain breakage is dependent on relative grain strength. Specifically, from strongest to weakest: 1) Quartz deformation is accomplished by flaking or spalling of small chips from the perimeters of grains; 2) Feldspars deform by transgranular fracturing, facilitated by their well developed cleavage; and 3) Volcanic lithic grains deform primarily by distributed microcracking and to a lesser extent, transgranular fracturing. Particle size measurements reveal that cataclasis preferentially breaks down the intermediate sized particles, resulting in flattening of the particle size distributions. I interpret this process of grain boundary sliding facilitated by grain-strength dependent cataclasis to be an example of controlled particulate flow. In this scenario, the rate of grain boundary sliding is controlled by intragranular deformation (i.e. cataclasis), but the amount of sliding of any individual grain is not limited by this deformation, and the relative movements of most grains did

not require intense intragranular deformation to the degree seen in brittle faults in crystalline and lithified sedimentary rocks.

6.4. What is the Permeability Structure of Large Displacement Normal Faults in Poorly Lithified Sediments?

The basic structural element of brittle faults in crystalline and lithified sedimentary rocks is the fracture; in faults in poorly lithified sandy sediments it is the deformation band. Fractures have increased porosity and permeability relative to their host rocks, whereas most deformation bands have reduced porosity and permeability relative to their host sediments. These fundamental differences result in contrasting outcrop-scale fault-zone permeability structures. Deformation and diagenesis within brittle faults in crystalline and lithified sedimentary rocks can both increase and decrease permeability in a spatially heterogeneous manner. However, on average, these processes should result in a fault zone that is likely to be a vertical flow conduit, with high permeability damage zones flanking a low permeability core. Conversely, structural and diagenetic processes in faults similar to the Sand Hill fault should result in lower permeability mixed and core zones when compared to all but the lowest permeability (i.e., clay-rich) protolith materials. Such faults are effective barriers to cross-fault fluid flow, and have little potential to be pronounced vertical flow conduits, especially when compared with brittle faults in crystalline and lithified sedimentary rocks.

6.5. What are the Implications of this Permeability Structure for Fault-Proximal and Basin-Scale Subsurface Fluid Flow?

Integration of field observations with our numerical models of subsurface fluid flow in faulted sedimentary sequences indicates that juxtaposition of strata alone is an oversimplification of the fault zones in this study. In normal faults in poorly lithified sediments, the low permeability mixed and core zones induce flow in low permeability strata adjacent to the fault. This is not the case in faulted lithified sedimentary rocks with high-permeability, fracture-rich damage zones, in which fault-parallel flow is localized. For both fault types, increasing the internal structural complexity of the fault zone or varying the thickness of the sedimentary layers does not significantly change the basics of the fluid flow patterns around the faults.

Results for brittle faults in crystalline and lithified sedimentary rocks indicate that their bulk hydrologic properties result in enhanced vertical flow and a lesser tendency for the fault zone to act as a barrier to horizontal flow, in agreement with the conventionally accepted conceptual model for such faults. The results from the numerical simulations of fluid flow patterns presented herein are consistent with inferences based on equivalent permeability calculations of idealized fault zone models. These calculations lead us to infer that the bulk hydrologic properties of faults in poorly lithified sediments can significantly impede horizontal subsurface fluid flow at a regional scale and do result in great potential for enhanced vertical flow.

6.6. How can the Geology and Permeability Structure of these Faults best be Incorporated into Subsurface Fluid Flow Models?

This study indicates that when incorporating faults into basin–scale fluid flow models, or considering the essentials of fluid flow patterns around faults, it is critically important to correctly describe the geology, and thus the permeability structure, of the fault. However, my analytical and numerical models suggest that only the mixed zones and core zone, or damage zones and core zone, are necessary for such large-scale simulations. In either case, a three-part fault zone with appropriate relative permeability values appears to simulate the permeability structure of faults in poorly lithified sediments and in lithified sedimentary rocks with sufficient accuracy. To a first approximation, this appears adequate to realistically model steady-state fluid flow in geologic models, especially at large scales, and is a significant advance over simple juxtaposition of strata across a plane.

6.7. Suggestions for Future Work

Although the results of this study greatly increase our understanding of the geology of fault zones and their hydrologic importance, many unanswered questions and fruitful lines of research remain to be explored. An obvious question is the nature of the transition between the two fault types, those based on fractures and those based on deformation bands. It is probable that an individual fault zone, with progressive lithification over geologic time, can develop structures characteristic of both types (e.g., fractures may overprint mixed zones and deformation bands). This transition may be also be expected with increasing depth along a given fault. Ongoing studies at New Mexico

Tech of the San Gregorio fault strand of the San Andreas fault should prove to be enlightening in this regard.

While the hydrologic importance of the core zone in faults in poorly lithified sediments is central to the main conclusions of this work, its origin remains largely a mystery. This is largely due to the nontrivial problem of preparing wet, friable, foliated clay for microstructural studies. An important question to be resolved is why the clay core is virtually always present and continuous, even where the adjacent sediments have little clay, and/or the offset along the fault is very small. This suggests that injection of clay along the fault plane (due to high pore fluid pressures?) may be an (the?) important process for generation of the core. Further work should address this question in more detail.

The possibility of clay injection raise the issue of the dynamics of faulting in poorly lithified sediments. What role does pore pressure variation during the seismic cycle play in these materials? For that matter, are the faults observed in this study the product of seismic or aseismic deformation, or both? More specifically, what is the role of slip rate in generating the characteristic internal architecture and overprinting relationships of faults in poorly lithified sediment? Or are these features more dependent on the stress history of the fault zone and adjacent sediments? These remain open questions, and avenues for future study.

The hydrologic conclusions of this work, and particularly their relevance to basin scale fluid-flow models, are robust. However, several aspects of the numerical flow modeling can certainly be improved. One obvious example of a boundary condition effect in the models was noted in Chapter Five, namely extensive flow in a silt layer due

to the lower domain boundary being a no-flow barrier. We considered implementing periodic boundaries conditions in the models to eliminate such artifacts, but it proved unsuccessful. A more exhaustive approach to the flow modeling described in Chapter Five, implementing such improvements as periodic boundary conditions, is a worthwhile future study. However, it may be that the limiting factor in what can be usefully derived from such an effort is the basic geologic input. For example, prediction of the flow paths and travel times of contaminants across faults at the level of detail required to predict, say, when they might arrive at a particular water supply well, is probably beyond the ken of such idealized models. Simulation of fault zone geology and fault-related fluid flow at this level of detail will probably continue to require site-specific geologic characterization.

APPENDIX 1. AN OVERVIEW OF CRITICAL STATE SOIL MECHANICS

A1.1. Introduction

The theory of critical state soil mechanics attempts to describe the deformation by grain scale flow of particulate or granular materials. It was primarily developed for use in solving applied civil and geotechnical engineering problems, and there is a vast literature on the subject, both experimental and theoretical. The fundamental postulate of the model, verified in numerous experiments on natural soils and artificial particulate aggregates of sand, silt, clay, glass beads, sugar, and other materials, is the concept of the critical state to which the materials evolve with increasing finite strain. The critical state is defined as the state at which deformation proceeds at nominally constant stress and volume (Atkinson and Bransby, 1978). This appendix is an overview of the main concepts of the theory.

The application of critical state soil mechanics in structural geology has been limited, perhaps due to the experimental and quantitative nature of the theory and its derivation from, and usual application to, materials that are not considered "geologically interesting". Notable exceptions are studies on incipient deformation in the accretionary

wedge environment (Moore, 1986) and processes such as slope failure (Ellen and Fleming, 1987). However, Jones and Addis (1986) proposed that the gravitational compaction and tectonic deformation of sediments in extensional basins may be fruitfully addressed with the critical state model. Although usually applied to soils and surficial deposits, they point out that the basic tenets of the model may be expected to hold at mean stresses up to 100 MPa, corresponding to depths of several kilometers or more in a sedimentary basin.

A1.2. Basic Concepts of Critical State Soil Mechanics

This section is a description of the critical state model and its representation in volumetric strain – stress space. The overview and relevant figures are based on readings from Atkinson and Bransby (1978), Scott (1980), Jones and Addis (1986), and Jones and Preston (1987) and figures therein, to which I refer the reader for a more detailed exposition of the relevant experiments and theory.

The general form of the critical state surface is shown in Figure A1.1. The three axes of the diagram are the effective mean stress,

$$p' = \frac{1}{3}(\sigma_1' + \sigma_2' + \sigma_3'), \tag{A1.1}$$

the differential stress,

$$q' = \sigma_1' - \sigma_3', \tag{A1.2}$$

and the specific volume,

$$v = 1 + e, \tag{A1.3}$$

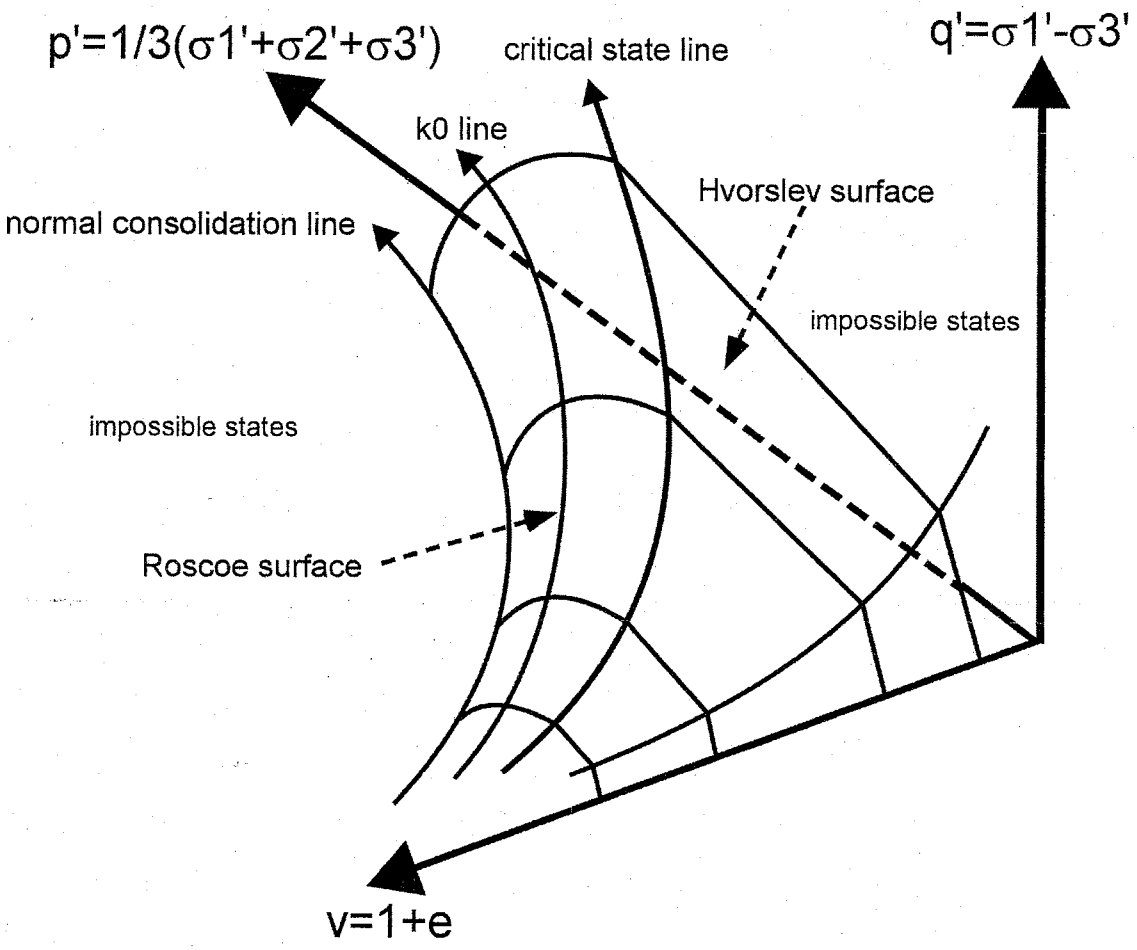

Figure A1.1. A perspective view of the critical state diagram (after Jones and Addis, 1986). See text for details.

where e is the void ratio (volume of pores/volume of solids) of the sediment, and $\sigma_1' < \sigma_2' \leq \sigma_3'$. Compressional stresses are taken as negative. Thus the directions of increasing p' and q' are towards increasingly negative values. Note that the stress axes are in terms of effective stress ($\sigma' = \sigma - P_p$), and so account for the effects of pore fluid pressure (P_p). The specific volume is the volume of sediment (pores and solids) that contains one unit volume of solids. It is equal to 1/(1-porosity) and scales directly with porosity.

Various types of tectonic loading and the resulting volumetric strains are represented as paths in this space, called stress paths. Stress paths show the evolution of stress and volumetric strain during a deformation event. In visualizing stress paths, it is useful to consider the three bounding planes, p'-v, v-q', and p'-q', or slices through critical state space parallel to one of these bounding planes (Figures A1.2a, b, and c). Certain types of deformation can be represented entirely within a particular plane. For example, compaction (or consolidation in the soil mechanics literature), which is the time dependent porosity loss and net volume reduction of a soil or sediment due to the increasing weight of overburden (Jones and Preston, 1987; Karig and Hou, 1992), is represented in the p'-v plane, as the volume change is a function only of the increasing mean stress. Likewise, the loci of constant volume (undrained) deformation stress paths are all in planes parallel to the p'-q' axes. More complex deformations may be more easily visualized via the projections of the stress paths in the three bounding planes.

The three dimensional shape of the critical state surface has been determined by experiments on numerous materials. Although the details vary from clays to sands to

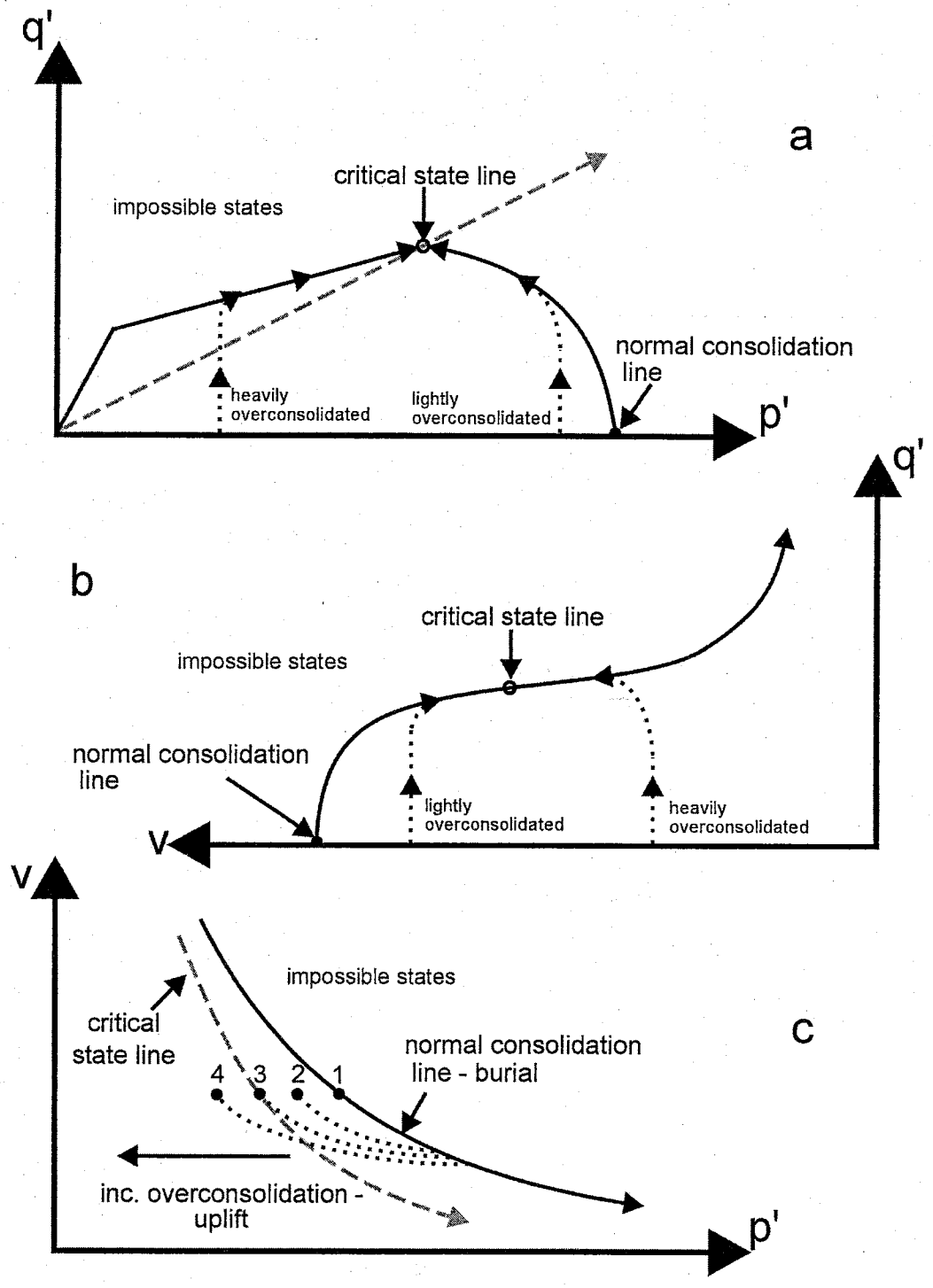

Figure A1.2. Three mutually perpendicular slices through the critical state diagram (after Scott, 1980).

poorly consolidated sediments, the overall shape is the same and retains several key features (see Figures A1.1 and A1.2):

1. The *critical state line* is the boundary between the Roscoe and Hvorslev surfaces, which together form the *state boundary surface*. It separates possible from impossible states of stress and specific volume. Stress paths cannot cross these surfaces, but they can move along them.

2. The critical state line is the locus of states at which shear strain increases indefinitely, but stress and volume remain constant. A stress path for a material deformed to failure will terminate at the critical state line. As described below, it is a fundamental boundary between stress paths for normally consolidated and highly overconsolidated sediments. As seen in Figure A1.2c, its projection in the p'-q' plane is a straight line (the dashed gray line).

3. The assumption is generally made that soils cannot sustain tensional stresses. Therefore, taking tensional stresses as positive, in a triaxial state $\sigma_2' = \sigma_3' \leq 0$. If $\sigma_2' = \sigma_3' = 0$ and $q' = \sigma_1' \leq 0$, then $p' = \sigma_1'/3$ and $q'/p' = 3$. Thus, the Hvorslev state boundary surface is bounded near the v-q' plane by an inclined plane with a slope $q'/p' = 3$ (see Figure A1.1).

4. The critical state line is contained entirely within the p'-v plane and can also be shown with v as a decreasing linear function of ln p'.

A1.3. Interpreting Deformation Histories on the Critical State Diagram

It is useful to see how a few simple and common stress paths are represented on the critical state diagram. In addition to familiarizing the reader with the use of the diagram, several important concepts can be illustrated.

A1.3.1. Consolidation of Sediments

A very basic stress path that can be considered within the critical state diagram is the consolidation of sediments under the influence of gravity. Sediments deposited in a basin will initially have high porosity and as the overburden thickens they will begin to decrease in volume through time-dependent reduction in specific volume. If the pores are water filled, this is associated with an expulsion of the pore waters. This is represented on the p'-v plane by the normal consolidation line, which shows an exponential decrease of volume with increasing mean stress and time, assuming the increasing mean stress is due to increasing overburden due to sedimentation (Jones and Addis, 1986). Sediments plotting on this line (e.g., point 1, Figure A1.2c) are referred to as normally consolidated, and their porosity is in equilibrium with the effective mean stress. When a normally consolidated sediment is unloaded, there is only a partial volume recovery. This results in the sediment having a lower specific volume than that which would be in equilibrium with the given mean stress. Points 2, 3, and 4 on Figure A1.2c show increasing degrees of overconsolidation. A common cause of overconsolidation is partial exhumation of the sediment with a reduction of the overburden stress (Jones and Addis, 1986; Jones and Preston, 1987).

Excess pore water pressure (overpressure) greater than hydrostatic may be generated when the rate of pore pressure diffusion is slower than the rate of sedimentary

or tectonic loading. This may be due to low permeability of the sediment or a long drainage path (Gretener, 1976). This excess pressure will prop open the pores and prevent significant decreases in volume. A rapid drop in pore pressure would increase the effective stress and leave the sediment in an underconsolidated state, which plots in the "impossible states" region of the p'-v plane. This state cannot be maintained, and the sediment will rapidly compact to a point on the normal consolidation line.

Three-dimensional consolidation represented by the normal consolidation line is due to changes in the effective mean stress caused by an increasing pressure acting in all directions. A more relevant geologic stress path is that of dewatering sediments in a subsiding basin subjected to increasing overburden pressure in which there is vertical compaction with negligible lateral expansion (Jones and Addis, 1986; Karig and Hou, 1992). The locus of stress-volume states corresponding to this condition is shown on the critical state diagram by the k_0 line. It corresponds to a state of stress allowing no lateral strain (uniaxial strain); $\sigma_H' = k_0\sigma_V'$. It has a shape similar to the normal consolidation line, but plots above the p'-v plane, indicating that there is a net effective differential stress ($q'>0$, $\therefore k_0 < 1$) for this stress path. As the effective mean stress increases, the differential stress increases and the specific volume decreases. Sediments of different composition will have different k_0 lines, as the value of k_0 varies with lithology (Karig and Hou, 1992). The projection of the k_0 line in the p'-v plane would appear as a curve roughly parallel to the normal consolidation line. Similar to sediment undergoing normal consolidation, sediment undergoing compaction along the k_0 line will evolve to an overconsolidated state if unloaded. The projection of the unloading curves on the p'-v

plane would appear similar to those shown for the case of normal consolidation (dark dashed lines in Figure A1.2c).

A1.3.2. Tectonic Deformation of Sediments

In addition to the stresses induced by consolidation of the sediments in an extensional basin, there is a superposed tectonic stress field, with the maximum compressive stress oriented vertically in an extensional system (Anderson, 1951). I will assume for the purposes of discussion that the horizontal stresses are approximately equal. The differential stress due to the addition of tectonic stresses can lead to failure of the sediments in the basin and the formation of normal faults, which can be treated as failure with maximum compression vertical. The critical state model assumes that soils (or in this case, sediments) have no tensile strength. There are two important parameters to consider when treating deformation of sediments in the critical state framework: the consolidation state of the sediments and the degree of drainage of the system, which is intimately related to the permeabilities of the sediments and their evolution with strain. The stress path followed by a given sediment will vary significantly with these parameters. Consideration of different types of stress paths helps to illustrate the fundamental concepts of the critical state model. Again, this discussion is based on the references listed at the beginning of section A1.2., where more detailed treatments can be found.

Drained Deformation. In this case the pore fluids are free to drain out of the deforming volume, and pore pressure is constant throughout the deformation event. Geologically, this corresponds to the sediment being permeable enough and/or the strain rate being slow enough to allow free drainage even of relatively impermeable sediments.

p', q' and v all may vary during a deformation event. Figure A1.2b is a slice through the critical state diagram parallel to the v-q' plane at some given mean stress level. Three different drained stress paths are shown, and they may be viewed as projections into this plane, with variations in p' taking place into and out of the page.

At the onset of tectonic loading, a normally consolidated sediment will immediately begin to decrease in volume and the stress path will move along the trace of the Roscoe state boundary surface (see Figure A1.1) towards the critical state line. When the stress path reaches this point, the sediment is said to be in the *critical state*, and it will remain at this stress state indefinitely as deformation proceeds, accumulating strain at constant volume and stress.

A lightly overconsolidated sediment when subjected to tectonic loading will at first deform approximately elastically and eventually will begin to compact as the stress path approaches the Roscoe state boundary surface. Again, the stress path will evolve along this surface to the critical state, and the sample will deform there at constant volume and stress.

The drained deformation behavior of highly overconsolidated sediments is significantly different from the preceding two cases. As in the lightly overconsolidated case, the initial deformation is approximately elastic; this shows the significance of overconsolidation in general, in that some degree of tectonic loading or differential stress can be maintained without significant permanent plastic strain. The overconsolidated sediment is closer to the origin, and so the stress path intersects the Hvorslev state boundary surface *at a stress level higher than that at the critical state.* This intersection stress is the peak or failure strength of the sediment. At this point the sediment will fail

and deformation will localize in a narrow shear band or zone. This localization is significant, for the sediment is no longer deforming homogeneously; material *outside* of the shear zone has effectively been unloaded, and no longer accumulates plastic strain other than that perhaps imposed by irregularities in the geometry of the shear zone. The material *inside* the shear zone continues to evolve along the Hvorslev surface to a stable stress-volume condition at the critical state line.

Undrained Deformation. During undrained deformation, the pore fluids are not free to drain out of the deforming volume. In nature this may be caused by (seismic?) strain rates faster than the drainage rate of fluids from the pores and/or the deforming volume may contain low permeability pods or layers (e.g., clays or cemented zones) that prevent rapid dissipation of pore pressure variations. In laboratory tests on soils and sediments carried out under undrained conditions, the overall sample volume remains constant. While this strict constant volume condition is probably not maintained in natural undrained deformations, in both the laboratory and nature the changes in pore pressure must dominate over volume changes. If volume change is suppressed during deformation, the pore volume changes will be manifested as pore pressure fluctuations of the opposite sign of the expected volume change. Stress paths for undrained deformation plot on planes of constant specific volume, parallel to the q'-p' plane. Figure A1.2a is a constant specific volume slice through the critical state diagram at some positive specific volume, with three different stress paths shown, corresponding to three different initial consolidation states.

In undrained tectonic deformation, normally consolidated sediments follow a constant volume, decreasing p' path along the Roscoe state boundary surface towards the

critical state line. Although the bulk volume of the deforming sediment remains approximately constant, the pore volume must be decreasing as the sediment strains and the grains move relative to one another to accommodate the deformation. This is manifested as a pore pressure increase, and a decrease in p'. Lightly overconsolidated sediments behave similarly, but with an initial approximately elastic stress path before significant grain reorganization and associated pore pressure increases.

Heavily overconsolidated sediments are initially closer to the origin than the critical state line, and after an initial rise in differential stress and associated elastic deformation, the stress path intersects the Hvorslev state boundary surface. It then follows a decreasing pore pressure path along this surface to the critical state line, at which point deformation will proceed at a constant specific volume and stress. Although the bulk volume of the deforming sediment remains approximately constant, the pore volume must be increasing as the sediment strains and the grains move relative to one another to accommodate the deformation.

It is important to note that the undrained stress paths all terminate at a maximum differential stress at the critical state line. This implies relatively homogenous, stable deformation without the strain-softening and localization observed in the behavior of drained, heavily overconsolidated sediments.

An illustrative real-world example of the variations in deformation behavior predicted by the critical state model is provided by Ellen and Fleming (1987). They studied debris flows around the San Francisco Bay area and observed two common flow morphologies: wide hummocky flows in which the material was pervasively deformed and behaved essentially as a fluid; and flows which retained some cohesion and moved

essentially as blocks along a basal shear zone. They attributed these differences to whether or not the deformation was dilatant or compactive, and the degree of drainage during shearing.

The hummocky soils were initially normally consolidated and so experienced a net volume loss when sheared. Also, because of their low permeability the pore pressure could not drain fast enough to keep pace with the strain rate and they underwent partial liquefaction (the pore pressure increased enough to support the weight of the soil). The whole mass moved downslope as a fluid. In contrast, the block-like flows formed from soil that was overconsolidated and thus were dilatant when sheared. The deformation quickly localized into a basal shear zone, and the remainder of the slipped mass stayed relatively intact as it moved downslope.

A1.4. Summary

In sum, the stress paths for sediments in various states of consolidation deformed under hydrostatic or differential stress states illustrate the evolution of stress and porosity (specific volume). When subjected to stress, both sand- and clay-rich sediments strive to attain an equilibrium stress-porosity state, represented by the normal consolidation line, the k_0 line, or the critical state line. This equilibrium stress-porosity state is a function of the applied stresses and the initial sediment volume (density) and is the fundamental concept of the critical state theory. The normal consolidation line represents the equilibrium condition under hydrostatic loading. The rest of the diagram above this plane may be thought of as the additional effects of differential or shear stresses on the sediment's stress-porosity state. This is illustrated by the projections of the k_0 line and the

critical state line in the p'-v plane (gray dashed lines in Figure A1.1). At any given mean stress, the effect of differential stress is to reduce the equilibrium porosity.

A1.5. References Cited

Anderson, E. M., 1951, The dynamics of faulting and dyke formation, with applications to Britain: Edinburgh, Oliver and Boyd, 206 p.

Atkinson, J. H., and Bransby, P. L., 1978, The mechanics of soils: an introduction to critical state soil mechanics: New York, New York, McGraw-Hill, 375 p.

Ellen, S. D, and Fleming, R. W., 1987, Mobilization of debris flows from soils slips, San Francisco Bay region, California: Geological Society of America, Reviews in Engineering Geology, v 7, p. 31-40.

Gretener, P. E., 1976, Pore pressure: fundamentals, general ramifications and implications for structural geology: American Association of Petroleum Geologists continuing education course notes series 4, 87 p.

Jones, M. E., and Addis, M. A., 1986, The application of stress path and critical state analysis to sediment deformation: Journal of Structural Geology, v. 8, p. 575-580.

Jones, M. E., and Preston, R. M. F., 1987, Deformation of sediments and sedimentary rocks, Geological Society Special Publication 29: London, Blackwell Scientific Publications, 350 p.

Karig, D. E., and Hou, G., 1992, High -stress consolidation experiments and their geologic implications: Journal of geophysical research, v. 97, p. 289-300.

Moore, J. C., ed., 1986, Structural fabric in deep sea drilling project cores from forearcs: Geological Society of America Memoir 166, 160 p.

Scott, C. R., 1980, Soil mechanics and foundations: London, Applied Science Publishers, 406 p.

APPENDIX 2. SAND HILL FAULT PERMEABILITY MEASUREMENTS

Air mini-permeameter measurements - data are log(k); k in m^2				
sand protolith	**sandy mixed zone**	**sandy mixed zone**	**sandy mixed zone**	**cemented hw* mixed zone**
-10.71	-11.49	-10.89	-12.20	-12.74
-10.73	-11.49	-11.28	-12.18	-13.70
-10.41	-11.07	-11.16	-12.49	-13.27
-10.59	-11.13	-11.36	-11.94	-13.37
-10.95	-11.28	-10.94	-11.00	-13.78
-10.85	-11.58	-10.90	-10.57	-13.11
-9.98	-11.24	-11.30	-11.18	-13.86
-10.19	-10.72	-11.29	-11.08	-13.00
-10.79	-11.26	-10.99	-11.29	-13.59
-10.56	-10.99	-10.89	-10.80	-13.67
-10.35	-11.03	-11.85	-11.26	-13.38
-10.80	-11.21	-11.43	-11.26	-13.48
-10.23	-11.14	-11.29	-11.02	-13.56
-10.04	-11.06	-11.05	-11.07	-13.37
-10.66	-11.21	-10.70	-10.70	-14.13
-10.58	-11.09	-10.80	-10.98	-13.72
-10.28	-11.01	-10.91	-11.25	-13.64
-10.26	-11.15	-10.34	-11.38	-13.62
-10.20	-10.94	-10.22	-11.39	-13.70
-10.12	-10.97	-10.22	-11.47	-13.74
-10.04	-10.94	-11.35	-11.49	-13.71
-10.02	-10.65	-11.11	-11.35	-13.49
-10.15	-10.90	-11.06	-11.55	-13.39
-10.95	-11.25	-11.29	-11.27	-13.42

* hanging wall

sand protolith cont.	sandy mixed zone cont.	sandy mixed zone cont.	sandy mixed zone cont.	cemented hw mixed zone cont.
-10.58	-11.04	-11.38	-11.42	-13.06
-10.94	-11.42	-11.23	-11.24	-13.16
-10.87	-11.47	-11.31	-11.33	-13.72
-11.01	-11.19	-11.40	-11.23	-13.51
-10.61	-11.15	-11.87	-10.98	-13.17
-10.74	-11.27	-11.18	-10.62	-12.85
-10.65	-11.15	-11.20	-11.00	-13.21
-10.45	-11.04	-11.35	-10.93	-13.42
-10.92	-11.13	-11.42	-10.89	-13.58
-11.09	-11.12	-11.13	-11.58	-13.37
-11.17	-11.17	-11.05	-11.78	-13.89
-10.92	-11.27	-10.31	-11.06	-13.37
-10.88	-10.97	-11.11	-11.56	-13.65
-10.90	-10.92	-10.40	-10.91	-13.54
-11.26	-10.90	-10.95	-11.09	-13.44
-10.97	-10.89	-11.17	-10.87	-13.68
-11.38	-11.08	-10.51	-10.05	-13.55
-10.98	-11.04	-10.99	-11.03	-13.58
-10.99	-11.08	-10.97	-10.88	-13.49
-11.36	-11.33	-11.08	-11.70	-13.36
-11.26	-10.89	-11.46	-11.02	-13.54
-11.50	-10.92	-11.36	-10.98	-13.57
-11.04	-10.92	-11.42	-11.30	-13.31
-10.92	-11.09	-11.36	-11.00	-13.62
-11.58	-10.87	-10.56	-10.30	-12.95
-11.55	-10.98	-10.60	-10.27	-12.64
-11.28	-10.85	-10.19	-11.93	-12.31
-10.97	-11.06	-11.18	-11.88	-12.17
-10.74	-11.10	-11.33	-11.54	-13.02
-10.74	-10.91	-11.53	-11.61	-13.73
-11.05	-10.96	-11.08	-11.73	-13.48
-10.92	-11.15	-11.23	-11.37	-13.32
-11.30	-10.85	-10.48	-11.14	-13.82
-11.18	-10.94	-11.19	-10.69	-13.87
-11.28	-11.16	-10.86	-11.10	-13.90
-11.26	-11.14	-11.08	-11.18	-13.87
-11.22	-11.27	-11.34	-11.04	-13.33
-11.57	-10.98	-11.58	-10.96	-12.35
-11.56	-10.54	-11.49	-11.08	-13.25
-11.62	-10.94	-11.51	-10.87	-13.63
-11.53	-10.95	-11.03	-10.77	-13.09
-11.58	-11.14	-11.09	-10.82	-12.12
	-10.79	-10.83	-10.70	-13.00

sandy mixed zone cont.	sandy mixed zone cont.	sandy mixed zone cont.	cemented hw mixed zone cont.
-11.09	-11.11	-10.82	-13.12
-11.10	-10.92	-11.08	-13.44
-11.00	-11.19	-11.38	-13.62
-10.88	-11.11	-11.60	-13.29
-10.95	-11.70	-11.23	-13.66
-10.90	-10.92	-10.80	-13.38
-10.85	-10.71	-10.81	-12.74
-11.18	-11.28	-10.95	-13.33
-10.93	-11.27	-11.10	-12.98
-11.08	-11.22	-10.67	-13.07
-10.80	-11.40	-11.25	-13.33
-11.02	-11.10	-11.21	-13.05
-10.77	-11.40	-10.74	-13.19
-10.80	-11.54	-10.70	-13.80
-10.56	-11.44	-10.58	-12.68
-10.95	-11.37	-11.21	-13.33
-11.04	-11.75	-11.22	-13.28
-10.94	-11.64	-11.43	-13.25
-10.88	-11.29	-10.92	-13.07
-10.84	-11.14	-11.30	-13.63
-10.64	-10.50	-11.15	-13.25
-11.05	-10.54	-10.92	-13.20
-10.90	-9.98	-11.23	-13.26
-11.19	-10.01	-10.99	-13.51
-11.32	-10.67	-10.90	-13.69
-11.17	-11.36	-10.65	-13.53
-11.10	-11.48	-10.94	-13.64
-11.44	-11.45	-11.30	-13.16
-10.81	-11.38	-10.90	-13.32
-10.69	-11.42	-10.93	-13.32
-11.04	-11.58	-10.56	-12.44
-10.87	-11.39	-10.28	-12.25
-10.91	-11.73	-10.68	-12.53
-10.90	-11.55	-10.39	-12.86
-11.04	-11.77	-10.71	-13.17
-10.80	-11.70	-10.54	-12.39
-10.93	-11.42	-11.08	-13.38
-10.95	-11.22	-11.24	-12.86
-10.89	-11.30	-11.09	-13.25
-11.08	-11.55	-10.97	-13.26
-11.18	-11.23	-10.86	-12.91
-11.04	-11.62	-10.69	-13.32
-11.05	-11.38	-10.79	-13.31

sandy mixed zone cont.	sandy mixed zone cont.	sandy mixed zone cont.	cemented hw mixed zone cont.
-11.12	-11.40	-11.50	-13.25
-10.96	-11.27	-11.53	-13.09
-10.90	-11.18	-11.36	-13.40
-10.95	-10.69	-11.56	-12.79
-11.00	-11.21	-11.93	-12.44
-10.93	-10.99	-11.97	-12.94
-11.04	-11.13	-11.53	-13.55
-10.82	-11.15	-11.20	-12.95
-10.88	-11.11	-12.08	-12.95
-10.72	-11.47	-11.21	-13.41
-11.26	-11.43	-11.64	-13.32
-11.16	-11.42	-12.17	-13.03
-10.77	-11.18	-11.46	-12.09
-11.19	-11.18	-11.48	-13.48
-11.26	-10.83	-11.42	-13.31
-11.05	-10.96	-11.10	-12.62
-10.85	-11.24	-11.02	-13.21
-10.79	-11.83	-10.94	-13.09
-10.62	-10.98	-11.12	-13.32
-10.88	-11.07	-11.25	-13.38
-11.13	-12.08	-11.09	-12.96
-11.10	-12.27	-11.02	-12.98
-11.18	-12.10	-11.05	-13.43
-10.58	-11.62	-10.60	
-10.80	-11.89	-11.66	
-10.73	-12.27	-11.74	
-11.30	-12.27	-10.97	
-11.06	-12.12	-12.17	
-10.50	-11.79	-11.51	
-10.91	-12.28	-11.02	
-10.69	-11.85	-10.95	
-10.44	-11.80	-11.71	
-10.36	-11.68	-11.47	
-10.90	-11.61	-11.73	
-10.46	-11.66	-11.12	
-10.95	-11.54	-11.41	
-10.82	-11.69	-11.39	
-10.88	-11.38	-11.35	
-11.14	-10.75	-11.14	
-10.87	-11.98	-11.28	
-10.92	-11.99	-11.84	
-10.97	-10.64	-11.93	
-11.08	-11.01	-11.61	

sandy mixed zone cont.	sandy mixed zone cont.	sandy mixed zone cont.
-10.99	-11.20	-11.65
-10.74	-11.69	-11.64
-10.88	-10.69	-11.34
-11.45	-10.95	-11.83
-11.39	-11.75	-11.28
-9.98	-11.86	-10.73
-10.19	-11.78	-10.56
-11.04	-11.72	-10.92
-10.87	-11.64	-10.96
-10.91	-11.76	-11.19
-10.84	-11.79	-10.94
-11.00	-11.90	-10.71
-10.98	-11.28	-11.53
-11.06	-11.98	-11.59
-10.72	-11.76	-11.68
-10.77	-11.57	-11.40
-11.25	-11.52	-11.24
-11.18	-11.37	-12.19
-11.51	-11.76	-11.51
-11.97	-11.67	-11.56
-12.23	-11.48	-11.28
-12.19	-11.61	-11.48
-10.85	-11.68	-10.88
-11.06	-11.73	-10.85
-11.53	-11.62	-10.84
-11.72	-11.56	-11.32
-11.99	-11.56	-10.98
-11.83	-11.49	-11.51
-12.14	-11.38	-10.91
-12.17	-10.69	-10.98
-12.08	-10.65	-10.96
-11.02	-10.72	-10.80
-11.10	-10.84	-10.84
-11.10	-11.02	-10.90
-11.31	-11.40	-10.85
-11.06	-11.35	-10.64
-11.09	-10.98	-11.29
-10.95	-11.09	-11.36
-10.71	-10.94	-11.33
-10.73	-10.86	-11.86
-12.18	-10.93	-10.85
-12.42	-11.07	-11.04
-12.46	-10.88	-10.64
-11.96	-11.10	-10.87

sandy mixed zone cont.	sandy mixed zone cont.	sandy mixed zone cont.
-12.26	-11.33	-11.02
-12.26	-11.51	-11.05
-12.27	-11.84	-10.70
-11.00	-11.79	-10.93
-10.90	-11.29	-11.46
-10.96	-11.12	-11.46
-11.02	-11.18	-10.42
-10.56	-11.23	-10.54
-10.45	-11.79	-10.30
-10.86	-11.23	-10.95
-10.43	-10.83	-10.14
-10.49	-11.05	-10.14
-10.91	-11.10	-10.87
-10.84	-10.93	-10.28
-11.25	-11.01	-10.31
-11.45	-10.92	-11.16
-11.47	-11.00	-11.16
-11.53	-12.18	-11.09
-10.83	-11.80	-11.13
-11.61	-11.90	-11.04
-10.65		

Consolidometer measurements - data are log(k); k in m^2		
sandy/silty clay	**clay core**	**undeformed clay**
-16.97	-18.70	-17.77
-16.71	-18.14	-18.82
-17.26	-19.07	
	-18.70	
	-18.51	

REFERENCES CITED

An, L. -j., and Sammis, C., 1994, Particle size distribution of cataclastic fault materials from southern California: a 3-d study: Pure and Applied Geophysics, v. 143, p. 203-227.

Anderson, E. M., 1951, The dynamics of faulting and dyke formation, with applications to Britain: Edinburgh, Oliver and Boyd, 206 p.

Anderson, T. W., Welder, G. E., Lesser, G., and Trujillo, A., 1988, Region 7, Central alluvial basins, *in* Back, W., Rosenshein, J. S., and Seaber, P. R., eds., Hydrogeology: Boulder, CO, Geological Society of America, Geology of North America, v. O-2, p. 81-86.

Antonellini, M. A. and Aydin, A., 1994, Effect of faulting on fluid flow in porous sandstones: petrophysical properties: American Association of Petroleum Geologists Bulletin, v. 78, p. 355-377.

Antonellini, M. A. and Aydin, A., 1995, Effect of faulting on fluid flow in porous sandstones: geometry and spatial distribution: American Association of Petroleum Geologists Bulletin, v. 79, p. 642-671.

Antonellini, M. A., Aydin, A., and Pollard, D. A., 1994, Microstructure of deformation bands in porous sandstones at Arches National Park, Utah: Journal of Structural Geology, v. 16, p. 941-959.

Atkinson, J. H., and Bransby, P. L., 1978, The mechanics of soils: an introduction to critical state soil mechanics: New York, McGraw-Hill, 375 p.

Aydin, A., 1978, Small faults formed as deformation bands in sandstones: Pure and Applied Geophysics, v. 116, p. 913-930.

Aydin, A., and Johnson, A. M., 1978, Development of faults as zones of deformation bands and as slip surfaces in sandstone: Pure and Applied Geophysics, v. 116, p. 931-942.

Barton, C. A., Zoback, M. D., and Moos, D., 1995, Fluid flow along potentially active faults in crystalline rock: Geology, v. 23, p. 683-686.

Beckner, J., 1996, Cementation processes and sand petrography of the Zia Formation, Albuquerque Basin, New Mexico [M.S. thesis]: New Mexico Institute of Mining and Technology, 146 p.

Beckner, J., and Mozley, P. S., 1998, Origin and spatial distribution of early phreatic and vadose calcite cements in the Zia formation, Albuquerque Basin, New Mexico, USA, *in* Morad, S., ed., Carbonate Cements in Sandstones: International Association of Sedimentologists Special Publication, v. 26, p. 27-51.

Been, K., Jefferies, M. G., and Hachey, J., 1991, The critical state of sands: Geotechnique v. 41, p. 365-381.

Benn, D. I., and Evans, D. J. A., 1996, The interpretation and classification of subglacially deformed materials: Quaternary Science Reviews, v. 15, p. 23-52.

Berg, R. R., and Avery, A. H., 1995, Sealing properties of Tertiary growth faults, Texas gulf coast: American Association of Petroleum Geologists Bulletin, v. 70, p. 375-393.

Berryman, J. G., 1985, Measurement of spatial correlation functions using image processing techniques: Journal of Applied Physics, v. 57, p. 2374-2384.

Berryman, J. G., and Blair, S. C., 1986, Use of digital image analysis to estimate fluid permeability of porous materials: Application of two-point correlation functions: Journal of Applied Physics, v. 60, p. 1930-1938.

Berryman, J. G., and Blair, S. C., 1987, Kozeny-Carman relations and image processing methods for estimating Darcy's constant: Journal of Applied Physics, v. 62, p. 2221-2228.

Biegel, R. L., Sammis, C. G., and Dieterich, J. H., 1989, The frictional properties of simulated gouge having a fractal particle distribution: Journal of Structural Geology, v. 11, p. 827-846.

Bishop, A. W., 1975, The strength of soils as engineering materials, *in* Milestones in soil mechanics; the first ten Rankine lectures: UK, Thomas Telford Ltd., p. 91-128.

Blair, S. C., Berge, P. A., and Berryman, J. G., 1996, Using two-point correlation functions to characterize microgeometry and estimate permeabilities of sandstones and porous glass: Journal of Geophysical Research, v. 101, p. 20359-20375.

Blenkinsop, T. G., 1991, Cataclasis and processes of particle size reduction: Pure and Applied Geophysics. v. 136, p. 59-86.

Blenkinsop, T. G., and Rutter, E. H., 1986, Cataclastic deformation of quartzite in the Moine Thrust Zone: Journal of Structural Geology. v. 8, p. 669-682.

Borg, I., Friedman, M., Handin, J., and Higgs, D. V., 1960, Experimental deformation of St. Peter sand: a study of cataclastic flow, *in* Griggs, D., and Handin, J., eds., Rock Deformation: Geological Society of America Memoir 79, Boulder, CO, The Geological Society of America, p. 133-191.

Borradaile, G. J., 1981, Particulate flow of rock and the formation of cleavage: Tectonophysics, v. 72, p. 305-321.

Bredehoeft, J. D., Belitz, K., and Sharp-Hansen, S., 1992, The hydrodynamics of the Bighorn Basin: A study of the role of faults: American Association of Petroleum Geologists Bulletin, v. 76, p. 530-546.

Brown, K. M., Bekins, B., Clennell, B., Dewhurst, D., and Westbrook, G., 1994, Heterogeneous hydrofracture development and accretionary fault dynamics: Geology, v. 22, p. 259-262.

Byrne, T., 1994, Sediment deformation, dewatering and diagenesis: illustrations from selected melange zones, *in* Maltman, A., ed., The geological deformation of sediments, London, Chapman and Hall, p. 239-260.

Caine, J. S., Evans, J. P. and Forster, C. B., 1996, Fault zone architecture and permeability structure: Geology, v. 24, p. 1025-1028.

Caine, J. S. and Forster, C. B., 1999, Fault zone architecture and fluid flow: insights from field data and numerical modeling, *in* Haneberg, W. C., Mozley, P. S., Moore, K. C., and Goodwin, L. B., eds., Faults and subsurface fluid flow in the shallow crust: Washington, DC, American Geophysical Union, p. 101-127.

Cashman, S., and Cashman, K., 2000, Cataclasis and deformation-band formation in unconsolidated marine-terrace sand, Humboldt County, California: Geology, v. 28, p. 111-114.

Chester, F. M. and Chester, J. S., 1998, Ultracataclasite structure and friction processes of the Punchbowl fault, San Andreas system, California: Tectonophysics, v. 295, p. 199-221.

Chester, F. M., Evans, J. P. and Biegel, R. L., 1993, Internal structure and weakening mechanisms of the San Andreas fault: Journal of Geophysical Research, v. 98, p. 771-786.

Chester, F. M., and Logan, J. M., 1986, Implications for mechanical properties of brittle faults from observations of the Punchbowl fault zone, California: Pure and Applied Geophysics, v. 124, p. 79-106.

Childs, C., Watterson, J., and Walsh, J. J., 1996, A model for the structure and development of fault zones: Journal of the Geological Society, v. 153, p. 337-340.

Cladouhos, T. T., 1999, Shape preferred orientations of survivor grains in fault gouge: Journal of Structural Geology, v. 21, p. 419-436.

Connell, S. D., Koning, D. J., and Cather, S. M., 1999, Revisions to the stratigraphic nomenclature of the Santa Fe Group, northwestern Albuquerque Basin, New Mexico,

in Pazzaglia, F. J., and Lucas, S. G., eds., Albuquerque Geology: New Mexico Geological Society, 50th Annual Field conference, Guidebook, p. 337-353.

Crabtree, S. J., Ehrlich, R., and Prince, C., 1984, Evaluation of strategies for segmentation of blue-dyed pores in thin sections of reservoir rocks: Computer Vision, Graphics, and Image Processing, v. 28, p. 1-18.

Das, B.M., 1983, Advanced soil mechanics: Washington, DC, Hemisphere Publishing Corporation, 511 p.

Deutsch, C. V., and Journel, A. G., 1998, GSLIB: geostatistical software library and user's guide: New York, Oxford University Press, 369 p.

Domenico, P. A., and Schwartz, F. W., 1990, Physical and chemical hydrogeology: New York, John Wiley, 824 p.

Dunn, D. E., LaFountain, L. J., and Jackson, R. E., 1973, Porosity dependence and mechanism of brittle fracture in sandstones: Journal of Geophysical Research, v. 78, p. 2403-2417.

Ellen, S. D., and Fleming, R. W., 1987, Mobilization of debris flows from soil slips, San Francisco Bay region, California, *in* Costa, J. E., and Wieczorek, G. F., eds., Debris flows/avalanches: process, recognition, and mitigation: Geological Society of America, Reviews in engineering geology, v. 7, p. 31-40.

Engelder, J. T., 1974, Cataclasis and the generation of fault gouge: Geological Society of America Bulletin, v. 85, p. 1515-1522.

Evans, J. P., Forster, C. B., and Goddard, J. V., 1997, Permeability of fault related rocks, and implications for hydraulic structure of fault zones: Journal of Structural Geology, v. 19, p. 1393-1404.

Folk, R. L., 1974, Petrology of sedimentary rocks, Austin, TX, Hemphill, 182 p.

Forster, C., and Evans, J., 1991, Hydrogeology of thrust faults and crystalline thrust sheets: results of combined field and modeling studies: Geophysical Research Letters, v. 18, p. 979-982.

Foxford, K. A., Walsh, J. J., Watterson, J., Garden, I. R., Guscott, S. C. and Burley, S. D., 1998, Structure and content of the Moab Fault Zone, Utah, USA, and its implications for fault seal prediction, *in* Jones, G., Fisher, Q. J. and Knipe, R. J., eds., Faulting, fault sealing, and fluid flow in hydrocarbon reservoirs: London, The Geological Society, p. 87-103.

Gibson, R. G., 1998, Physical character and fluid-flow properties of sandstone-derived fault zones, *in* Coward, M. P., Daltaban, T. S., and Johnson, H., eds., Structural geology in reservoir characterization: London, The Geological Society, p. 83-97.

Goodwin, L. B., Mozley, P. S., Moore, J. C. and Haneberg, W. C., 1999, Introduction, *in* Haneberg, W. C., Mozley, P. S., Moore, K. C., and Goodwin, L. B., eds., Faults and subsurface fluid flow in the shallow crust: Washington, DC, American Geophysical Union, p. 1-5.

Gretener, P. E., 1976, Pore pressure: fundamentals, general ramifications and implications for structural geology: American Association of Petroleum Geologists continuing education course notes series 4, 87 p.

Haneberg, W. C., 1995, Steady-state groundwater flow across idealized faults: Water Resources Research, v. 31, p. 1815-1820.

Haneberg, W. C., Gomez, P., Gibson, A., and Allred, B., 1998, Preliminary measurements of stress-dependent hydraulic conductivity of Santa Fe Group aquifer system sediments from the 98th St. core hole, Albuquerque, New Mexico: New Mexico Geology, v. 20, p. 14-20.

Hawley, J. W., 1996, Hydrogeologic framework of potential recharge areas in the Albuquerque basin, central New Mexico: New Mexico Bureau of Mines and Mineral Resources Open-File Report 402 D, Chapter 1, 68 p.

Hawley, J. W., Haase, C. S., Lozinsky, R. P., 1995, An underground view of the Albuquerque Basin, in, The Water Future of Albuquerque and the Middle Rio Grande Basin, Proceedings of the 39th Annual New Mexico Water Conference, New Mexico Water Resources Research Institute Report 290, p. 37-55.

Herrin, M., 2001, Characteristics of deformation bands in poorly lithified sand, Rio Grande rift, New Mexico [M.S. thesis]: New Mexico Institute of Mining and Technology, 81 p.

Heynekamp, M. R., Goodwin, L. B., Mozley, P. S., and Haneberg, W. C., 1999, Controls on fault-zone architecture in poorly lithified sediments, Rio Grande rift, New Mexico: Implications for fault-zone permeability and fluid flow, *in* Haneberg, W. C., Mozley, P. S., Moore, K. C., and Goodwin, L. B., eds., Faults and subsurface fluid flow in the shallow crust: Washington, DC, American Geophysical Union, p. 27-49.

Hippler, S. J., 1993, Deformation microstructures and diagenesis in sandstone adjacent to an extensional fault: implications for the flow and entrapment of hydrocarbons: American Association of Petroleum Geologists Bulletin, v. 77, p. 625-637.

Hooke, R. L., and Iverson, N. R., 1995, Grain-size distribution in deforming sub-glacial tills: role of grain fracture: Geology, v. 23, p. 57-60.

Hooper, E. C. D., 1991, Fluid migration along growth faults in compacting sediments: Journal of Petroleum Geology, v. 14, p. 161-180.

Jiang, D. and Williams, P. F., 1998, High-strain zones: a unified model: Journal of Structural Geology, v. 20, p. 1105-1120.

Jones, M. E., and Addis, M. A., 1984, Volume change during sediment diagenesis and the development of growth faults: Marine and Petroleum Geology, v. 1, p. 118-122.

Jones, M. E., and Addis, M. A., 1986, The application of stress path and critical state analysis to sediment deformation: Journal of Structural Geology, v. 8, p. 575-580.

Jones, M. E., and Preston, R. M. F., eds., Deformation of Sediments and Sedimentary Rocks: Geological Society of London Special Publication 29, 350 p.

Karig, D. E., 1986, Physical properties and mechanical state of accreted sediments in the Nankai Trough, S.W. Japan, *in* Moore, J. C., ed., Structural fabrics in Deep Sea Drilling Project cores form forearcs: Memoir 166, Boulder, CO, The Geological Society of America, p. 117-133.

Karig, D. E., and Hou, G., 1992, High -stress consolidation experiments and their geologic implications: Journal of Geophysical Research, v. 97, p. 289-300.

Kennedy, S. K., and Mazzulo, J., 1991, Image analysis method of grain size measurement, *in* Syvitski, J. P. M., ed., Principles, methods, and application of particle size analysis: Cambridge University Press, p. 76-87.

Kernodle, J. M., 1998, Simulation of ground-water flow in the Albuquerque Basin, central New Mexico, 1901-1995, with projections to 2020: U.S. Geological Survey Open File Report 96-209, 54 p.

Kharaka, Y. K., Thordsen, J. J., Evans, W. C., and Kennedy, B. M., 1999, Geochemistry and hydromechanical interactions of fluids associated with the San Andreas fault system, California, *in* Haneberg, W. C., Mozley, P. S., Moore, J. C., and Goodwin, L. B., eds., Faults and subsurface fluid flow in the shallow crust: Washington, DC, American Geophysical Union, p. 129-148.

Knipe, R. J., 1993, The influence of fault zone processes and diagenesis on fluid flow, *in* Horbury, A. D., and Robinson, A. G., eds., Diagenesis and basin development: Tulsa, OK, American Association of Petroleum Geologists, p. 135-151.

Kolm, K. E., and Downey, J. S., 1994, Diverse flow patterns in the aquifers of the Amargosa Desert and vicinity, southern Nevada and California: Association of Engineering Geologists Bulletin, v. 31, p. 33-47.

Krinsley, D. H., and Doornkamp, J. C., 1973, Atlas of quartz sand surface textures: Cambridge University Press, 91 p.

Krinsley, D. H., and Marshall, J. R., 1987, Sand grain textural analysis: an assessment, *in* Marshall, J. R., ed., Clastic particles: New York, Van Nostrand Reinhold Company, p. 2-15.

Lin, S., Jiang, D., and William, P. F., 1998, Transpression (or transtension) zones of triclinic symmetry: natural example and theoretical modelling, *in* Holdsworth, R. E., Strachan, R. A., and Dewey, J. F., eds., Continental transpressional and transtensional tectonics: London, Geological Society, p. 41-57.

Lister, G. S., and Snoke, A. W., 1984, S-C mylonites: Journal of Structural Geology, v. 6, p. 617-638.

Logan, J. M., Dengo, C. A., Higgs, N. G., and Wang, Z. Z., 1992, Fabrics of experimental fault zones: their development and relationship to mechanical behavior, *in* Evans, B., and Wong, T.-f., eds., Fault mechanics and transport properties of rocks: London, Academic Press, p. 33-68.

Lucas, S. E., and Moore, J. C., 1986, Cataclastic deformation in accretionary wedges: Deep Sea Drilling Project Leg 166, southern Mexico, and on-land examples from Barbados and Kodiak Islands, *in* Moore, J. C., ed., Structural fabrics in Deep Sea Drilling Project cores from forearcs, Memoir 166: Boulder, CO, The Geological Society of America, p. 89-104.

Mandl, G., de Jong, L. N. J., and Maltha, A., 1977, Shear zones in granular material: an experimental study of their structure and genesis: Rock Mechanics, v. 9, p. 95-144.

Marone, C., and Scholz, C. H., 1989, Particle-size distribution and microstructures within simulated fault gouge: Journal of Structural Geology, v. 11, p. 799-814.

Matthai, S. K., and Roberts, S. G., 1996, The influence of fault permeability on single-phase fluid flow near fault sand intersections: results from steady-state high-

resolution models of pressure-driven fluid flow: American Association of Petroleum Geologists Bulletin, v. 80, p. 1763-1779.

Mazzulo, J., and Kennedy, S. K., 1985, Automated measurement of the nominal sectional diameters of individual sedimentary particles: Journal of Sedimentary Petrology, v. 55, p. 593-595.

McCave, I. N., and Syvitski., J. P. M., 1991, Principles and methods of geological particle size analysis, *in* Syvitski, J. P. M., ed., Principles, methods, and application of particle size analysis: Cambridge, Cambridge University Press, p. 3-22.

McCord, J. T., and Stephens, D. B., 1999, Contrasts in regional and local-scale heterogeneity in relation to ground-water supply and contamination in the Albuquerque basin, *in* Pazzaglia, F. J., and Lucas, S. G., eds., Albuquerque Geology: New Mexico Geological Society, 50th Annual Field conference, Guidebook, p. 401-408.

Menéndez, B., Zhu, W., and Wong, T.-f., 1996, Micromechanics of brittle faulting and cataclastic flow in Berea sandstone: Journal of Structural Geology, v. 18, p. 1-16.

Mifflin, M. D., 1988, Region 5, Great Basin, *in* Back, W., Rosenshein, J. S., and Seaber, P. R., eds., Hydrogeology: Boulder, CO, Geological Society of America, Geology of North America, v. O-2, p. 69-78.

Miller, M. G., 1996, Ductility in fault gouge from a normal fault system, Death Valley, California: a mechanism for fault zone strengthening and relevance to paleoseismicity: Geology, v. 24, p. 603-606.

Moore, J. C., ed., Structural fabrics in Deep Sea Drilling Project cores from forearcs, Memoir 166: Boulder, CO, The Geological Society of America, 160 p.

Moore, J. C., and Byrne, T., 1987, Thickening of fault zones: a mechanism of melange formation in accreting sediments: Geology, v. 15, p. 1040-1043.

Morrow, C. A., Shi, L. Q., and Byerlee, J. D., 1981, Permeability and strength of San Andreas fault gouge under high pressure: Geophysical Research Letters, v. 8, p. 325-328.

Morrow, C. A., Shi, L. Q., and Byerlee, J. D., 1984, Permeability of fault gouge under confining pressure and shear stress: Journal of Geophysical Research, v. 89, p. 3193-3200.

Mozley, P. S., and Goodwin, L. B., 1995, Patterns of cementation along a Cenozoic normal fault: A record of paleoflow orientations: Geology, v. 23, p. 539-542.

Pazzaglia, F. J., Connell, S. D., Hawley, J., Tedford, R. H., Personius, S., Smith, G. A., Cather, S., Lucas, S., Hester, P., Gilmore, J., and Woodward, L., 1999a, Second-day trip 2 road log, from Albuquerque to San Ysidro, Loma Creston, La Ceja, and Sand Hill fault, *in* Pazzaglia, F. J., and Lucas, S. G., eds., Albuquerque Geology: New Mexico Geological Society, 50th Annual Field conference, Guidebook, p. 47-66.

Pazzaglia, F. J., Woodward, L. A., Lucas, S. G., Anderson, O. J., Wegman, K. G., and Estep, J. W., 1999b, Phanerozoic geologic evolution of the Albuquerque area, *in* Pazzaglia, F. J., and Lucas, S. G., eds., Albuquerque Geology: New Mexico Geological Society, 50th Annual Field conference, Guidebook, p. 97-114.

Porter, J. R., Knipe, R. J., Fisher, Q. J., Farmer, A. B., Allin, N. S., Jones, L. S., Palfrey, A. J., Garrett, S. W., and Lewis, G., 2000, Deformation processes in the Britannia Field, UKCS: Petroleum Geoscience, v. 6, p. 241-254.

Renard, P., and de Marsily, G., 1997, Calculating equivalent permeability: A review: Advances in Water Resources, v. 20, p. 253-278.

Russ, J.C. 1991, Practical Stereology: New York, Plenum Press, 185 p.

Russ, J.C. 1999, The image processing handbook: Boca Raton, FL, CRC Press, 771 p.

Rutter, E. H., 1986, On the nomenclature of mode of failure transitions in rocks: Tectonophysics, v. 122, p. 381-387.

Rutter, E. H., Maddock, R. H., Hall, S. H., and White, S. H., 1986, Comparative microstructures of natural and experimentally produced clay bearing fault gouges: Pure and Applied Geophysics, v. 124, p. 3-29.

Sammis, C., King, G., and Biegel, R., 1987, The kinematics of gouge deformation: Pure and Applied Geophysics, v. 125, p. 777-812.

Scott, C. R., 1980, An introduction to soil mechanics and foundations: London, Applied Science Publishers, 406 p.

Shafike, N. G., and Flanigan, K. G., 1999, Hydrologic modeling of the Estancia Basin, New Mexico, *in* Pazzaglia, F. J., and Lucas, S. G., eds., Albuquerque Geology: New Mexico Geological Society, 50th Annual Field conference, Guidebook, p. 409-418.

Shelley, D., 1995, Asymmetric shape preferred orientations as shear-sense indicators: Journal of Structural Geology, v. 17, p. 509-517.

Sibson, R. H. 1977, Fault rocks and fault mechanisms: Journal of the Geological Society of London, v. 133, p. 191-213.

Sigda, J. M., Goodwin, L. B., Mozley, P. S., and Wilson, J. L., 1999, Permeability alteration in small-displacement faults in poorly lithified sediments: Rio Grande Rift, Central New Mexico, *in* Haneberg, W. C., Mozley, P. S., Moore, K. C., and Goodwin, L. B., eds., Faults and subsurface fluid flow in the shallow crust: Washington, DC, American Geophysical Union, p. 51-68.

Skempton, A. W., 1985, Residual strength of clays in landslides, folded strata, and in the laboratory: Geotechnique, v. 35, p. 3-18

Smith, D. A., 1980, Sealing and non-sealing faults in the Louisiana Gulf Coast salt basin: American Association of Petroleum Geologists Bulletin, v. 64, p. 145-172.

Smith, L., Forster, C., and Evans, J., 1990, Interaction of fault zones, fluid flow, and heat transfer at the basin scale, *in* Neuman, S. P., and Neretnieks, I., eds., Hydrogeology of low permeability environments, Hanover, Verlag Heinz Heisse, p. 41-67.

Starkey, J., 1977, The contouring of orientation data represented in spherical projection: Canadian Journal of Earth Sciences, v. 14, p. 268-277.

Tedford, R. H., and Barghoorn, S., 1999, Santa Fe Group (Neogene), Ceja del Rio Puerco, Northwestern Albuquerque Basin, Sandoval County, New Mexico, *in* Pazzaglia, F. J., and Lucas, S. G., eds., Albuquerque Geology: New Mexico Geological Society, 50th Annual Field conference, Guidebook, p. 327-335.

Thorn, C. R., McAda, D. P., and Kernodle, J. M., 1993, Geohydrologic framework and hydrologic conditions in the Albuquerque Basin, central New Mexico: U. S. Geological Survey Water Resources Investigations Report 93-4149, 106 p.

Turcotte, D. L., and Huang, J., 1995, Fractal distributions in geology, scale invariance, and deterministic chaos, *in* Barton, C. C., and La Pointe, P. R., eds., Fractals in the Earth Sciences: New York, Plenum Press, p. 1-40.

Underhill, J. R., and Woodcock, N. H., 1987, Faulting mechanisms in high-porosity sandstones; New Red Sandstone, Arran, Scotland, *in* Jones, M. E., and Preston, R. M. F., eds., Deformation of Sediments and Sedimentary Rocks: Geological Society of London Special Publication 29, p. 91-105.

Watterson, J., Childs, C., and Walsh, J. J., 1998, Widening of fault zones by erosion of asperities formed by bed-parallel slip: Geology, v. 26, p. 71-74.

Weber, K. J., Mandl, G., Pilaar, W. F., Lehner, F., and Precious, R. G., 1978, The role of faults in hydrocarbon migration and trapping in Nigerian growth fault structures, *in* Proceedings, Offshore Technology Conference, 10th, Houston: Dallas, Offshore Technology Conference, p. 2643-2653.

Whitworth, T. M., Haneberg, W. C., Mozley, P. S., and Goodwin, L. B., 1999, Solute-sieving induced calcite precipitation on pulverized quartz sand: experimental results and implications for membrane behavior of fault gouge, *in* Haneberg, W. C., Mozley, P. S., Moore, K. C., and Goodwin, L. B., eds., Faults and subsurface fluid flow in the shallow crust: Washington, DC, American Geophysical Union, p. 149-158.

Wilson, E. B., 1952, An introduction to scientific research: New York, McGraw-Hill,

375 p.

Wong, T. -f., David, C., and Zhu, W., 1997, The transition from brittle faulting to cataclastic flow in porous sandstones: Mechanical deformation: Journal of Geophysical Research, v. 102, p. 3009-3025.

Yielding, G., Freeman, B., and Needham, D. T., 1997, Quantitative fault seal prediction: American Association of Petroleum Geologists Bulletin, v. 81, p. 897-917.

Zhang, J., Wong, T. -f., and Davis, D. M., 1990, Micromechanics of pressure-induced grain crushing in porous rocks: Journal of Geophysical Research, v. 95, p. 341-352.